UNIWERSYTET KAZIMIERZA WIELKIEGO W BYDGOSZCZY
RADA DZIEDZINY NAUK ŚCISŁYCH I PRZYRODNICZYCH

Anton Markovskyi

Optical and mechanical properties of phosphor converters for white LEDs based on the single crystalline films and single crystals of garnets

Właściwości optyczne i mechaniczne konwertorów diod białych na bazie warstw monokrystalicznych i kryształów granatów

Dysertacja na stopień doktora

Promotor:
prof. dr. hab. Yuriy Zorenko

Drugi promotor:

dr. hab. Michał Pakuła, prof. uczelni

Bydgoszcz 2023

Abstract

This Ph.D. thesis focuses on investigating the structural, luminescence, photoconversion, and elastic properties of garnet-based epitaxial structures for application as phosphor converters (**pc**) in white light-emitting diodes (WLEDs). The aim of the research is to better understand the behavior of garnet-based materials as efficient and reliable **pc** in WLEDs and contribute to their optimization for lighting applications. The liquid phase epitaxy (LPE) method was used for the growth of film and composite color converters based on the epitaxial structures of garnet compounds. The single crystalline films (SCF) of Ce^{3+} doped $Lu_3Al_5O_{12}$ (LuAG:Ce), $Tb_3Al_5O_{12}$ (TbAG:Ce), and $Tb_{1.5}Gd_{1.5}Al_5O_{12}$ (TbGdAG:Ce) garnets were grown onto undoped $Y_3Al_5O_{12}$ (YAG) and Ce^{3+} doped $Y_3Al_5O_{12}$ (YAG:Ce) substrates using LPE technique. The thesis also includes a comprehensive structural investigation of the films and composite converters using optical microscopy, scanning transmission electron microscopy (STEM), and X-ray diffraction (XRD) analyses. These characterization techniques provide valuable insights into the crystal structure, morphology, and interface properties of the garnet-based epitaxial structures.

Within the theoretical and numerical research, a microscopic layered model is developed to describe the propagation of ultrasonic waves in the epitaxial structures. This modeling approach aims to identify the elastic properties of the garnet-based films and substrates. Experimental investigations using ultrasonic microscopy are conducted on LuAG:Ce SCF/YAG:Ce substrate epitaxial structures for the frequencies ranged from 35 to 200 MHz. To identify the mechanical (i.e., elastic) properties of the investigated films and substrates, the results acquired withn ultrasonic studies are further analyzed using an optimization-based algorithm, which utilizes the microscopic model of wave propagation and numerical analysis.

The optical properties of the film and composite converters under study are examined through measurements of absorption, cathodo- and photoluminescence spectra. This analysis helps assess their spectral characteristics. The investigation of photoconversion properties is an essential aspect of the research. Measurements of color coordinates (CC), color temperature (CCT), color rendering index (CRI), and luminous efficacy (LE) are performed both for the film and composite converters. These properties play a crucial role in determining the color quality, temperature, and efficiency of the emitted light, thereby contributing to the optimization of garnet-based phosphor converters for WLED applications.

Finally, the prototype of WLED photoconverters were created based on the SCFs of Ce^{3+} doped $Lu_3Al_5O_{12}$, $Tb_3Al_5O_{12}$, and $Tb_{1.5}Gd_{1.5}Al_5O_{12}$ garnets with different thickness, grown onto YAG substrates. Furthermore, the composite color converters based on the TbAG:Ce and $Tb_{1.5}Gd_{1.5}$AG:Ce SCF films with different thicknesses and Ce^{3+} doped YAG substrates with various Ce concentrations and thicknesses, were developed. The photoconversion properties of developed film and composite converters were studied and the best compositions were selected.

Streszczenie

Niniejsza rozprawa doktorska obejmuje badanie strukturalnych, mechanicznych, luminescencyjnych oraz fotokonwersyjnych właściwości struktur epitaksjalnych granatów, które znajdują zastosowanie jako monokrystaliczne fosfory-konwertory w elektroluminescencyjnych diodach emitujących światło białe (WLED). Głównym celem badawczym pracy było pogłębienie wiedzy na temat właściwości luminescencyjnych materiałów w postaci warstw monokrystalicznych i wybranych kryształów granatu, które stanowią podstawę efektywnych konwerterów fosfor-WLED. Ponadto w ramach pracy zoptymalizowano właściwości fotokonwersyjne tych materiałów, aby uzyskać wydajne źródła światła białego.

Do produkcji fosforów-konwertorów WLED zarówno w postaci warstw monokrystalicznych, jak i kompozytowych konwertorów typu "warstwa-kryształ", wykorzystano metodę epitaksji w fazie ciekłej (metodę LPE). M. in., przy użyciu metody LPE uzyskano domieszkowane jonami Ce^{3+} warstwy monokrystaliczne wybranych granatów, takich jak $Lu_3Al_5O_{12}$ (LuAG:Ce), $Tb_3Al_5O_{12}$ (TbAG:Ce) oraz $Tb_{1.5}Gd_{1.5}Al_5O_{12}$ (TbGdAG:Ce). Hodowli warstw tych granatów dokonano z roztworów w stopie na bazie topnika $PbO\text{-}B_2O_3$ na podłożach granatów $Y_3Al_5O_{12}$ (YAG) oraz YAG:Ce o różnym stężeniu ceru.

Przeprowadzono także kompleksowe badania strukturalne tych warstw monokrystalicznych oraz kompozytowych struktur epitaksjalnych granatów za pomocą skaningowej mikroskopii transmisyjnej (STEM) oraz analizy dyfrakcji rentgenowskiej (XRD). Badania te pozwoliły uzyskać istotne informacje na temat struktury krystalicznej, morfologii i właściwości interfejsu "warstwa-kryształ" w strukturach epitaksjalnych opartych na granatach.

W ramach badań teoretycznych i numerycznych opracowano model opisujący propagację fal ultradźwiękowych w warstwowych strukturach epitaksjalnych. Model ten pozwolił na identyfikację właściwości sprężystych warstw i podłoży opartych na granatach. Przeprowadzono również badania eksperymentalne struktur epitaksjalnych typu "warstwa LuAG:Ce/kryształ YAG:Ce" z wykorzystaniem mikroskopii ultradźwiękowej w szerokim zakresie częstotliwości (35-200 MHz). W celu identyfikacji właściwości mechanicznych (sprężystych) badanych warstw i podłoży, wyniki badań mikroskopii ultradźwiękowej zostały poddane analizie za pomocą algorytmu optymalizacjnego, z wykorzystaniem opracowanego mikroskopowego modelu propagacji fali oraz analizę numeryczną W pracy dokonano badań właściwości optycznych granatów poprzez pomiar ich widm absorpcji, katodoluminescencji oraz fotoluminescencji. Analiza ta pozwoliła na ocenę spektralnych charakterystyk luminescencyjnych tych materiałów, które są istotne dla ich zastosowania w WLED. Badania fotokonwersyjnych właściwości warstw, kryształów oraz struktur epitaksjalnych granatów

stanowiły także ważny aspekt pracy. Przeprowadzono pomiary współrzędnych barwowych (CC), temperatury barwowej (CCT), wskaźnika oddawania barw (CRI) oraz wydajności świetlnej (LE) zarówno dla warstw, jak i kompozytowych konwerterów. Te właściwości odgrywają kluczową rolę w określaniu jakości barwowej, temperatury i wydajności emitowanego światła, co przyczyniło się do optymalizacji składy konwerterów opartych na strukturach epitaksjalnych granatów do zastosowań w źródłach oświetleniowych.

W końcowej części pracy stworzono prototypy fotokonwerterów WLED opartych na domieszkowanych jonami Ce^{3+} warstwach monokrystalicznych granatów LuAG:Ce, TbAG:Ce oraz $Tb_{1.5}Gd_{1.5}AG$:Ce o różnej grubości, krystalizowanych metodą LPE na podłożach YAG. Opracowano także kompozytowe konwertery WLED oparte na warstwach monokrystalicznych granatów TbAG:Ce oraz $Tb_{1.5}Gd_{1.5}AG$:Ce, hodowanych przy użyciu metody LPE na podłożach YAG:Ce o różnym stężeniu ceru i grubości. Dodatkowo przeprowadzono badania fotokonwersyjnych właściwości opracowanych warstwowych i kompozytowych konwertorów oraz wybrano najlepsze składy tych konwertorów.

Contents

Abbreviations

ADC – Analog-to-digital converter
CCC - Composite color converter
CF- Cost function
CCT - Correlated color temperature
CL- cathodoluminescence
CRI - Color rendering index
GGG - Gadolinium Gallium Garnet
IC - Interfacial conditions
LDs- Laser diodes
LE - Luminous efficiency
LED - Light-emitting diode
LPE - Liquid phase epitaxy
LuAG- Lutetium Aluminum Garnet
MOCVD - Metal-organic chemical vapor deposition
MS - Melt-solution
n-UV - Near-ultraviolet
PC - Phosphor converter
PCLC- Planar-Chip-Level Conversion
PC-WLED - Phosphor-converted white LED
PiS- Phosphors in the glass
PL- photoluminescence
PLD - Pulsed laser deposition
QE- Quantum efficiency
RC - Rocking curve
RE - Rare-earth elements
RGB - Red, green, and blue
RMS- Root mean square
SAW- Surface acoustic waves
SAM- Scanning acoustic microscope
SC - Single crystal
SCF - Single crystalline films
SCPs- single crystals phosphors
STEM- Scanning Transmission Electron Microscopy
TbAG - Terbium Aluminum Garnet
T_g – Growth temperature
T_s - Saturation temperature
VCC - Volume-Casting-Conversion
XRD - X-ray diffraction
YAG - Yttrium Aluminium Garnet

"The reward of the young scientist is the emotional thrill of being the first person in the history of the world to see something or to understand something. Nothing can compare with that experience. The reward of the old scientist is the sense of having seen a vague sketch grow into a masterly landscape."

C.H. Payne-Gaposchkin, Astronomical Journal, 1977, 82, 665

Dear Supervisor, prof. dr hab. Yuriy Zorenko, and dear Co-supervisor, dr hab. Michal Paskuła, prof. UKW, I would like to express my heartfelt gratitude for all the help and support that I received during the writing of my doctoral thesis. Without your valuable guidance, suggestions, and professional knowledge, it would not have been possible.

I also want to express my gratitude to all my colleagues from the Chair for Optoelectronic Materials at the Faculty of Physics of UKW who helped me with conducting the measurements and carrying out the research.

I express my gratitude to dr Vitalii Gorbenko for producing all the samples for the research in this work, as well as for teaching me all the intricacies of liquid-phase epitaxial film growth. I am very grateful to MSc. Tetiana Zorenko and dr Sandra Witkiewicz-Łukaszek for assistance in measuring absorption and cathodoluminescence spectra as well as photoluminescence excitation and emission spectra presented in this work.

Next thanks go to the group of researchers led by Prof. Erdmann Spiecker (Institute of Micro- and Nanostructure Research & Center for Nanoanalysis and Electron Microscopy, Friedrich Alexander University of Erlangen-Nuremberg) and prof. Miroslaw Batentschuk (Institute of Materials for Electronics and Energy Technology, University of Erlangen-Nuremberg) for high-resolution scanning transition electron microscopy and composition analysis measurements of the specially-prepared cross-section of the epitaxial structures of LuAG/YAG and TbAG/YAG garnet compounds.

I am very grateful to dr Alexander Fedorov for X-ray diffraction measurements and data analysis at the Institute for Single Crystals, National Academy of Sciences of Ukraine.

Next thanks go to prof. dr hab. Jerzy Litniewski and his group from the Institute of Fundamental Technological Research Polish Academy of Sciences in Warsaw for measuring the studied samples using acoustic microscopy.

I also want to thank my colleagues dr Karol Bartosiewicz and MSc. Yuriy Syrotych for their motivation and support throughout my doctoral studies. I would also like to thank my family and friends for their support and patience during this challenging process. I am honored to have had such wonderful people around me who helped me achieve this important goal in my life.

Szanowny Panie Promotorze, prof. dr. hab. Yuriy Zorenko oraz szanowny Panie Drugi Promotorze, dr. hab. Michale Pakuło, prof. UKW,

Chciałbym wyrazić moje najserdeczniejsze podziękowania za wszelką pomoc i wsparcie, które otrzymałem od Państwa w czasie powstawania mojej pracy doktorskiej. Bez Państwa cennych wskazówek, sugestii oraz fachowej wiedzy nie byłoby to możliwe.

Pragnę również wyrazić swoją wdzięczność dla wszystkich kolegów z Katedry Materiałów Optoelektronicznych Wydziału Fizyki UKW, którzy pomogli mi w przeprowadzaniu badań.

Wyrażam swoją wdzięczność dla dr Vitalija Gorbenko za produkcję próbek struktur epitaksjalnych granatów wykorzystanych w badaniach w tej pracy, a także za nauczanie mnie tajników hodowli warstw metodą epitaksji z fazy ciekłej.

Jestem bardzo wdzięczny mgr Tetianie Zorenko i dr Sandrze Witkiewicz-Łukaszek za pomoc w pomiarach widm absorpcji i katodoluminescencji oraz widm emisji i wzbudzenia fotoluminescencji, przedstawionych w tej pracy.

Następnie dziękuję dwóm grupom badaczy na Uniwersytecie Friedricha-Alexandra w Erlangen-Norymberdze pod kierunkiem prof. Erdmanna Spieckera z Instytutu Badań Mikro- i Nanostruktur oraz Centrum Nanoanalizy i Mikroskopii Elektronowej oraz pod kierunkiem prof. Mirosława Batentschuka z Instytutu Materiałów dla Elektroniki i Technologii Energii za pomiary wysokorozdzielczej transmisyjnej mikroskopii elektronowej i analizę składu specjalnie przygotowanego przekroju struktur epitaksjalnych granatów LuAG/YAG i TbAG/YAG.

Jestem bardzo wdzięczny dr Aleksandrowi Fiodorowowi za pomiar dyfrakcji rentgenowskiej i analizę danych w Instytucie Monokryształów Akademii Nauk Ukrainy. Następnie dziękuję prof. dr hab. Jerzemu Litniewskiemu i jego grupie z Instytutu Podstawowych Problemów Techniki Polskiej Akademii Nauk za pomiar badanych próbek za pomocą mikroskopii akustycznej.

Chciałbym także podziękować moim kolegom dr. Karolowi Bartosiewiczowi i mgr Jurijowi Syrotyczowi za motywację i wsparcie podczas moich studiów doktoranckich. Chciałbym również podziękować mojej rodzinie i przyjaciołom za ich wsparcie i cierpliwość w trudnym procesie. Czuję się zaszczycony, że miałem wokół siebie tak wspaniałych ludzi, którzy pomogli mi osiągnąć ten ważny cel w moim życiu.

Preface

This doctoral thesis was conducted in the frame of the individual research plan at an interdisciplinary doctoral school at the Department of Mechanical Engineering and the Faculty of Physics of Kazimierz Wielki University in Bydgoszcz.

The research related to this doctoral dissertation was also performed in the frame of the National Science Center (NCN) project No 2017/25/B/ST8/02932 “Novel phosphor converters for high power white light emitting diodes based on the ceramics, single crystalline films and hybrid epitaxial structures of mixed garnet compounds” as well as NCN project No 2018/31/B/ST8/03390 “Advanced scintillation and thermoluminescence detectors based on the epitaxial structures of garnet and orthosilicate compounds”. The research, carried out by the doctoral candidate as the executor and scholarship recipient of the mentioned projects, was conducted at the Chair for Optoelectronic Materials, Faculty of Physics of Kazimierz Wielki University in Bydgoszcz.

NARODOWE CENTRUM NAUKI

Introduction

The relevance of the topic. Ce^{3+} and other rare-earth ions doped garnet phosphors have emerged as one of the most promising materials for use in white light-emitting diodes (WLEDs). WLEDs are widely used in a variety of lighting applications, including automotive lighting, display backlighting, and general illumination. Ce^{3+} doped garnet phosphors are the type of materials that have unique optical properties, such as high thermal stability, excellent color rendering, and high quantum efficiency. These properties make them an ideal choice for use in WLEDs, as they can provide high-quality white light with high efficiency and long lifetimes. Additionally, Ce^{3+} doped garnet phosphors have high luminous efficacy, which means they can produce more light with less energy compared to other phosphors [1-5].

Another advantage of Ce^{3+} doped garnet phosphors is their excellent thermal stability, which allows them to maintain their optical properties even at high temperatures. This makes them ideal for use in high-power LED applications, where heat management is crucial for maintaining long lifetimes and high performance. With ongoing research and development, Ce^{3+} doped garnet phosphors in different crystalline forms (powders, films, ceramics and crystals) are expected to play an increasingly important role in the future of lighting technology [6].

The elastic and mechanical properties of garnet crystals play also a critical role in the performance of white light-emitting diodes (WLEDs) that utilize garnet phosphors. To optimize the performance of WLEDs, it is also necessary to consider the elastic and mechanical properties of garnet crystals. When a WLED is subjected to mechanical stress or thermal expansion, the strain on the garnet crystal can alter its electronic structure and reduce or increase the efficiency of light emission [7]. Therefore, it is important to use garnet crystals with appropriate elastic properties that can maintain their optical properties even under external stress [8]. In particular, the mechanical strength and hardness of the garnet crystals can affect their resistance to cracking, fracturing, and other forms of damage that can occur during the fabrication, packaging, and operation of WLEDs. This is especially important for high-power LED applications, where the WLEDs are subjected to high thermal stress. By carefully selecting and engineering the properties of the garnet crystals, it is possible to create high-performance WLEDs with superior optical efficiency, stability, and durability.

LPE (Liquid Phase Epitaxy) is a widely used technique for the growth of high-quality single-crystalline films of garnet phosphors. LPE is a liquid-phase method, which is based on the controlled nucleation and growth of films from a solution or melt of the desired material. In recent years, LPE-grown single-crystalline films (SCF) of different garnet compounds have emerged as promising converters for WLEDs [9, 10]. Moreover, LPE grown films have several advantages over conventional powder-based phosphors, such as high uniformity, controlled thickness, and the possibility of integrating with microelectronics.

LPE-grown SCFs of garnet phosphors can be used as color converters for WLEDs by placing them on the blue-emitting LED chips. Various types of garnet phosphors, such as $Y_3Al_5O_{12}$ (YAG, Yttrium Aluminium Garnet), $Lu_3Al_5O_{12}$ (LuAG, Lutetium Aluminum Garnet), $Gd_3Ga_5O_{12}$ (GGG, Gadolinium Gallium Garnet), and others garnet compounds, have been successfully grown using the LPE technique. These phosphors can be doped with rare earth ions like Ce^{3+}, Eu^{3+}, Dy^{3+}, and Tb^{3+}, which exhibit strong luminescence in the visible and near-infrared spectral ranges [11]. The color of the emitted light can be tuned by adjusting the composition and doping level of the phosphor.

The research on LPE-grown SCFs of Ce^{3+} doped garnet phosphors and composite structures on their base show great potential for use in WLEDs, owing to their high luminescence efficiency, excellent thermal stability, and good color rendering properties [12, 13]. Therefore, the research on the optimization of the growth parameters and improvement of material performance of these film phosphors for practical applications is highly relevant.

The acoustic methods are widely used techniques for measuring the elastic properties of crystals and multilayered epitaxial structures. This non-destructive method is based on the measurement of sound wave velocity, which is directly related to the elastic modulus of the material. The method applies to both isotropic and anisotropic materials. In the case of multilayered epitaxial structures, the acoustic method can be used to measure the elastic properties of individual films as well as the interfacial properties between the films [14]. This is important for understanding the mechanical stability and performance of these structures, as well as for optimizing their design.

Research goals. This PhD thesis is focused on the investigation of the structural, elastic, luminescent, and photoconversion properties of Ce^{3+} doped garnet-based epitaxial structures for phosphor converters in WLEDs. Based on the properties of the LPE grown epitaxial structures of selected garnet compounds, the Author aimed to enhance the understanding of the behavior of garnet-based materials as phosphor converters in WLEDs and contribute to their optimization for efficient and reliable lighting applications. The study aims to explore the potential of garnet single crystalline films and film-crystal composite structures as efficient and reliable phosphor converters for WLEDs.

Achieving the stated objective requires addressing **the main scientific tasks:**

1) *LPE growth of film color converters*. The Ce^{3+} doped LuAG, TbAG:Ce, and $Tb_{1.5}Gd_{1.5}AG$ SCFs were grown using the LPE method onto undoped YAG substrates.

2) *LPE growth of composite film-crystal color converters*. The Ce^{3+} doped LuAG:Ce, TbAG:Ce and $Tb_{1.5}Gd_{1.5}AG$:Ce SCFs were grown using the LPE method onto YAG:Ce substrates with different thickness and Ce^{3+} concentrations.

3) *Optimization of the technological conditions*. This investigation explores how the ratio of SCF-forming oxides to flux components, growth temperature, super-cooling rate of the melt-solution, and the velocity of SCF growth affect the quality of film converters.

4) *Structural investigation* of the films and composite converters including optical microscopy, scanning transmission electron microscopy (STEM), and X-ray diffraction (XRD) analyses.

5) In the scope of theoretical and numerical research, a microscopic layered model of the epitaxial structure was developed to describe the *propagation of ultrasonic waves* (with wavelengths comparable to the thickness of the layer).

6) With the aim of experimental confirmation of the developed model, the studies were conducted using *ultrasonic microscopy* of YAG:Ce substrate and LuAG:Ce SCF/YAG:Ce substrate epitaxial structures at various frequencies.

7) An *optimization-based algorithm* was used to identify the mechanical (elastic) properties of the investigated film and substrate based on the microscopic model of wave propagation, numerical analysis, and the results obtained from ultrasonic measurements.

8) *Investigation of the optical properties* of film and composite converters including measurements of their absorption, cathodoluminescence (CL) and photoluminescence (PL) spectra.

9) *Investigation of photoconversion properties* of film and composite converters including measurements of color coordinates (CC), color temperature (CCT), color rendering index (CRI), and luminous efficacy (LE).

Research objects:

1) Film converters based on the Ce^{3+} doped LuAG:Ce, TbAG:Ce and $Tb_{1.5}Gd_{1.5}$AG:Ce SCFs, grown using the LPE method onto undoped YAG substrates.
2) Composite film-crystal converters based on the Ce^{3+} doped LuAG:Ce, Tb_3AG:Ce and $Tb_{1.5}Gd_{1.5}$AG:Ce SCFs, grown using the LPE method onto YAG:Ce substrates.

Research methods

SCFs and film-crystal composite structures were obtained by the LPE method. The structural properties were investigated using XRD and STEM. Elastic properties were determined using acoustic microscopy and the V(z) curve technique. The results were optimized using a genetic algorithm. The optical characteristics of the film and composite converters were determined using absorption and luminescence spectroscopies. Their photoconversion properties were investigated under the excitation of the blue LED.

The scientific novelty of the obtained results

1) LPE growth of the experimental sets film and composite converters based on the SCFs of LuAG:Ce, TbAG:Ce and TbGdAG:Ce garnets onto YAG and YAG:Ce substrates, with different film and substrate thickness and content of Ce dopant.
2) Using ultrasonic microscopy to study epitaxial structures.

3) Development of a microscopic layered model of epitaxial structure for the description of ultrasonic wave propagation. The optimization procedure showcases a novel approach employed to determine the elastic properties of LuAG:Ce SCF.

4) The study's key scientific contribution is the discovery of composition transition layers (TL) at the interface between SCF and YAG substrate.

5) Investigation of the absorption and photoluminescence properties of film and composite converters. In addition, the dependence of photoconversion properties on the film thicknesses was studied.

6) Application of epitaxial structures of selected Ce^{3+} doped garnet compounds as efficient color converters for WLED.

Personal contribution of the author

The formulation of the work tasks was performed by the Supervisor and Co-Supervisor with the participation of the Author, and the main experimental results were obtained personally by him. The Author actively participated in the process of adjusting the growth of the samples, which arose from the express testing of their photoconversion properties. Specifically, the Author's contribution involves direct participation in all experiments related to the investigation of absorption, luminescence photoconversion, and elastic properties of film and film-crystal color converters for WLEDs. The analysis of literature data, arrangements of experimental results, and formulation of conclusions in the dissertation work were carried out personally by the Author, in consultations with the Supervisor and Co-Supervisor.

The experimental data from acoustic microscopy were obtained by prof. J. Litniewski from the Institute of Fundamental Technological Research Polish Academy of Sciences in Warsaw and his group, the interpretation of the results and the optimization procedure were carried out by Co-Supervisor, dr hab. Michał Pakula with the participation of the Author.

The Author also participated in the preparation of all 6 articles for publication, included in this dissertation. In these articles, author performed the absorption, photoluminescence and photoconversion measurements of samples, analyzed experimental materials, and wrote the manuscripts. Also Author participated in the processes of the SCFs growth by the LPE method under the leadership of dr. Vitalii Gorbenko. The author analyzed and processed the original data of the XRD measurements performed by dr Alexander Fedorov from the Institute of Single Crystal Academy of Science of Ukraine. The samples for HR STEM measurements were prepared by mgr J. Elia from prof. M. Batentschuk group, when the HR STEM measurements were performed by dr T. Yokosawa and dr J. Will from prof. E. Spiecker group; meanwhile the results of this research were analyzed and

described by the Author in articles [A1 A2]. Dr hab. M. Pakuła and prof. M. Kaczmarek described a mechanical model based on the structural results [A1], prof. Ph.D. Yuri Zorenko developed the concept of the works, analyzed the research results as a whole, and corrected the final versions of the manuscripts.

Approbation of dissertation results

The author presented the main results of this work at the following international conferences and workshops:

1) 8th International Symposium on Optical Materials (IS-OM), 9-14.06.2019, Wroclaw, Poland.

2) DESY Photon Science Users' Meeting 2020/European XFEL Users' Meeting 2020, 28-31.01.202, Hamburg, Germany.

3) 20th International Conference on Defects in Insulating Materials (ICDIM 2020), 23-27.11.2020, an online conference hosted by the Federal University of Sergipe, Brazil.

4) 11th International Conference on Luminescent Detectors and Transformers of Ionizing Radiation (LUMDETR). 12-17 September 2021, Bydgoszcz, Poland.

5) 5th International Conference on Oxide Materials for Electronic Engineering (OMEE), September 28 - October 2, 2021, Lviv, Ukraine.

6) 9th International Conference on Optical, Optoelectronic and Photonic Materials and Applications & 14th Europhysical Conference on Defects in Insulating Materials (ICOOPMA-EuroDIM 2022), 3-8 July 2022, Ghent University, Ghent, Belgium.

7) The 8th International Workshop on Advanced Spectroscopy and Optical Materials (IWASOM) 2022, 10-15.07. 2022, Gdansk University, Gdańsk, Poland.

8) International Conference on Excited States of Transition Elements (ESTE 2023), 3-8.09.2023, Świerardów Zdrój, Poland.

Articles: The main results of the dissertation have been published in **6 articles** in specialized journals relevant to the research topic (**A list of references**).

[A1] **A. Markovskyi**, V. Gorbenko, T. Yokosawa, J. Will, E. Spiecker, M. Batentschuk, J. Elia, A. Fedorov, M. Pakuła, M. Kaczmarek, Y. Zorenko, Structural, luminescence and photoconversion properties of $Lu_3Al_5O_{12}$:Ce single crystalline film phosphors for WLED application, J. Alloys Compd. 929 (2022) 167159.

[A2] **Markovskyi**, A., Gorbenko, V., Zorenko, T., Yokosawa, T., Will, J., Spiecker, E., Batentschuk, M., Elia, J., Fedorov, A., & Zorenko, Yu. LPE growth of $Tb_3Al_5O_{12}$:Ce single crystalline film converters for WLED application. CrystEngComm, 23(17), 3212–3219.

[A3] **A. Markovskyi**, V. Gorbenko, T. Zorenko, K. Bartosiewicz, A. Fedorov, Y. Zorenko, Development of $Tb_{1.5}Gd_{1.5}Al_5O_{12}$:Ce single-crystalline film converters for WLED using a liquid phase epitaxy growth method, Crystals (MDPI). 12 (2022) 1814.

[A4] **A. Markovskyi,** V. Gorbenko, T. Zorenko, A. Fedorov, Yu. Zorenko. Development of $R_3Al_5O_{12}$:Ce (R=Lu, Y, Tb, Gd) single crystalline film color converters for white LEDs using liquid phase epitaxy growth method, submitted to Journal of Luminescence, 2023. Manuscript No: LUMIN-D-23-01439.

[A5] **A. Markovskyi,** V. Gorbenko, T. Zorenko, S. Nizhankovskiy, A. Fedorov, Y. Zorenko, Composite Color Converters Based on $Tb_3Al_5O_{12}$:Ce Single-Crystalline Films and $Y_3Al_5O_{12}$:Ce. Crystal Substrates, Phys. Status Solidi RRL (2021) 2100173.

[A6] **A. Markovskyi,** V. Gorbenko, S. Nizhankovskiy, T. Zorenko, M. Pakula, M. Kaczmarek, A. Fedorov, Yu. Zorenko, Novel composite color converters based on $Tb_{1.5}Gd_{1.5}Al_5O_{12}$:Ce single crystalline films and $Y_3Al_5O_{12}$:Ce crystal substrates, CrystEngComm. 24 (2022) 4975–4982.

This dissertation **does not include** the results of the other nine articles that have been published on this research topic **(list B of references).**

[B1] Wojciech Gieszczyk, Paweł Bilski, Anna Mrozik, Alexander Fedorov, **Anton Markovskyi,** Tetiana Zorenko, Yuriy Zorenko. Luminescent, scintillation and photoconversion properties of MPD grown single crystals of Ce^{3+} doped $Gd_{3-x}Lu_xAl_{5-y}Ga_yO_{12}$ garnets, Physica status solidi (b), 275 (2020) 1900429.

[B2] **A. Markovskyi,** W. Gieszczyk, P. Bilski, A. Fedorov, K. Bartosiewicz, K. Paprocki, T. Zorenko, Y. Zorenko, Composition engineering of $Tb_{3-x}Gd_xAl_{5-y}Ga_yO_{12}$:Ce single crystals and their luminescent, scintillation and photoconversion properties, Journal of Alloys and Compounds, 849 (2020) 155808.

[B3] K. Bartosiewicz, **A. Markovskyi,** A. Yoshikawa, S. Kurosawa A. Yamaji, T. Zorenko, Y.Zorenko, New efficient scintillating and photoconversion materials based on the self-flux grown $Tb_3Al_5O_{12}$:Ce single crystal, Phys. Status Solidi RRL**,** 14 (2020) 2000327.

[B4] **A. Markovskyi**, W. Gieszczyk, P. Bilski, A. Fedorov, T. Zorenko, Yu. Zorenko, MPD growth of single crystals of Ce^{3+} doped $Gd_{3-x}Lu_xAl_{5-y}Ga_yO_{12}$ mixed garnets and their luminescent, scintillation and photoconversion properties, Materials Science and Engineering: B. 262 (2020) 114751.

[B5] **A. Markovskyi**, K. Bartosiewicz, W. Chewpraditkul, K. J. Kim, S. Witkiewicz-Lukaszek, T. Zorenko, W. Chewpraditkul, A. Yoshikawa, Yu. Zorenko. Development of novel scintillation and photo-conversion materials based on $Gd_3(Sc,Al,Ga)_5O_{12}$:Ce single crystals grown by micro-pulling-down method. Materials Science and Engineering: B. 273 (2021) 115395.

[B6] K. Bartosiewicz, **A. Markovskyi**, T. Horiai, D. Szymański, S. Kurosawa, A. Yamaji, A. Yoshikawa, Y. Zorenko, A study of Mg^{2+} ions effect on atoms segregation, defects formation, luminescence and scintillation properties in Ce^{3+} doped $Gd_3Al_2Ga_3O_{12}$ single crystals, Journal of Alloys and Compounds. 905 (2022) 164154.

[B7] A. Shakhno, **A. Markovskyi**, T. Zorenko, S. Witkiewicz-Łukaszek, Y. Vlasyuk, A. Osvet, J. Elia, C.J. Brabec, M. Batentschuk, Y. Zorenko, Micropowder $Ca_2YMgScSi_3O_{12}$:Ce Silicate Garnet as an Efficient Light Converter for White LEDs, Materials, 15 (2022) 3942.

[B8] W. Dewo, V. Gorbenko, **A. Markovskyi**, Y. Zorenko, T. Runka, Photoconversion, luminescence and vibrational properties of Mn and Mn, Ce doped $Tb_3Al_5O_{12}$ garnet single crystalline films, Journal of Luminescence, 254 (2023) 119481.

[B9] A. Markovskyi, V. Gorbenko, T. Zorenko, S. Witkiewicz-Lukaszek, O. Sidletskiy, A. Fedorov, Y. Zorenko, Development of three-layered composite color converters for white LEDs based on the epitaxial structures of YAG:Ce, TbAG:Ce and LuAG:Ce garnets, Materials, 16 (2023) 1848.

Patents

Patent application EU EP 3831911A1 „Composite wavelength conventer", Applicants: Fridrich-Alexander University-Erlangen-Nurnberg, Germany and Kazimierz Wielki University in Bydgoszcz, Poland. Inventors: Yu. Zorenko, M. Batentschuk, C. Brabec, A. Osvet, V. Gorbenko, I. Levchuk, T. Zorenko, L. Chepyga, **A. Markovskiy,** S. Witkiewicz-Lukaszek. Date of publication 09.06.2021; Bulletin 2021/23. Priorities EP19213887A·2019-12-05*;* Application EP19213887A·2019-12-05*;* Publication EP3831911A1·2021-06-09.

Structure of a dissertation: The structure of a dissertation includes an introduction, 7 chapters, conclusions, and a list of used references. The total volume of the dissertation is 131 pages, with 71 figures, 11 tables, and a reference list of 166 literary sources.

Chapter 1. Ce^{3+} doped garnet phosphors

1.1 Garnet crystal structure

Garnets have been widely used since the Bronze Age. Due to their high refractive index and charming coloring caused by the incorporation of transition metal ions, garnets have been used as gemstones and abrasives for thousands of years. When Menzer assigned the garnet structure to the cubic with *Ia*3*d* symmetry in 1928, the scientific study of compounds with garnet-like properties began [15]. In a unit cell, there are eight molecules with the stoichiometric formula $\{A_3\}[B_2](C_3)O_{12}$, where A, B, and C are cations occupying different symmetry sites, which is shown in Fig. 1.1.

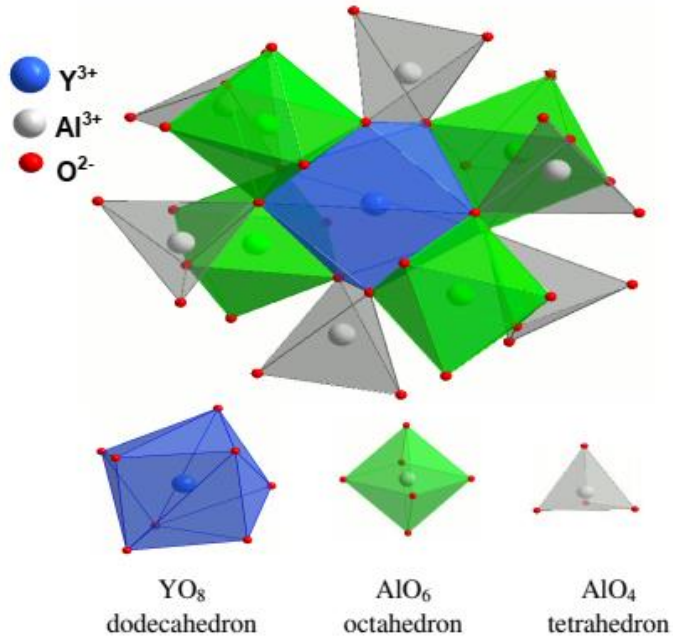

Fig.1.1. Fragment of garnet crystal structure $\{A_3\}[B_2](C_3)O_{12}$ showing dodecahedron {A} sharing edges with two tetrahedra [B] and four octahedra (C).

The A, B, and C atoms are (8-fold) dodecahedrally, (6-fold) octahedrally, and (4-fold) tetrahedrally coordinated to the O atoms of the garnet structure, respectively. The dodecahedral AO_8 polyhedron, which can be regarded as a tetragonally distorted cube, shares the coordinating O atoms with two neighboring CO_4 tetrahedra and four BO_6 octahedra. Since the oxygen sublattice in the garnet crystal structure exhibits high flexibility, the oxygen anions can readily fit the size of the enclosed cations. Because of this, the garnet phosphors are unique in their tunability of the luminescence properties by full or partial variations of cations in the {A}, [B], and (C) cation sublattice.

The large Lu^{3+}, Y^{3+} , Tb^{3+}, Gd^{3+} or Ca^{2+} cations and co-doping rare earth (*RE*) ions (Ce^{3+}, Nd^{3+}, Pr^{3+}, etc.) are localized in dodecahedral sites{A}; medium size Al^{3+}, Ga^{3+}, Sc^{3+} or Mg^{2+} cations occupy octahedral sites [B]; and Al^{3+} and Ga^{3+} ions and relatively small size Si^{4+} and Ge^{4+} cations, are localized

preferable in (C)-tetrahedral sites, respectively [16]. However, for *RE* ions larger than Gd^{3+} (Table 1), the $REAlO_3$ perovskite phase is usually more stable than the $RE_3Al_5O_{12}$ garnet phase at the crystallization of the material from the melt [17,18]. Therefore, the synthesis of Gd-based garnets usually is stabilized in two ways: (i) by partial substitution of Gd^{3+} by Y^{3+} or Lu^{3+}, (ii) by the introduction of Ga^{3+} or Sc^{3+} ions into the garnet matrix replacing the Al^{3+} ions in octahedral and tetrahedral sites [19].

Table 1.1 Ionic radii and electronegativity of some ions depending on the coordination environment. CN - anion coordination [20].

	Gd^{3+}	Y^{3+}	Tb^{3+}	Lu^{3+}	Sc^{3+}	Ce^{3+}	Ce^{4+}	Ga^{3+}	Al^{3+}
Dodecahedral (CN=8)	1.06	1.02	1.05	0.97	0.87	1.14	0.97		
Octahedral (CN=6)	0.94		0.93	0.86	0.75	1.01	0.8	0.62	0.53
Tetrahedral (CN=4)								0.47	0.39
Electronegativity	1.2	1.2	1.2	1.3	1.3	1.1	1.1	1.8	1.6

In the past few decades, aluminum garnets $RE_3Al_5O_{12}$ (RE = Y, Lu, Tb, Gd) have been comprehensively studied around the world due to their multifunctional applications in lasers, magnetooptical devices, scintillation detectors as well as phosphors in lighting sources [21-24]. For example, yttrium aluminum garnet YAG has been widely used in medicine and industry as a solid-state laser host material, since its discovery in 1964. This was facilitated by the rare-earth ion's ideal spectroscopic properties in YAG crystal, as well as its good mechanical properties (hardness and general stability against chemical and mechanical changes), good thermodynamic properties (low thermal expansion and high thermal conductivity), and good optical properties (high-optical transparency, high threshold for optical damage) [25,26]. The Ce^{3+} doped yttrium aluminum garnet YAG:Ce, prepared in different forms: bulk single crystals (SC), single crystalline films (SCF), and transparent optical ceramics (OC), powders are widely applied nowadays as cathodoluminescent screens [27], scintillators [28], screens for the visualization of X-ray images [29], luminescent converters in white light emitting diodes [30], and other optoelectronic devices [31]. Numerous applications of Ce^{3+}-doped garnets have been based on their exceptional ability to combine a short-lived (ns decay time) efficient yellow emission with strong absorption in the blue spectral region.

The advances in modern crystal growth technology have paved the way for the development of garnet materials that possess unique properties and exceptional optical quality. To engineer devices incorporating garnet materials effectively, it becomes important to have a comprehensive understanding of their mechanical, thermophysical, and acoustooptical properties. It is well-established that these properties are intricately linked to the elastic and photoelastic constants of the garnet crystals [32] (Fig. 1.2).

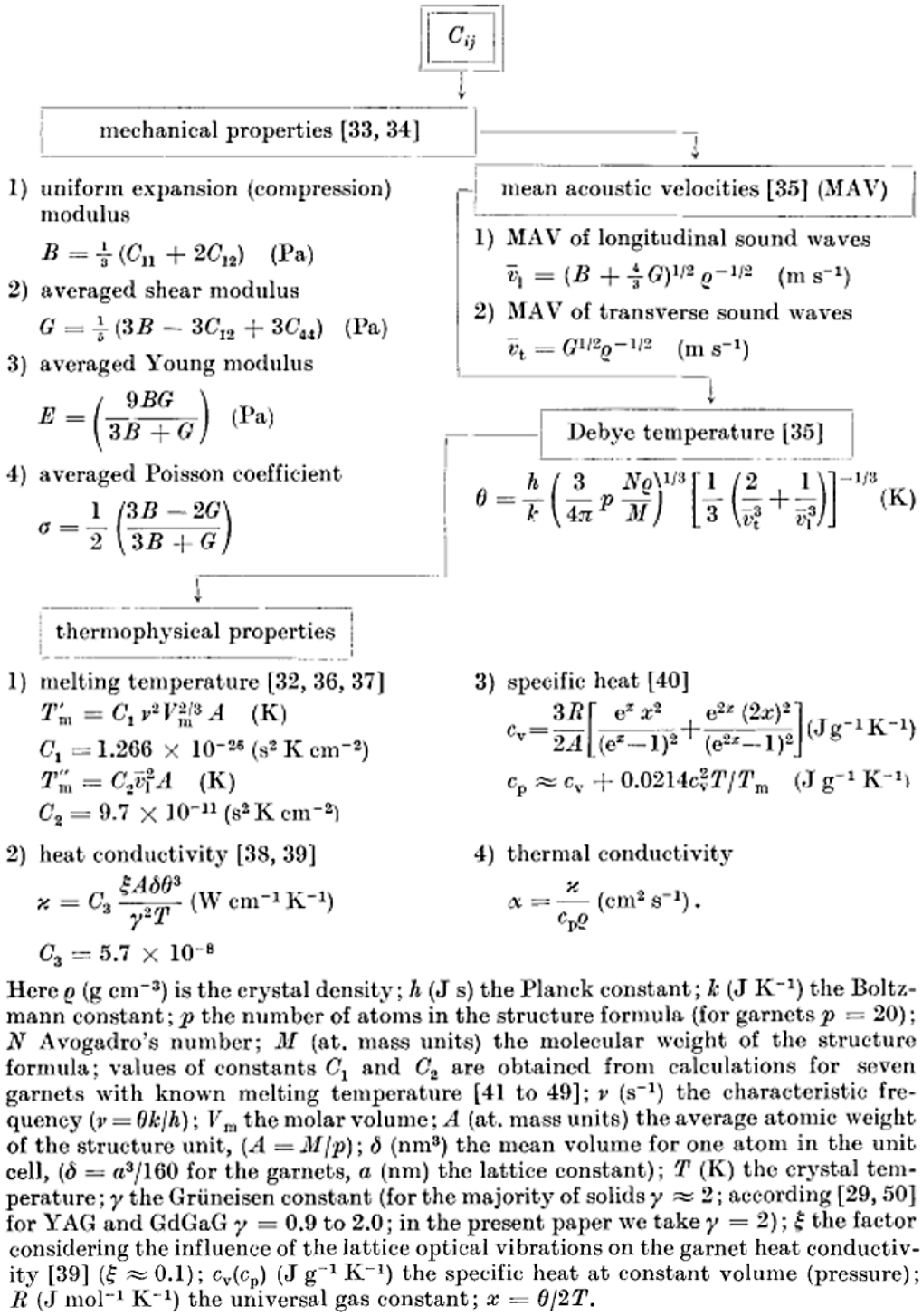

Here ϱ (g cm^{-3}) is the crystal density; h (J s) the Planck constant; k (J K^{-1}) the Boltzmann constant; p the number of atoms in the structure formula (for garnets $p = 20$); N Avogadro's number; M (at. mass units) the molecular weight of the structure formula; values of constants C_1 and C_2 are obtained from calculations for seven garnets with known melting temperature [41 to 49]; ν (s^{-1}) the characteristic frequency ($\nu = \theta k/h$); V_m the molar volume; A (at. mass units) the average atomic weight of the structure unit, ($A = M/p$); δ (nm^3) the mean volume for one atom in the unit cell, ($\delta = a^3/160$ for the garnets, a (nm) the lattice constant); T (K) the crystal temperature; γ the Grüneisen constant (for the majority of solids $\gamma \approx 2$; according [29, 50] for YAG and GdGaG $\gamma = 0.9$ to 2.0; in the present paper we take $\gamma = 2$); ξ the factor considering the influence of the lattice optical vibrations on the garnet heat conductivity [39] ($\xi \approx 0.1$); $c_v(c_p)$ (J g^{-1} K^{-1}) the specific heat at constant volume (pressure); R (J mol^{-1} K^{-1}) the universal gas constant; $x = \theta/2T$.

Fig.1.2. Garnet properties derived from elastic constants [32].

1.2 Luminescence of Ce^{3+} ion in garnet host

The phenomenon known as luminescence is when atoms spontaneously emit photons to return to their ground state after being promoted into excited states by absorbing photons of the appropriate energy. To describe the luminescence of ions in the crystal matrix, it is convenient to use the electronic (Fig.1.3a). For dielectrics and semiconductors, the unfilled conduction band - (CB) and filled valence band (VB) are separated by a forbidden energy band with a width E_g [33]. The value of

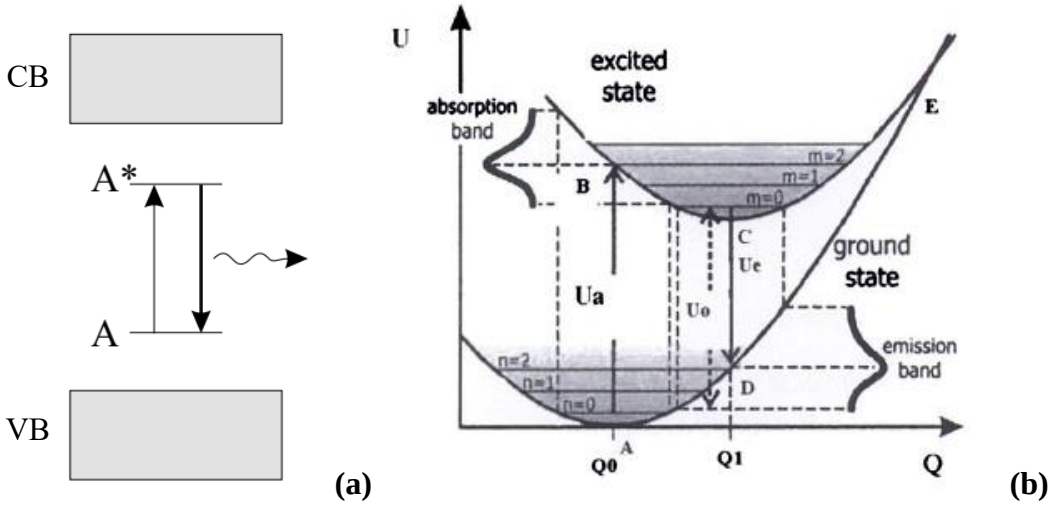

Fig.1.3. (a) - band structure model of luminescence process of activator in solids; (b) - configurational coordinate diagram of activator [36].

E_g determines whether the crystal belongs to dielectrics or semiconductors. It is considered to be that that for semiconductors $E_g < 3$ eV and in turn for typical dielectric crystals E_g is ~ 8 eV (for example, NaCl, KCl, etc.). For aluminum garnets, which are dielectrics, this E_g is the range from ~5.5 to ~8.5 eV depending on the cation content [34, 35]. Crystals with wide band gaps are favorable for their activation by different cations.

For wide-gap crystals, the energy zones of the ground and excited states of the activator are placed in the band gap. The energy levels of the activator (luminescence centers) are depicted by separate lines on the band diagram of the crystal phosphor. Such centers contain the ground and at least one excited level and the relaxation of the electron from the excited level occurs with the emission of a photon. Fig.1.3a shows the occurrence of radiative transitions upon direct excitation of a discrete center.

However, for the explanation of the luminescence phenomenon, the model of configuration curves developed by Mott and Seitz is more useful (Fig.1.3b). It allows for the representation of both the difference in wavelength between absorption and emission, as well as the difference in the half-widths of absorption and emission peaks, and a series of other phenomena. However, it has a drawback as it ignores the charge transport through the crystal lattice.

In this model, particular attention is paid to the interaction between the luminescent ion and its surroundings. The luminescent ion and its neighboring ions are selected as a system, neglecting the influence of other distant ions. In this way, a large number of real vibrations are approximated by a small number or a combination of specific normal coordinates-configuration coordinates (Q). They determine the distances between the luminescent ion and its neighbors and their deviations from the equilibrium position. It is assumed that the binding force between atoms in the lattice can be expressed by Hooke's law. Configuration curves are obtained by plotting the potential energy as a function of

configuration coordinates (although, for simplicity, usually only one configuration coordinate is considered). The graph always shows two configuration curves, one for the ground state (Ug) and another for the excited state (Ue) (Fig 1.3b) [36].

The total energies of the ground and excited states can be expressed as:

$$U_g = K_g \frac{Q^2}{2}$$

$$U_e \approx K_e \frac{(Q-Q_0)^2}{2} + U_0 \quad (1.1),$$

where K_g and K_e are the force constants of the chemical bond, Q_0 is the distance between atoms at the equilibrium position for the ground state, and U_0 is the energy difference between the lowest possible vibrational level of the excited state (m=0) and the lowest possible vibrational level of the ground state (n=0).

The spatial distribution of electron orbitals is different for the ground state and the excited state. This results in the formation of different electronic wavefunctions that interact differently with neighboring ions. This, in turn, affects the change in the equilibrium position of the excited state. According to the Franck-Condon principle, throughout the entire process of excitation and relaxation, atomic nuclei do not change their positions. This is justified by the significant difference in mass between the nucleus and the electron [37].

An example process of absorption and emission can proceed as described below. The absorption process begins at the equilibrium point of the ground state, Q_0 (A). From the vibrational level of the ground state, n=0, excitation occurs to the vibrational level of the excited state, m=2 (B). The excited electron can lower its energy in two ways. The first possibility is the generation of lattice vibrations called phonons. The probability of such an event is about 10^{12}~10^{13} s^{-1}. The second possibility is the emission of a photon of light. The probability of photon emission depends on the type of emitting center and is less than 10^9 s^{-1}. Therefore, first, non-radiative relaxation occurs back to the equilibrium point of the excited state, m=2 → m=0 (C). Then, the electron returns to the ground state, accompanied by photon emission (C – D). Before the cycle is complete, another non-radiative relaxation occurs (D – A). When the emitted photon has less energy than the absorbed photon, this energy difference is the Stokes shift ΔS.

Configuration curves can intersect with each other. In such a case, the electron in the excited state can transition to the ground state non-radiatively with the help of thermal energy (E).

The RE ions, which include the group lanthanides (Ln), are the largest group of luminescent centers used for production in light emitting materials for technological applications. The Ln^{3+} ions have the following electron configuration: $4f^n5s^25p^6$, where n is the number of electrons in the 4f inner shell, which can range from 0 for La (an empty 4f shell) to 14 for Lu (filled 4f shell) [38].

Among the luminescent RE ions with number n>1, the Ce^{3+} ion has the simplest electron configuration $4f^1$. The luminescence properties of Ce^{3+} result from optical transitions between the $4f^1$ ground state and the $5d^1$ excited state. The electronic energy levels of a free Ce^{3+} ion undergo significant modifications when it interacts with its nearest neighboring atoms in a host crystal, resulting in substantial differences compared to a free Ce^{3+} ion. The energy difference between the 4f ground state and the 5d excited state of a free Ce^{3+} ion is around 6.12 eV. However, when this free Ce^{3+} ion is placed within a garnet crystal, this energy gap undergoes a significant reduction.

The decrease in the energy gap between the 4f and 5d states, known as the red-shift D(A) for a specific host A, is primarily determined by two factors: ***the centroid shift and the crystal field splitting*** within the energy levels of the 5d state (Fig. 1.4). The energy levels within the 4f state of the Ce^{3+} ion are predominantly governed by the influence of spin−orbit coupling (s/o), which splits the 4f state into two energy levels $^2F_{5/2}$ and $^2F_{7/2}$.

The centroid shift pertains to the lowering of the average energy of the 5d levels of Ce^{3+}—commonly referred to as the barycenter. This reduction arises as a consequence of diminished interelectronic repulsion, denoted as ε_c in Figure 1.4. The determination of the centroid shift can be derived from the (degeneracy-weighted) position of all 5d levels of Ce^{3+}, obtained through spectroscopic data analysis [34].

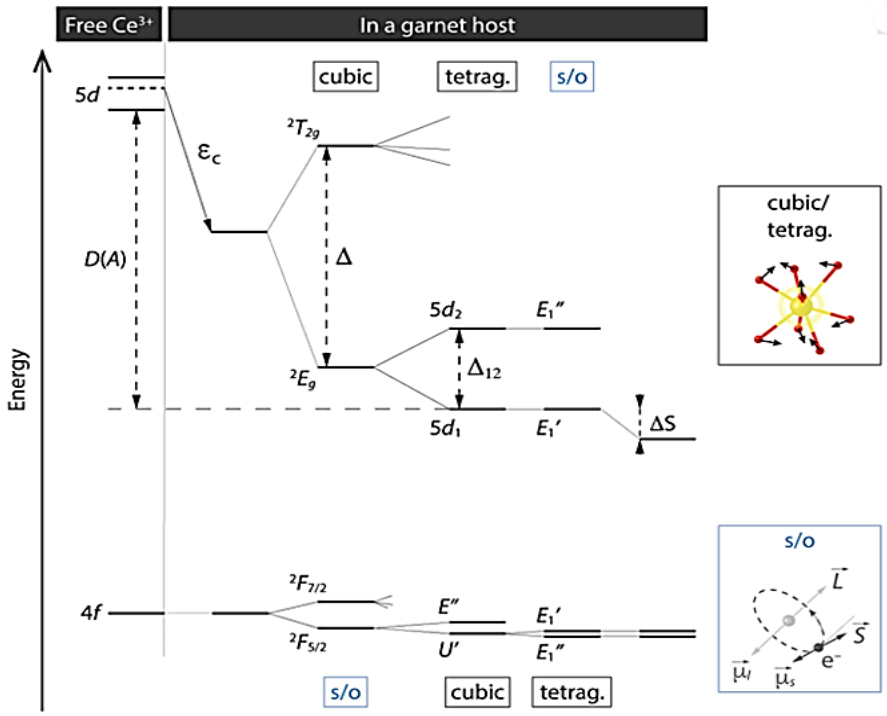

Fig. 1.4. Energy diagram of the 4f ground and 5d excited electronic configurations of the Ce3+ ions in a garnet host. The energy levels associated with the coordination symmetry splitting are denoted as U', E'', E_1', and E_1'' [39].

The covalency of the chemical bonds between the surrounding anion (oxygen) ligands and the activator ion, as well as the polarizability of the anion ligands themselves, determine the strength of this effect. The centroid shift increases with an increase in the polarizability of the anion and a decrease in the average electronegativity of the matrix cations. The level of the effect of the centroid shift can be characterized by the nephelauxetic ratio β as:

$$1 - \beta = hk, \tag{1.2}$$

where 1-β is written as a product of two functions, each variable. h characterizes the anion ligands and k the metal. Changes in the chemical nature can affect the covalency of the bonds as well as the positions of the valence band (VB) and conduction band (CB) edges of the host when one constituent element of the host crystal is replaced by another element of a different ionic radius.

In a highly symmetric coordination environment, such as octahedral or cubic, the ***crystal field splitting*** refers to the energy difference between the highest and lowest 5d levels and is again an effect of the host crystal. In the context of a simple point charge model, it has been demonstrated that the crystal field splitting exhibits variation as follows: [34,40]:

$$D_q = \frac{1}{6} Ze^2 \frac{r^4}{R^5}, \tag{1.3}$$

In the equation above, D_q is a measure of the crystal field strength, R is the distance between the central ion (Ce^{3+}) and its ligands (neighboring oxygen anions), Z is the charge or valence of the coordinating anions, e is the charge of an electron, and r is the radius of the d wave function.

The crystal field splitting reaches its maximum in octahedral coordination (10Dq), with cubic coordination following closely behind at [(8/9) × 10Dq = Δ] (Fig. 1.4b) [41].

For a perfect cubic CeO_8 moiety, the 5d state splits into the lower-energy doublet state 5d(^2E_g) and the higher triplet state 5d($^3T_{2g}$). However, when considering the CeO_8 moiety within a garnet structure, where the originally cubic symmetry is distorted to tetragonal D_2 site symmetry, the ^2E_g level splits into two levels ($5d_1$ and $5d_2$). The unusual long wavelength emission shift for Ce^{3+} in garnets is attributed to an additional splitting Δ_{12} of the ^{2}Eg crystal field component, though this is not fully understood. The variation in the cubic coordination's distortion is primarily responsible for the changes in Δ_{12}. In this way, the host crystal's composition and structure can be changed to adjust both the excitation and emission energies. Additionally, the excitation energy arising from the 4f → $5d_1$ transition is lowered by the so-called Stokes shift ΔS.

Generally, the crystal field splitting decreases as the ionic radius of the host cation, for which the optically active ion is substituted, increases. According to Eq.1. 3, a larger cation site results in a greater cation-ligand distance, which reduces Dq. However, it has been demonstrated for Ce^{3+} in garnets that as the radius of the host cation in the dodecahedral site increases, the crystal field splitting

also increases and the emission of Ce^{3+} shifts to longer wavelengths [42]. The increased radius of ions occupying tetrahedral and/or octahedral sites causes an emission shift towards shorter wavelengths. The distortion from cubic symmetry has a greater impact on the Δ_{12} splitting than the ion-ligand distance, which provides evidence for the unexpected trends in host cation substitution on the 5d-4f emission wavelength. The very wide range of solid solution compositional variation enables tuning and optimization of optical properties concerning specific applications.

1.3 Major mechanisms of thermal quenching of luminescence in Ce^{3+}-doped phosphors

The thermal quenching observed in Ce^{3+}-doped phosphors, which exhibit 4f–5d transitions, primarily arises from one of the following three processes or a combination thereof:

- ***Nonradiative 5d → 4f Crossover Relaxation.*** In this mechanism, the excited-state electron of Ce^{3} returns to its ground state in the 4f ground state through vibrational relaxation (Fig.1.5). This transition is nonradiative, meaning it does not emit light, but instead, the excess energy is transferred to lattice vibrations (phonons). The condition for nonradiative crossover relaxation is satisfied when an ample amount of thermal energy ΔE, originating from vibrational excitation near the Ce^{3+} ion in its excited state is provided. This energy elevates the 5d electron to a position where it intersects with the potential energy curves of both the 5d and 4f states on the configurational coordinate diagram. The transition from the 5d state to the 4f state is succeeded by vibrational relaxation, a process analogous to multiphonon nonradiative relaxation observed in 4f–4f transitions.

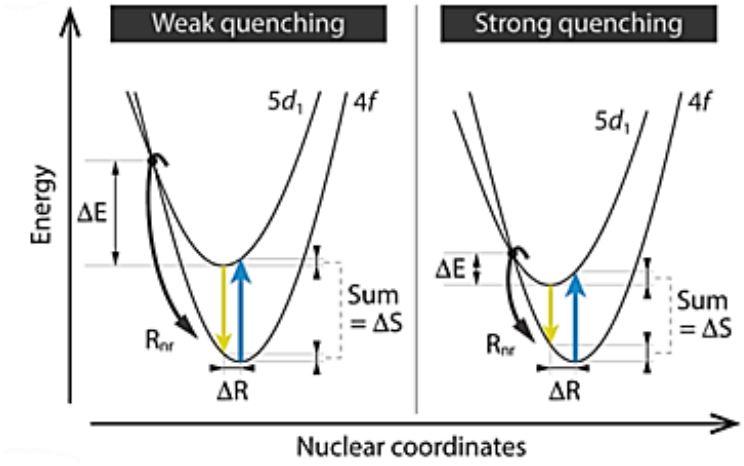

Fig.1.5. A diagram illustrating nonradiative relaxation via thermally activated crossover from the 5d1 excited state to the 4f ground state of Ce^{3+}. This process is depicted for both weak coupling (on the left) and strong coupling (on the right) [39].

Thermal Ionization of the 5d Electron into the conduction band (CB) of the host lattice, followed by charge trapping at defects. Here, the thermal energy in the system is sufficient to promote the 5d electron from Ce^{3+} to the conduction band of the host lattice. This transition occurs due to the

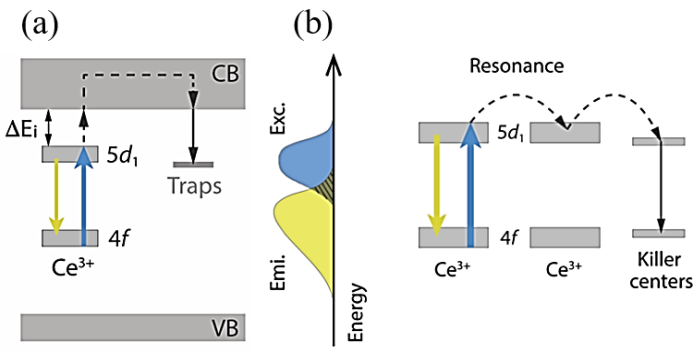

Fig. 1.6. (a) - a schematic representation depicting the thermal quenching of Ce^{3+} luminescence through thermal ionization. (b) - illustration of thermally activated concentration quenching of Ce^{3+} luminescence, with "Exc." and "Emi." denoting excitation and emission spectra, respectively [39].

increased thermal agitation at higher temperatures. Once the electron reaches the conduction band, it may subsequently become trapped at defects or impurities within the crystal lattice. These defects can serve as localized sites where the charge is immobilized (Fig. 1.6a). The trapping of charges at defects effectively reduces the number of active luminescent centers (Ce^{3+} ions), leading to a decrease in luminescence as temperature rises.

- ***Thermally Activated Concentration Quenching.*** Thermally activated concentration quenching occurs when the concentration of luminescent ions, such as Ce^{3+} ions, in the host material becomes too high. At elevated temperatures, the ions are in close proximity, leading to increased interactions between them. These interactions can result in energy transfer processes that are nonradiative and cause the luminescence to diminish. Essentially, as the ion concentration increases, the probability of nonradiative energy transfer between nearby ions also rises, leading to quenching of luminescence. The effectiveness of resonance transfer of excitation energy relies on the extent of overlap between the excitation (or absorption) and emission spectra, as depicted in Fig. 1.6b. This overlap becomes more significant as the temperature increases, mainly due to the thermal broadening of the spectra. In essence, the excitation of phonon modes by thermal energy enhances the probability of energy migration processes.

1.4 Phosphor Converted White Light Emitting Diodes

About 20% of the electricity produced in the world is used for lighting, which is a driving force for the development of new energy-efficient and eco-friendly lighting devices. The invention of blue LEDs by Nakamura and others in the middle of the 1990s pushed the development of white light sources based on inorganic phosphors [43]. Luminescence materials are indispensable components of phosphor-converted white LED (pc-WLED) devices. WLEDs are being regarded as the next

generation of solid-state lighting according to their broad application potential and advantages over conventional light sources, especially in terms of energy-saving and environmental friendliness**.**

Currently, pc-WLEDs have been considered the next generation of solid-state lighting technology to replace traditional lighting sources such as incandescent lamps, fluorescent lamps, and halogen lamps. In the past three years the average luminous efficiency for mass-market 60W LED bulbs, increased from 76 lm/W to 90 lm/W, thus in the next decade the luminous efficiency on WLED sources will be rapidly approaching the theoretical limit of 200 lm/W, while the luminous efficiency (LE) of incandescent and fluorescent lamps are 15 and 75 lm/W, respectively [44].

Three parameters are useful to define the brightness and the color emitted by WLED: luminous efficiency (LE), color rendering index (CRI), and correlated color temperature (CCT). The LE expresses how well a light source produces visible light, whereas the CRI measures quantitatively the ability of a light source to reproduce the colors of various objects. CCT is a specification of the color appearance of the light emitted by a light source, relating its color to the color of light observed from a black body radiator heated to a predetermined temperature.

The three primary colors - red, green, and blue (RGB) produced by three different LEDs could theoretically be combined to create white light (Fig.1.7a). Due to the high cost of production, this method, which makes use of numerous LED chips, has a significant drawback. The emission spectrum of RGB LEDs is determined by the emission spectrum of each constituent LED and has a distinct linear shape. This spectrum differs from the solar spectrum as a natural source of white light. The corresponding CRI of RGB LEDs is low and temperature-dependent. Since semiconductor chips have finite dimensions and directional patterns, this type of LED has non-uniform angular color characteristics. This is why it is currently preferred to use a single LED in combination with the appropriate phosphors.

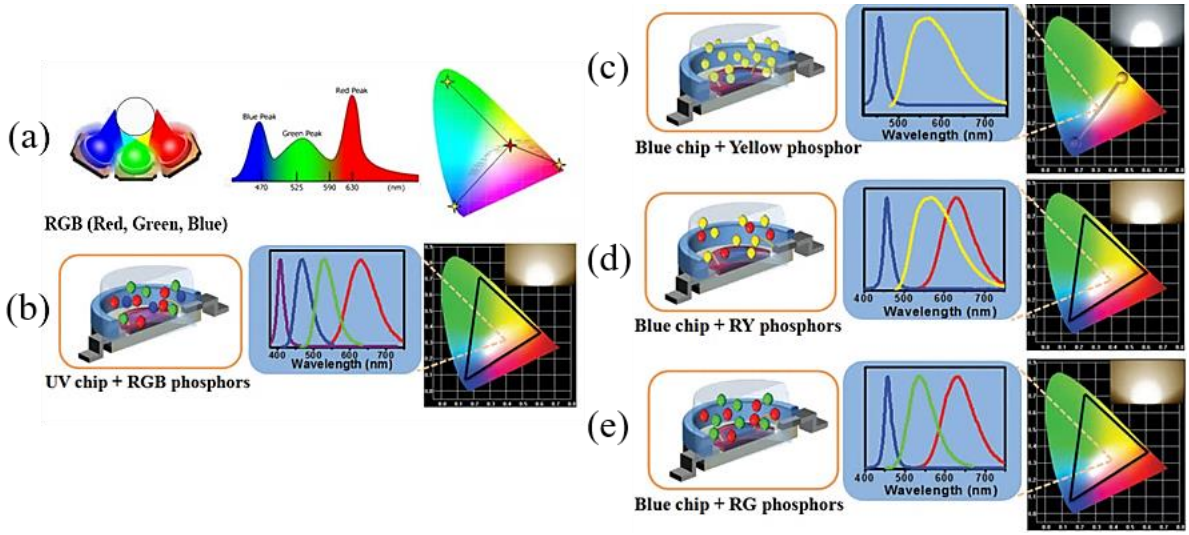

Fig.1.7 Schematics of principal white-lighting strategies of pc-WLED devices.

The second approach combines the emission from n-UV LED chips (380-420 nm) with RGB phosphors, as in the device with the schematic structure shown in Fig.1.7b. Due to the strong reabsorption of the emission of blue or green phosphors by yellow and red emitting phosphors, multi-phased phosphor converted systems frequently have low luminescence efficiency and increased manufacturing costs. In return, some advantages can be obtained, including a very high color rendering index (CRI=90), broad color gamut coverage, and stable light color output at various drive currents [45-47].

The simplest and most common approach is the combination of a 460 nm blue InGaN LED chip and a yellow phosphor in a device with a schematic structure shown in Fig. 1.7c. However, such a device has a poor color rendering index (R_a=60–70) and a high correlated color temperature (CCT= 5000–7500 K) because of the lack of a red component. The modified methods for producing white light with a high Ra and an appropriate CCT include coating yellow-emitting phosphors with a more red component (Fig.1.4 d) or admixing green and red multi-phased phosphors on 460 nm blue LEDs (Fig. 1.7e) [48].

Recently garnets, oxynitrides, silicates, and aluminates have been actively studied as host materials for converting luminescence ions. However, the main research is focused on garnet type lattices**,** such as Ce^{3+} doped YAG, and nowadays, typical WLEDs consist of YAG:Ce phosphor powders encapsulated in resins on top of a blue LED**.** The function of the phosphor converter is to absorb the blue light emitted by the LED chip and convert it to yellow light, due to the Ce^{3+} ions luminescence. The combination of the transmitted blue light and yellow Ce^{3+} emission band due to the 5d-4f transitions allows for obtaining white light. The high flexibility of the $\{Ln\}_3[M]_2(M)_3O_{12}$ (Ln= Lu, Y, Gd, Tb; M=Al, Ga, Sc) garnet structure allows for replacing ions in dodecahedral {a}, octahedral [b] and tetrahedral (c) sites, and thus, to modify the composition for optimization of the Ce^{3+} luminescence properties demanded in WLED application**.** The choice of cations allows for tuning of the local coordination environment of the luminescent ions and changes the crystal field strength and the covalence of Ce^{3+}-O^{2-} bonding, allowing to vary the Ce^{3+} emission color from the green to the orange-red spectral range. The influence of such composition engineering strategy is based on the "Ce^{3+} *5d level positioning*" [49] and "*band-gap engineering*" [50]. The shift of YAG:Ce spectrum into the red range often is carried out by (i) partial or full cationic substitution of Y^{3+} ions by larger Gd^{3+} or Tb^{3+} ions, also called *composition engineering strategy*; (ii) or codoping of YAG:Ce with red-emitting rare-earth ions (Eu^{3+}, Mn^{2+}) also known as a codoping level control tuning [6]. Such spectral tuning increases the luminescence efficiency of pc-WLEDs, optimizes the color conversion, achieves the desired color temperature, and increases the color gamut [51,52]. The widespread garnet solid solution variations enable tuning and optimization of optical, luminescence, and photoconversion properties depending on the area of application.

1.5 Planar-Chip-Level Conversion

The most common pc-WLEDs are produced using the Volume-Casting-Conversion (VCC) design, where a blue LED and powder PC are packed with organic resins [53] (Fig. 1.8a). Numerous techniques, including solid-state reactions [54], hydrothermal synthesis [55], coprecipitation [56], spray pyrolysis [57], sol-gel [58], and combustion [59], can be used to make ceramic powder phosphors. The heat generated from the LED chip and PC (Stokes shift and optical losses) cannot be efficiently dissipated because of the poor thermal stability and weak thermal conductivity of the resin (< 0.5 W m^{-} K^{-1}) [60]. With the increasing demand for high-brightness lighting, the high-power wLEDs and white laser diodes (WLDs) are rapidly developing and some limitations arise associated with the optical, structural, mechanical, and thermal properties of converters. The operating temperature of a color converter can reach even up to 200 °C under high-power LED or LD excitation. The extreme heat is generated in the converter originating from the non-radiative relaxation of phosphors and the heat transfer from high-power LED chips. With the increase of the wLED temperature, color degradation occurs because of the thermal quenching properties of the phosphor such as luminous decay and color shifting [61]. Furthermore, this setup results in low efficiency because the diffuse phosphor reflects 60% of the total white light back onto the chip [62]. To achieve high efficiency and strong chemical and thermal stability for pc-WLEDs, downconversion phosphors have been developed from powders to plates for Planar-Chip-Level Conversion (PCLC) approach [63] (Fig. 1.8b).

In PCLC design, instead of powder, the ceramic, eutectics, or single crystal phosphors based on the yellow emitting Ce^{3+} doped garnets are used for manufacturing high power WLEDs under blue LED excitation. Nevertheless, glasses and ceramics have a relatively low luminescence efficiency [65], whilst the structure and optical properties of eutectic converters are hard to control. The development of single-crystalline (SC) converters is much preferable to ceramics or powders, due to their high uniformity, and internal quantum efficiency (QE) than ceramics or glasses, as well as excellent thermal stability up to 300 °C**,** and high thermal conductivity (~10 W/(m K) [64, 66, 67].

It is obvious that the investigation of new types of color converters is an acute problem to be solved with the development of energy-efficient solid-state lighting sources. The minimization trend

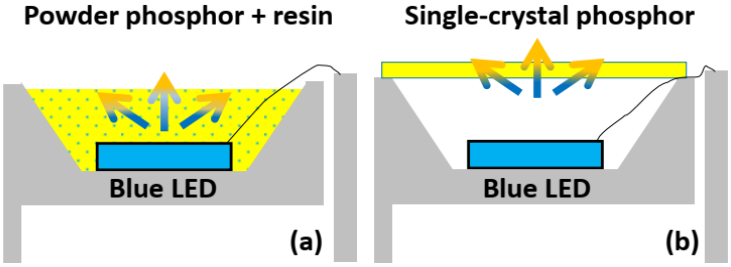

Fig. 1.8. Comparison schematic of WLEDs with VCC (Volume-Casting-Conversion)(a) and PCLC (b) designs [64].

has focused attention on phosphor films that can be produced using different techniques such as sputtering deposition [68], electrochemical synthesis [69], pulsed laser deposition (PLD) [70], sol-gel [71], metal-organic chemical vapor deposition (MOCVD) [72] and liquid phase epitaxy (LPE) as well [73, 74]. Among the presented methods, the LPE technique is a versatile method for the production of SCFs for applications in optoelectronics with thicknesses in the range of several micrometers up to 200 micrometers with excellent material quality and reproducibility [75].

One of the first works in this area was from Kundaliya et al. [9], who proposed phosphor converter based on the YAG:Ce and LuAG:Ce garnet phosphor film epitaxially grown onto a YAG substrate, to induce yellow and green emission, respectively. Recently, with the participation of the Author of this dissertation it was shown the possibility of the development of $Tb_3Al_5O_{12}$:Ce (TbAG:Ce) single-crystalline film converters for wLEDs using LPE technique [76] (Fig.1.9). It is especially important to note that, according to Al_2O_3-Tb_2O_3 phase diagram, the $Tb_3Al_5O_{12}$ melts incongruently and it is difficult to grow a high-quality and large-size bulk TbAG:Ce crystal by Czochralski (Cz) or other melt-grown techniques which is a barrier for its practical applications [77]. However, the single crystalline $Tb_3Al_5O_{12}$ matrix can be fabricated in the pure garnet phase using low-temperature synthesis methods such as LPE growth [78].

The next generation of film converters is the development of a composite color converter (CCC), based on the Ce^{3+} doped film/crystal epitaxial structures [79]. Development of CCCs suggests a few more additional tunable parameters, originating from the single crystal substrate: (i) Ce^{3+} doping concentration in the substrate; (ii) thickness of the substrate. Finally, the combination of the emission coming from the Ce^{3+} doped substrate and film constituents of the color converter allows the obtaining of a wide spectrum of WLEDs similar to the spectrum of natural white light, with enhanced luminous efficacy in comparison with standard photoconverters.

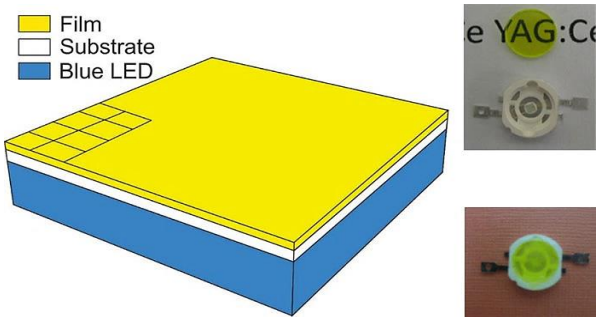

Fig.1.9. Schematic representation of a white LED, with a film photoconverter, pc-WLED prototype (right side of figure).

Conclusion to Chapter 1

This chapter explores the peculiarities of the garnet crystal structure and the luminescence properties of Ce^{3+} ions in garnet phosphors. The crystal structure allows for tunability of the

luminescence behaviors of Ce^{3+} doped garnets by varying the cations in the structure. The incorporation of Ce^{3+} ions in garnet phosphors leads to unique luminescent properties, particularly in the yellow spectral region. The Ce^{3+} rare earth ion has a simple electron configuration, and radiative transitions occur from the lowest excited energy level of the 5d configuration to the ground state. The *centroid shift* (determined by the so-called nephelauxetic effect) and the *crystal field splitting* plays crucial roles in determining the emission properties of Ce^{3+} in garnets. The centroid shift refers to the reduction in the average energy of all the 5d levels within an activator ion. This decrease in energy arises due to a decrease in inter-electron repulsion. The determination of the centroid shift involves analyzing the positions of all 5d energy levels, and it is defined as the average energy of these levels, taking into account their degeneracy. This average energy value is commonly referred to as the *barycenter*. The crystal field splitting is influenced by the covalency of the bonds and the coordination environment, resulting in the splitting of 5d levels into multiple components. The change of the centroid shift and crystal field splitting contribute to the overall redshift or blue shift of the Ce^{3+} luminescence band. The strength of these effects is influenced by the chemical nature of the host lattice and the positions of the valence band and conduction band edges. By adjusting the composition and structure of the host lattice, both the excitation and emission energies of Ce^{3+} in garnets can be tailored.

Increasing the power of white diodes poses limitations in the optical, structural, mechanical, and thermal aspects of converters. Most pc-WLEDs are made using the VCC design, combining a blue LED and powdered PC within organic resins. However, the low heat resistance of epoxy resin and silicone can lead to color shifts and reduced lifespan. To address these issues, the PCLC approach separates the phosphor from the LED chip, creating a free-standing converter. PCLC employs materials like ceramics, glasses, single crystals, or films as phosphors to manufacture high-power WLEDs under near UV and blue LED excitation

The LPE growth stands out as a versatile method for producing SCF converters with thicknesses ranging from several micrometers to even 200 micrometers. Notably, the LPE technique has shown promise in the development of TbAG:Ce and GdAG:Ce based garnet converters in SCF form for WLEDs. The incongruent melting characteristics of TbAG and GdAG present challenges in the context of bulk crystal growth, but LPE method enables the fabrication of pure garnet-phase $Tb_3Al_5O_{12}$ and $Gd_3Al_5O_{12}$:Ce matrices at low temperatures [78, 80]. This breakthrough opens up new possibilities for practical applications of TbAG:Ce and GdAG:Ce based converters. The future of film converters lies in the development of composite color converters (CCCs), which combine Ce^{3+} doped film/crystal epitaxial structures. CCCs offer additional tunable parameters, such as the Ce^{3+} doping concentration in film and crystal as well as the thickness of the single crystal substrate and films, resulting in a wide spectrum of WLEDs that closely resemble natural white light.

Chapter 2. Features of the growth of luminescent materials based on the single crystalline films of garnets using the LPE method

2.1 LPE growth of garnet single crystalline films for WLED

The development of garnet phosphors in thin SCF form is much preferable to powders, glasses, or ceramics, due to their high crystallinity, internal quantum efficiency (QE), and excellent thermal stability up to at least 300 °C for YAG:Ce and LuAG:Ce [81]. The trend for device minimization has focused attention on phosphor films that can be produced using different techniques such as sputtering deposition [68], electrochemical synthesis [69], pulsed laser deposition (PLD) [72], sol-gel [82], metal-organic chemical vapor deposition (MOCVD) [83] and liquid phase epitaxy (LPE) as well [84, 85]. Nowadays only a few works in the literature consider the use of epitaxially grown film phosphors for pc-WLED which opens up ample opportunities for innovative solutions in this field. There appears to be little, if any, work in the literature considering the use of epitaxially grown SCF phosphors for pc-WLED. The first work in this field was performed by Kundaliya et al. [9], who proposed WLEDs produced by depositing a YAG:Ce garnet film phosphor onto an undoped YAG substrate. Zorenko et al. [86] reported the successful quasi-homoepitaxial growth SCFs of TbAG:Ce and GdAG based garnets onto YAG substrates [78, 80]. Furthermore, LPE grown TbAG:Ce SCFs were also studied by us with the purpose of WLED application [79].

For the first time, the method of SCF growth by the LPE method was used by Levinstein and his colleagues [75, 87]. Subsequently, the LPE method was improved and developed at the end of the 70s of the last century to obtain the SCFs of ferromagnetic materials with cylindrical magnetic domains, as well as the SCFs of other magneto-optical materials [88, 89].

Epitaxy, like all forms of crystal growth, is a well-controlled phase transition that results in a single-crystal solid. Therefore, the formation of an epitaxially grown precipitate is the creation of a new phase [75, 90]. This is achieved by the relationship of nucleation and growth between the two crystalline phases, which allows the crystalline "f" phase (film) to grow depending on the structure onto the crystalline "**s**" phase (substrate) of a given structure. The essence of this method consists of the horizontal immersion of the substrate in the super-cooled melt solution (MS), followed by its rotation. The LPE process is isothermal. When the substrate is immersed into the MS, SCF growth occurs on the substrate surface due to the supersaturation of the solution concerning the garnet phase at a given temperature. At the initial stage of substrate immersion in the melt solution, there is a period of non-stationary growth during which a diffusion transition layer (TL) is formed, followed by steady-state growth of the SCF at a constant rate after the formation of a diffusion TL [91].

The SCF growth occurs gradually through the diffusion of garnet molecules towards the crystal growth front, followed by a surface reaction. However, considering only the diffusion of garnet

molecules from the MS to the SCF is not entirely accurate because the garnet molecules are in a dissociated state in the solution. According to the kinetics growth model in the horizontal system [91], mass transfer occurs through the diffusion of individual components of the solution. The garnet molecule M_8O_{12}, dissociates into four parts, with M_2O_3 being the most probable product. For a simple garnet with an equilibrium constant $L_1=\{Y\}_3\{Al\}_5$, which is the product of the molar concentrations of the cation components, the dissolution process can be represented as $\mathbf{3Y_2O_3 + 5Al_2O_3 \leftrightarrow 2Y_3Al_5O_{12}}$.

The process of SCF formation can be described by a sequence of elementary processes, as proposed in previous studies [92]:

1. Transport of MS components to the diffusion layer boundary.
2. Independent diffusion of the components occurs through the diffusion layer.
3. Ordering of the components may also occur near the crystal growth front.
4. The desolvation of solvent molecules and surface diffusion of the crystal components toward the attachment sites.
5. Flux molecule diffusion through the diffusion layer into the solution.

2.2 The selection of the melt solution

The melt compositions for growing of $A_3Al_5O_{12}$:Ce (A =Y, Lu, Tb) garnets onto YAG substrates included PbO and B_2O_3 as flux components, the Y_2O_3, Lu_2O_3, Tb_4O_7, Al_2O_3 oxides as garnet film-forming components, and dioxide CeO_2 as rare-earth ion dopant.

The main requirements for MS are as follows:

1. Achieving significant supercooling without the risk of spontaneous crystallization.
2. Low viscosity, allowing easy removal of MS droplets from the surface of SCF even at low (200-300 rpm) rotation speed.
3. The saturation temperature (T_s) of MS should be in the range of <1000-1050 °C
4. MS should be characterized by weak dependence of SCF properties on growth conditions.
5. The MS flux components should have very low segregation coefficients in SCF of garnets.

The above-mentioned requirements are fulfilled by optimizing the main four ratios, so-called *Blank-Nielsen coefficients* R_1, R_2, R_3, R_4 (Eqs.2.1). These coefficients should be maintained during the preparation of the MS for the production of SCF with chosen content, and they should correspond to the following molar ratios [93]:

$$R_1 = \frac{P_{flux_{PbO}}}{P_{flux_{B2O3}}};\quad R_2 = \frac{\sum P_{garnet}}{\sum P_{garnet}+\sum P_{flux}};\ R_3 = \frac{\sum P_{garnet(dod)}}{\sum P_{garnet(oct+tet)}};\ R_4 = \frac{\sum P_{dopant}}{\sum P_{garnet}} \qquad (2.1),$$

where P is the mole weights of the garnet and activator host components, which are located in the dodecahedral (dod), octahedral (oct), and tetrahedral (tet) positions in the garnet lattice, as well as the PbO and B_2O_3 flux components.

The solubility of the oxides and the kinetic properties of the solution are both determined mainly by the coefficient R_1 = 11–12. The value R_2 = 0.02-0.035 identifies the garnet phase as the primary phase during the film crystallization. The choice of molar ratios R_3 and R_4 is directly related to optimizing the structural quality of the SCFs. The optimal values of the coefficients R_3 and R_4 are determined experimentally for SCFs with selected compositions.

Generally, the choice of the value of R_2 coefficient is associated with the action of two factors. The first factor is the relationship between the segregation coefficients of the activator ions (in our case the Ce^{3+}) and the Pb^{2+} ions as a component of the flux. The second factor is determined by the requirement that the value of R_2 should correspond to such MS, for which the growth temperature (T_{gr}) range should not exceed 950-1000 °C to prevent significant evaporation of PbO. When the growth temperature (T_{gr}) and the value of R_2 decrease, the values of segregation coefficients of Ce dopant increase and vice versa. However, in the case using of PbO based flux for MS preparation, the incorporation of lead (Pb^{2+}) ions into the composition of the phosphor also increases. These Pb^{2+} ions act as efficient quenchers of Ce^{3+} luminescence and other dopants in these phosphors [94]. Since the action of these factors is opposite, the choice of the optimal value of the coefficient R_2 requires a compromise approach. Regarding the improvement of film luminescence efficiency, R_3 and R_4 coefficients are selected in the ranges of 0.02-0.035 and 0.01-0.15, respectively [93]. The crystalline structure and morphology of epitaxial films can be controlled by modifying the growth conditions (temperature of growth, super-cooling rate of melt-solution, rotational speed), and film/substrate misfit.

2.3 Requirement for single crystal substrate

The term *epitaxy* describes the ordered crystalline growth of a film on a single-crystalline substrate. Therefore, the substrate can be considered as a seed, which crystalline structure and orientation are replicated in the grown film. In the present work, the two types of epitaxial growth are presented.

1. **Homoepitaxy.** The SCF and substrate material grown possess the same content, i.e., the film is grown on a substrate of the same material, for example, the YAG:Ce SCF is grown onto a YAG SC substrate. The presence of dopants here in the concentration below 1 at. %. is not critical since their content is low to change significantly the lattice constant of film/substrate materials.

2. **Quasi-homoepitaxy.** The materials of the same crystallographic structure are grown in the LPE process, in which only one component is replaced by another; or to achieve better lattice matching between the two materials, one component of the first material can be replaced by two components. However, such substitutions of the first material do not lead to a fundamental change in its physical properties since it belongs to the same crystallographic and chemical group as the second material, for example, the LuAG:Ce and TbAG:Ce SCFs grown on YAG substrates.

Thus, the main limitations for *Quasi-homoepitaxy* growth of garnets are associated with the selection of a single-crystal substrate on which the film will be grown. For this technique, the permissible lattice constant misfit between the film and the substrate is considered to be in the range $\Delta\mathbf{m} = (a_{SCF} - a_{sub})/a_{sub} \times 100 = \pm 1.5\%$ [85].

The YAG is a relatively cheap substrate commonly used in LPE for the growth of high-quality SCFs. YAG lattice parameter closely matches that of all garnet family members, starting from LuAG up to GdAG, enabling defect-free film growth with a high degree of crystallographic orientation. For the LPE growth of film and composite color converters, the YAG and YAG:Ce substrates are required, respectively. For substrate preparation, the YAG and YAG:Ce bulk crystals were grown in the Crytur Ltd, Turnov, Czech Republic, and Institute of Materials National Academy of Science in Kharkiv, Ukraine using the Czochralski growth method, and further cut on wafers with sizes up to 5×5 mm and 0.5-1 mm in thickness. To ensure stable film growth, high smoothness of substrate surface is required, which is performed by the following mechanical polishing and final chemical-mechanical polishing of wafers with a SiO_2 slurry (typically 50-70-nm colloidal silica solution containing NaOH with pH 8.5-9.5) to achieve surface roughness below 0.5 nm RMS (root mean square).

2.4 Crystallization process of single crystalline films using LPE technique

The LPE growth procedure of garnet SCFs is as follows. The prepared substrate is fixed in the holder, which moves vertically and rotates horizontally (Fig. 2.1).

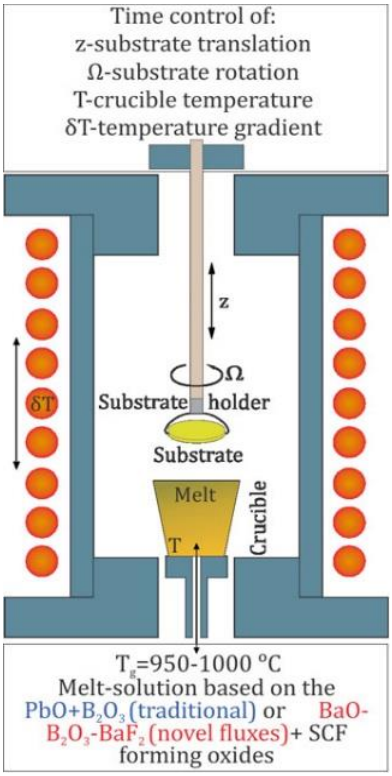

Fig.2.1. Scheme of the setup for SCF growth of garnet compounds by the LPE method.

The substrate is immersed in a melt-solution heated in a Pt crucible, which consists of flux and crystal-forming components taken in the appropriate ratio to ensure SCF growth. MS is heated at a rate of 150°C/h to the homogenization temperature, which exceeds the corresponding saturation temperature of MS by 100-120°C. The homogenization of MS is achieved by stirring with a speed of 80-100 rpm for 2 hours. To enhance the conditions of MS homogenization, a specific temperature gradient was established in the furnace, with the lower zone temperature being 10-20°C lower and the upper zone temperature being 20-30°C higher than the temperature of the middle zone.

Further, the temperature of MS is slowly reduced to the growth temperature T_g. Upon reaching this temperature, the holder with the mounted substrate is immersed in MS and rotated at a speed of 80-120 rpm during the required time. Growth time determines the thickness of the resulting film. After the end of growth, the holder is pulled out of the MS, kept for 3-5 minutes, and then quickly rotated (500-800 rpm) to remove MS residues. The holder with the SCF grown on both sides of the substrate is taken out of the furnace and washed from the MS residues in a hot solution of acetic or nitric acids.

The crystallization process is shown in the diagram (Fig.2.2)

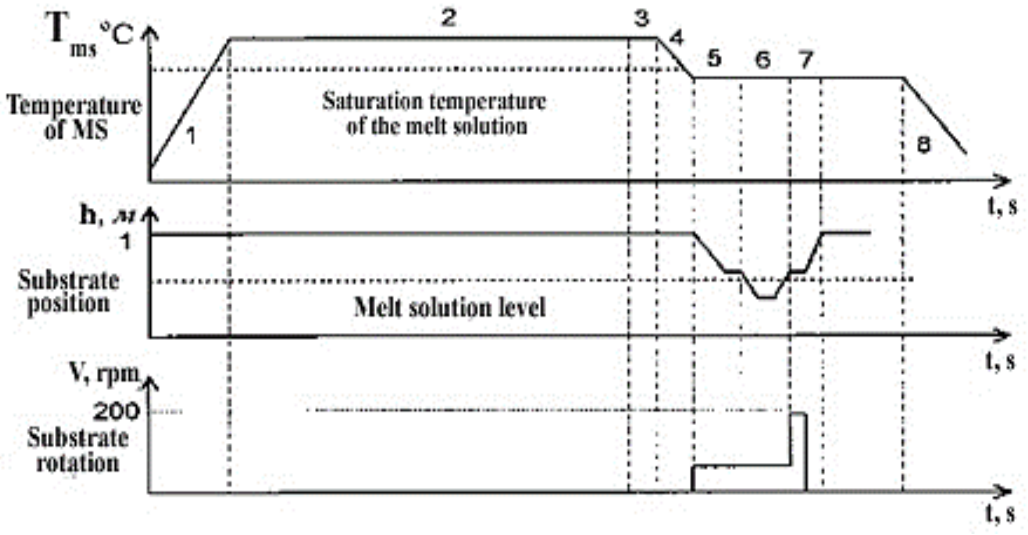

Fig. 2.2. Time diagram of SCF growing by the LPE method.

1. Heating
2. Homogenization at T~T_s+100°C.
3. Mixing with a platinum stirrer.
4. Lowering the temperature to T=T_{gr}.
5. Lowering the substrate to the surface of the melt and holding it above the surface (~0.5 hours).
6. Submerging the substrate into the melt, growth of single crystals, and removing the substrate from the melt.
7. Rotating the substrate above the melt, removing the single crystals from the furnace .
8. Cooling down the melt.

2.5 Determination of the thickness of single crystalline films

The SCF thickness was determined using the *weight method*, since the refractive index of the substrate and the film is close in both homoepitaxial and heteroepitaxial growth modes of garnet compounds, making it impossible to use the interference or refraction methods for thickness measurement. To do this, the substrate was weighed before and after the growth cycle of the single crystal. The thickness of the obtained single crystal was determined using the formula:

$$h_f = m - m_s \,/\, 2S\rho \qquad (2.2),$$

where $\boldsymbol{m}$ is the mass of the substrate with the grown single crystalline film in (g), $\boldsymbol{m_s}$ sub is the mass of the substrate in (g), **S** is the area of the substrate in (cm^2), and **ρ** is the density of the film in (g/cm^3) (ρ=4.55 g/cm^3 for YAG; 6.67 g/cm^3 for LuAG; ρ=6.24 g/cm^3 for TbAG).

2.6 LPE growth of single crystalline film and composite converters

The SCFs of LuAG:Ce, TbAG:Ce and $Tb_{1.5}Gd_{1.5}$AG:Ce garnets were grown at the Institute of Physics Kazimierz Wielki University of Bydgoszcz by LPE method onto undoped Czochralski grown (Cz) $Y_3Al_5O_{12}$ (YAG) substrates of (110) crystallographic orientations from Crytur Ltd, Turnov, Czech Republic. The substrates were prepared from hexagon-like plates of 20*0.5 mm size (Fig.2.3 a).

The LPE growth of composite color converters was performed onto Czochralski grown (110) oriented YAG:Ce SC substrates, specially prepared by the chemical-mechanical polishing in the Institute for Single Crystals, Kharkiv, Ukraine. The typical size of substrates used in the following research was 0.5x0.5mm with thicknesses h=0.5 and 1 mm. There were four different sets of YAG:Ce SC substrates with Ce concentration of 0.1; 0.15; 0.25; 0.5 at. %.

2.6.1 LPE growth of LuAG:Ce, TbAG:Ce and TbGdAG:Ce SCFs onto YAG substrates

- **LuAG:Ce SCF/YAG SC substrate**

The set of LuAG:Ce SCFs with different thicknesses was grown by the LPE method onto YAG substrates (Fig.2.3b). For melt preparation, the starting PbO, B_2O_3, Lu_2O_3, CeO_2, Al_2O_3 raw oxides of 4N purity were used. The film growth was performed from the supercooled MS based on PbO-B_2O_3 (12:1 mole/ mole) flux agents and garnet components, placed into Pt crucible. The content of garnet components in the melt solutions was in the 2.5–3.0 mole % range. The Lu_2O_3/Al_2O_3 oxides content in the MS was chosen with a stoichiometric ratio of 3/5. Due to very low segregation coefficients of Ce^{3+} ions in LuAG the concentration of CeO_2 activating oxides in the MS was equal to 10 mole % per total moll quantity of solution. Substrate rotation rotating speed in the melt was 60–160 rpm. In all growth cycles, the growth temperature T_g was in the 950-975 ºC range and the growth rate was in the f_s= 0.2-0.5 μm/min range.

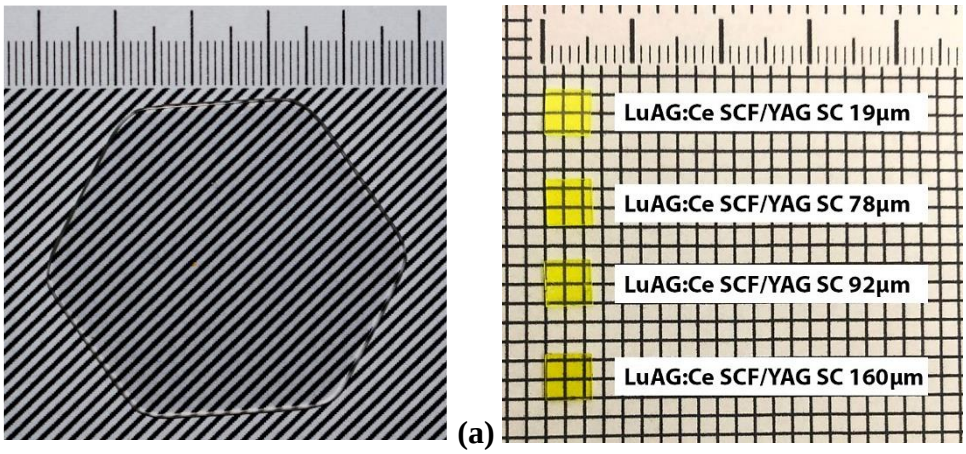

Fig.2.3. Images of undoped YAG substrate, prepared from the Cz grown crystal (a) and set of LuAG:Ce SCFs with different thicknesses, grown by the LPE method onto YAG substrates.

- **TbAG:Ce SCF/YAG SC substrate**

The TbAG:Ce SCFs growth was performed from the supercooled melt solution based on PbO-B_2O_3 (12:1 mole/ mole) flux and Tb_4O_7, CeO_2, Al_2O_3 garnet-forming components of 4N purity. In all crystallization cycles, the growth temperature T_g was in the 950-1025ºC range and the growth rate was in the f_s=0.35-1.6 μm/min range. The set of TbAG:Ce SCFs with Ce concentrations of about 0.6 at.% and different thicknesses were grown by the LPE method onto YAG substrates (Fig.2.4).

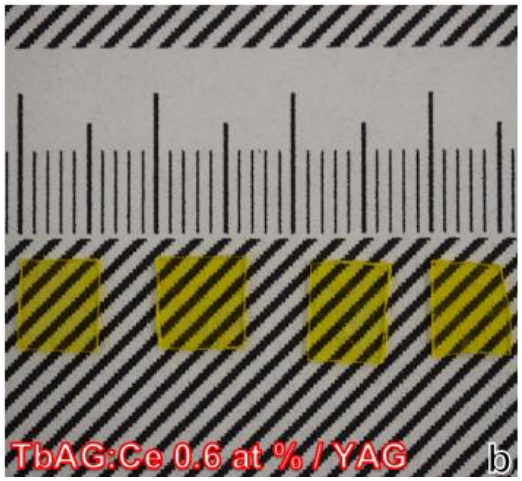

Fig.2.4. Images of TbAG:Ce SCFs with different thicknesses, LPE grown onto YAG substrates.

- **$Tb_{1.5}Gd_{1.5}$AG:Ce SCF/YAG SC substrate**

The SCFs with nominal composition $Tb_{1.5}Gd_{1.5}Al_5O_{12}$:Ce were grown using the Pt crucible from the supercooled MS based on PbO-B_2O_3 (12:1 mole/ mole) flux and 4N purity garnet-forming oxides: Tb_4O_7, Gd_2O_3, Al_2O_3, and CeO_2. The growth process of the TbGdAG-based films by LPE and the choice of mole ratios are described in detail in Ref. [92, 93].

The segregation coefficients for Tb and Gd ions are also found to be 0.85-0.9; and 0.95-1.1 respectively. Such a high segregation coefficient is explained by the close ionic radii values of Tb^{3+}

(1.04 Å) and Gd^{3+}(1.05 Å) ions) in dodecahedral positions of the garnet matrix [94]. Thus, the real SCF composition may differ from the nominal one within 5%. In the experimental part of the paper, the nominal composition of the films is given throughout. During the film growth process, the substrate horizontally attached to the Pt holder was rotating at 60–80 rpm in the forming melt with growth temperature T_g in the 950-1025 ºC range. Under the described conditions, the growth rate was in the f_s= 0.35-1.6 μm/min range.

Fig.2.5 displays the photographs of as grown $Tb_{1.5}Gd_{1.5}$AG:Ce SCF/YAG SC with different film thicknesses in the 43-85 μm range. It can be seen that the $Tb_{1.5}Gd_{1.5}$AG:Ce SCFs are yellow and transparent, which preliminary indicates the good quality of the samples since the crystallization of a polycrystalline film is often accompanied by a matte surface.

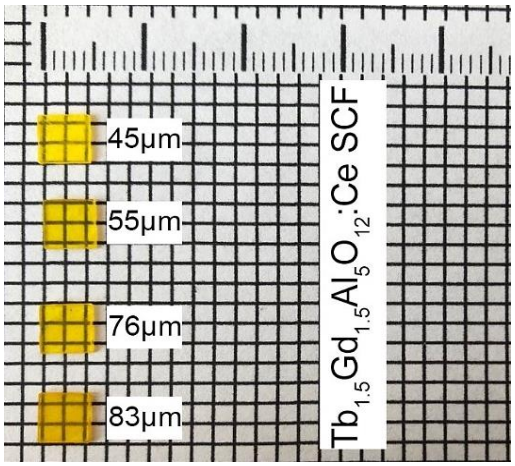

Fig.2.5. Images $Tb_{1.5}Gd_{1.5}$AG:Ce SCFs with different thicknesses, LPE grown onto YAG substrates.

2.6.2 LPE growth of composite film-crystals converters onto YAG:Ce substrates

- **LuAG:Ce SCFs/YAG:Ce SC substrates**

Fig. 2.6 presents the set of LuAG:Ce SCF/YAG:Ce SC substrate composite color converters consisting of the LuAG:Ce SCFs (h=11-30 μm, Ce=0.25-0.3 at.%), LPE grown onto YAG:Ce SC substrates (h=0.5; Ce= 0.15 at.%). For melt preparation, the PbO, B_2O_3, Lu_2O_3, CeO_2, Al_2O_3 raw oxides of 4N purity were used. The SCF growth was performed in the Pt crucible from the supercooled melt solution based on PbO-B_2O_3 (12:1 mole/ mole) flux agents and garnet components. The content of garnet-forming oxides in the MS was in the 2.5–3.0 mole % range. The ratio of Lu_2O_3/Al_2O_3 oxides content in the MS was chosen with a stoichiometric value of 3/5. Due to very low segregation coefficients of Ce^{3+} ions in LuAG SCF, the concentration of CeO_2 activating oxide in the MS was equal to 10 mole % per total moll quantity of solution. The substrate rotating speed in the melt was 100 rpm.

In all growth cycles, the growth temperature T_g was in the 960-985 ºC range and the growth rate was in the f_s= 0.2-0.8 μm/min range.

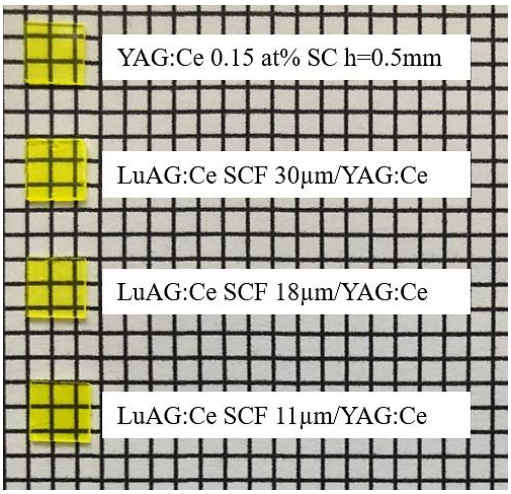

Fig. 2.6. Photo of LPE grown LuAG:Ce SCF/YAG:Ce SC substrate epitaxial structures with different SCF thickness.

- **TbAG:Ce SCFs/YAG:Ce SC substrates**

Fig. 2.7 presents the set of TbAG:Ce SCF/YAG:Ce SC substrate composite color converters consisting of the TbAG:Ce SCFs (h=30-128 µm, Ce=0.25-0.3 at.%), LPE grown onto YAG:Ce SC substrates (h=0.5; 1mm, Ce= 0.1 and 0.5 at.%). The TbAG:Ce SCF/ YAG:Ce SC substrate epitaxial structures were grown by the LPE method from the supercooled melt solution based on $PbO\text{-}B_2O_3$ (12:1 mole/ mole) flux and Tb_4O_7, CeO_2, Al_2O_3, garnet components of 4N purity. In all cycles of crystallization, the growth temperature T_g was in the 950-1025 ºC range and the growth rate was in the f_s= 0.35-1.6 µm/min range. Depending on the growth temperature in the mentioned range, the Ce content in SCF samples varied from 0.3 to 0.25 at. %.

The CCCs colors change from light yellow to dark yellow–orange, which is caused by the variance of transmittance property in the visible ranges due to the variations of film/substrate thickness and Ce^{3+} concentration.

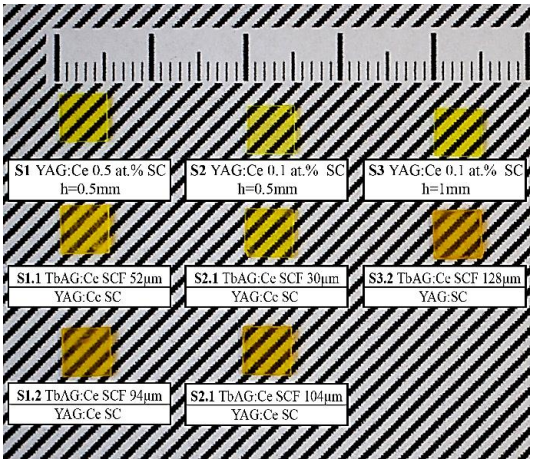

Fig. 2.7. Photo of LPE grown TbAG:Ce SCF/YAG:Ce SC substrate epitaxial structures with different SCF thickness.

- **$Tb_{1.5}Gd_{1.5}$AG:Ce SCF/YAG:Ce SC substrates**

Fig. 2.8 presents the set of $Tb_{1.5}Gd_{1.5}$AG:Ce SCF/YAG:Ce SC substrate composite color converters consisting of the $Tb_{1.5}Gd_{1.5}$AG:Ce SCF (h=12-48 μm, Ce=0.1-0.15 at.%), LPE grown onto YAG:Ce SC substrates (h=0.5; 1mm, Ce= 0.1; 0.15 and 0.5 at.%). The SCFs growth was performed in the Pt crucible from the supercooled MS based on $PbO-B_2O_3$ (12:1 mole/ mole) flux and 4N purity garnet-forming oxides: Tb_4O_7, Gd_2O_3, Al_2O_3 and CeO_2. Throughout the film growth process, the substrate horizontally attached to the Pt holder was rotating at 60–80 rpm in the forming melt. The SCF growth temperature T_g was in the 950-1025 ºC range, and under the described conditions, the growth rate was in the f_s= 0.35-1.6 μm/min range.

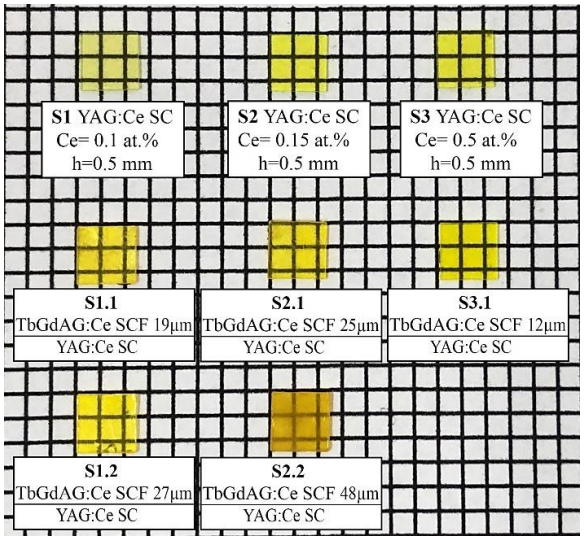

Fig.2.8. Photo of composite color converters with various $Tb_{1.5}Gd_{1.5}$AG:Ce SCF thickness, LPE grown onto substrate with different Ce contents: S1 (0.1 at. %); S2 (0.15 at.%); S3 (0.5 at.%).

Conclusion to Chapter 2

This chapter focuses on the details of the LPE growth technology of garnet-based phosphors in the SCF form for potential application in pc-WLEDs. SCFs of garnet compounds offer significant advantages over ceramics or powders counterparts in terms of high crystallinity, internal quantum efficiency, and thermal stability. The LPE technique involves a well-controlled phase transition, resulting in the growth of high-quality SCFs of a large variety of garnets.

The SCF growth process using the LPE method is described, highlighting the diffusion of garnet-forming cations from the MS and surface reactions. The selection of the MS content is crucial for achieving significant supercooling, low viscosity, and weak dependence of SCF properties on growth conditions.

This chapter also emphasizes the importance of choosing an appropriate single-crystal substrate for epitaxial growth. YAG SC substrates are commonly used due to their close lattice matching with

the row of lanthanides garnet family and their ability to support defect-free film growth with high crystallographic perfection. The details of LPE growth cycle are presented, including the immersion of the substrate in the MS, rotation, and controlled temperature reduction.

The following SCF samples and composite structures, grown using the LPE technique were studied and tested in this work:

Films: LuAG:Ce, TbAG:Ce and TbGdAG:Ce SCFs, grown onto undoped YAG substrates

Composites: LuAG:Ce, TbAG:Ce and TbGdAG:Ce SCFs grown onto YAG:Ce substrates.

The chapter concludes with a description of the critical aspects of the LPE growth process of film and composite converters, highlighting the potential of such materials for pc-WLED applications.

Chapter 3. Experimental techniques

In an effort to better understand and develop SCF and composite color converters, a wide range of experimental techniques were used in this study. These techniques have played a crucial role in characterizing the materials and unraveling their structural, mechanical and optical properties. In this chapter, we will discuss each experimental technique in detail, highlighting their principles, methodologies, and specific applications within this research.

3.1 X-ray diffraction analysis

In materials science, X-ray diffraction analysis (XRD) is a method used to determine the crystallographic structure of a substance. In order to perform XRD, a material is first irradiated by an incident X-ray beam, and then the intensities and scattering angles of the X-rays that escape the material are measured. XRD analysis is the identification of materials based on their diffraction pattern. XRD provides information on phase identification as well as how internal stresses and defects affect the actual structure and how it differs from the ideal one. Diffraction occurs when each object in a periodic array scatters radiation coherently, producing concerted constructive interference at specific angles**.**

The strong peak of intensity that is produced by the coherent scattering of the atomic arrangement in a crystal is called the *Bragg diffraction peak.* Bragg derived an expression for the conditions required for constructive diffraction to occur. Let us consider a system of parallel planes A, B, C in Fig. 3.1 Diffraction of X-rays by a crystal lattice [95].

In the first plane of atoms, rays 1 and 1a hit the atoms K and P and then scattered in all directions. Only in directions 1' and 1a' are the scattered beams in phase with one another, leading to

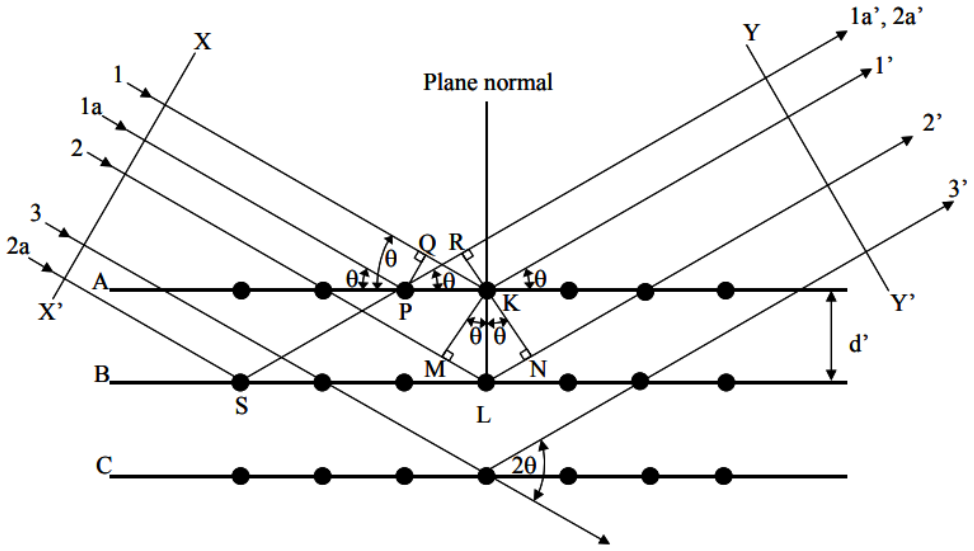

Fig. 3.1. Diffraction of X-rays by a crystal lattice, where *d* is the spacing between diffracting planes, θ - is the incident angle, *n* is an integer, and λ is the beam wavelength [95].

constructive interference. As a result of the wavefronts XX' and YY' having identical path lengths, constructive interference is observed. Thus, the zero path lengths difference can be written as

$$QK - PR = PK\cos\theta - PK\cos\theta = 0 \quad (3.1).$$

The intensity of the diffracted beam will increase because any rays that are scattered by atoms in the plane that are parallel to 1' will also be in phase and add their contributions to the beam. Now let us consider the condition required for rays scattered by atoms in various planes to interfere constructively. For rays 1 and 2 which are scattered by atoms K and L the path difference of 1K1' and 2L2' can be expressed as:

$$ML + LN = d'\sin\theta + d'\sin\theta \quad (3.2).$$

Since there is no path difference between rays scattered by atoms S and L or P and K in this direction, this term also describes the path difference for reinforcing rays scattered from atoms S and P in the direction depicted in Fig. 3.1. Scattered rays 1' and 2' will be in phase only if the path difference is a whole number of wavelengths, which is commonly known as Bragg's Law and it forms the fundamental basis of X-ray diffraction theory

$$n\lambda = 2d'\sin\theta \quad (3.3).$$

When X-rays are diffracted through crystal lattices, a distinct correlation can be seen between the diffraction pattern and the inter-planar spacing of the material. From the above mentioned it is clear that if a beam of X-rays is directed at a crystal, then in the space around the crystal one can detect a regular interference pattern, which is relatively easy to register, for example, on an X-ray film or detector placed at a small (on the order of several centimeters) distance from the crystal. For a material that is not under any strain, the inter-planar spacing will result in a distinctive diffraction pattern. When a material is under strain, the crystal lattice undergoes elongations and contractions that change the distances between the {hkl} lattice planes. The diffraction pattern will shift as a result of this induced change in *d*.

The change in the inter-planar spacing can be precisely measured, allowing for the evaluation of the shift and the subsequent determination of the strain present in the material. The two most common

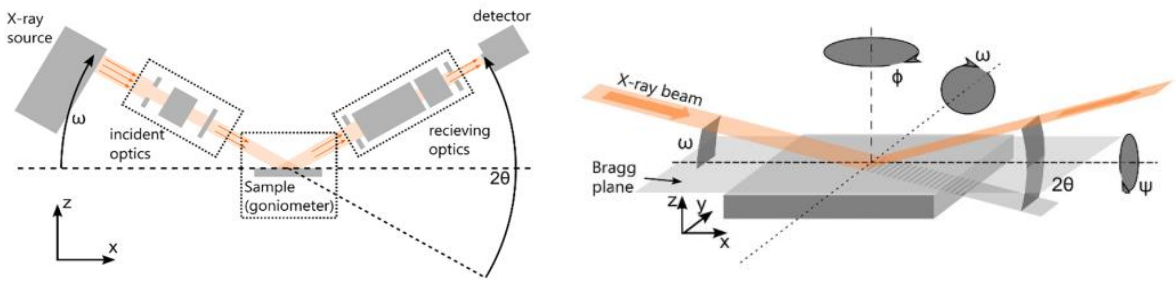

Fig.3.2 (a) - components of a diffractometer. (b) - schematic of the notation used for the angles and degrees of freedom in a typical diffractometer used for thin film measurements [96].

configurations for X-ray studies are single crystal and powder XRD. However, the X-ray spectrometer's parts are generally similar and consist of the X-ray source, the detector, the incident (or primary beam) optics, the receiving (or diffracted beam) optics, and the goniometer, as shown in Fig. 3.2a [95].

In XRD, the incident angle (ω) is the angle between the X-ray source and the sample, while the diffracted angle (2θ) is the angle between the incident beam and the detector. These two angles are coupled and move simultaneously during measurements. However, in thin film measurements, it is often necessary to decouple the scattering angle from the angle of incidence for tasks like rocking curve measurements or substrate alignment. In such cases, the incident angle (ω) is used to denote the angle of incidence.

Different types of scans can be performed in XRD:

1. A Rocking Curve involves plotting X-ray intensity against the incident angle (ω).
2. A Detector Scan plots X-ray intensity against the diffracted angle (2θ) without changing the incident angle (ω).
3. A Coupled Scan is a plot of scattered X-ray intensity against the diffracted angle (2θ), with the incident angle (ω) changing in a way linked to 2θ, typically described as ω=1/2*2θ + offset.

For the purpose of this research, XRD measurements were conducted at the Institute of Single Crystal NAN of Ukraine using the DRON 4 spectrometer with a $Cu_{K\alpha}$ X-ray source. The measurements were performed in the 2θ range with a step size of 0.02° to determine the crystalline phase, assess the structural quality, and calculate the misfit values between the SCF and the substrate.

3.2 Scanning Transmission Electron Microscopy

Scanning Transmission Electron Microscopy (STEM) is an advanced imaging technique that builds upon the principles of traditional Transmission Electron Microscopy (TEM). STEM allows for the detailed imaging and analysis of both the surface and internal structure of a sample. In a STEM, a focused electron beam is transmitted through a thin sample, and the electrons that pass through the sample are collected by a detector on the other side. This allows for the generation of high-resolution images that reveal the atomic structure and composition of the sample. One of the main advantages of STEM over traditional TEM is its ability to produce images with both high spatial resolution and high contrast. This is due in part to the use of a smaller electron probe size and the collection of electrons at different angles, which results in improved imaging capabilities [97].

The samples used in STEM must be extremely thin and carefully prepared to avoid damage from the electron beam. Despite these challenges, STEM remains an essential tool for researchers seeking to better understand the properties and behavior of materials at the atomic scale, and for developing new materials with unique properties and functions [98].

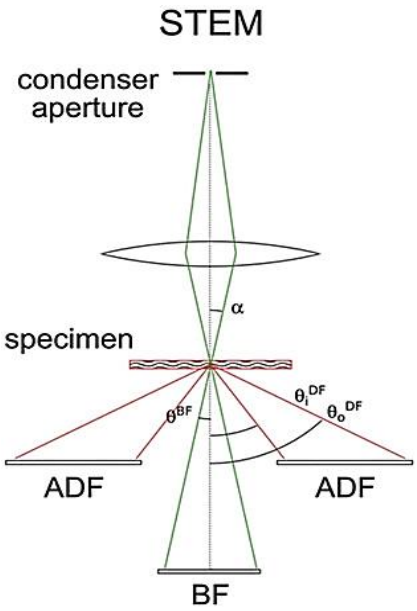

Fig. 3.3. Schematic representation STEM.

A typical STEM setup includes the following components (Fig. 3.3):

- An electron source that generates a beam of high-energy electrons.
- A series of lenses that focus and shape the electron beam.
- A sample holder that holds the thin sample is to be imaged.
- An electron detector that collects electrons that have passed through the sample.
- A computer system that processes and displays the resulting images.

The electron beam is focused onto the sample using magnetic lenses, and as the beam passes through the sample, some of the electrons are scattered or absorbed. The remaining electrons are collected by the detector on the other side of the sample, and their intensity and direction are recorded to generate an image. STEM can be performed in different modes, including *high-angle annular dark field* (**HA ADF**) and *annular bright field* (**A BF**) imaging, each of which provides unique information about the sample's structure and composition.

The high-resolution scanning transition electron microscopy (HR STEM) and composition analysis measurements of the specially prepared cross-section of the LuAG:Ce SCF/YAG SC and TbAG:Ce SCF/YAG SC epitaxial structures were performed at the Center for Nanoanalysis and Electron Microscopy in Erlangen, Germany. For imaging, electron diffraction and energy dispersive X-ray spectroscopy a double corrected Titan Themis³ 300 (FEI Company, Hillsboro, USA) operated at an acceleration voltage of 300 kV was utilized.

3.3 Acoustic microscopy

Acoustic microscopy is a non-destructive imaging technique that uses ultrasound waves to create images of the surface and internal structures of materials. The principle of acoustic microscopy

is based on the reflection and scattering of high-frequency sound waves at interfaces between materials of different acoustic impedance. This method is universal for non-destructive testing, and the scope is not only limited to the quality control during production of electronic and microelectronic devices but also spreads much more widely including the areas of photovoltaics, automotive, materials science, and biotechnology. It can be noted that acoustic microscopy is an excellent tool for studying semiconductor wafers, crystals, and multilayer devices such as flip chips, chip-on-board, chip-on-flex, etc.

An acoustic microscope consists of a transducer, which emits high-frequency sound waves, and a receiver, which detects the waves that are reflected or scattered by the sample. The transducer and receiver are typically mounted on a scanning stage which allows the sample to be scanned in two dimensions. The electrical signal (pulse mode) from the generator enters a piezoelectric transducer, which converts the electrical signal into acoustic waves. For frequencies below 100 MHz, lithium niobite ($LiNbO_3$), quartz ceramics, or crystals are used. If frequencies are above this limit, piezoelectric crystals such as zinc oxide (ZnO) are used. Next, the acoustic signal is sent through the sapphire (Al_2O_3) cylinder to the focusing lenses, after which the acoustic field is focused on the lens axis in a binding medium (see Fig.3.4).

The focal length of a transducer is shortened due to the higher speed of sound in most materials compared to water, which is commonly used as a coupling medium. This phenomenon is primarily caused by refraction, wherein sound waves are refracted as they pass through materials with different acoustic properties. To ensure the efficient transfer of acoustic waves, it is crucial to establish effective acoustic coupling between the transducer and the object being studied, which can be achieved by using

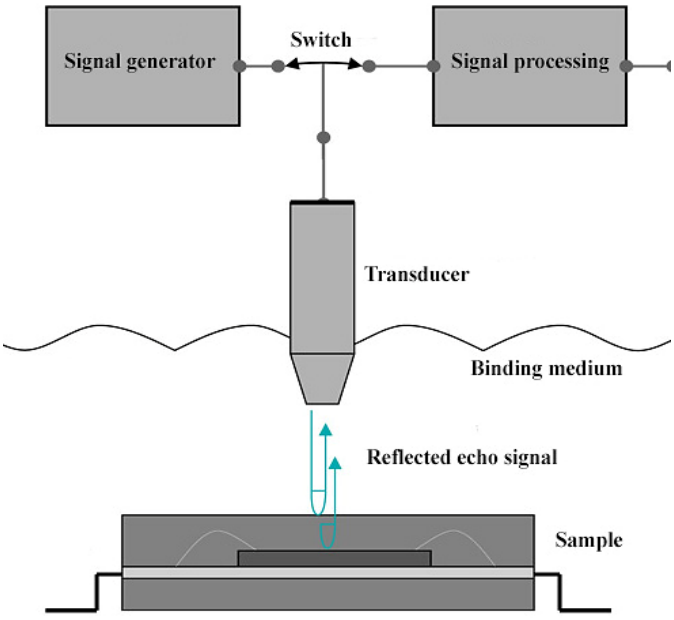

Fig.3.4 Scheme of operation of an acoustic microscope, showing the incident and reflected pulse.

a suitable coupling medium, such as water [99]. The Scanning Acoustic Microscope (SAM) utilizes an ultrasonic pulse, generated by the transducer, to investigate the sample and record the reflected echoes produced after interacting with the internal structure over a range of time delays. The magnitude of these time delays is determined by the acoustic properties of the material, including its density and attenuation, which are determined by the material's acoustic impedance.

The SAM and optical microscope share common parameters, including resolution, penetration depth, and contrast. In an acoustic microscope, the resolution (w) is determined by the ultrasonic frequency (f) utilized for imaging, similar to an optical microscope:

$$w = \frac{\lambda}{2NA}, \ \lambda = \frac{c}{f}, \tag{3.4}$$

where λ is the wavelength of the ultrasound wave in the liquid, NA is the numerical aperture, of the acoustic lens. NA = sinθ, where θ is the semi-angle of the lens aperture. Fig.3.5 illustrates schematically a focusing of an acoustic lens.

Optimal adjustment of the probe/sample-distance is advisable, aiming to position the focal length at the precise location of interest, such as the interface between film and substrate.

Maximal reflection from a plane surface perpendicular to the sound beam occurs when the reflection takes place precisely at the focal length, causing all incident waves to be reflected back toward the lens. The utilization of high frequencies enhances the capability to examine near-surface materials by enhancing both lateral and depth resolution. By employing a 50 MHz transducer and taking into account the longitudinal wave velocity of water (V_L = 1500 m/s), it is feasible to achieve a resolution of around 30 μm.

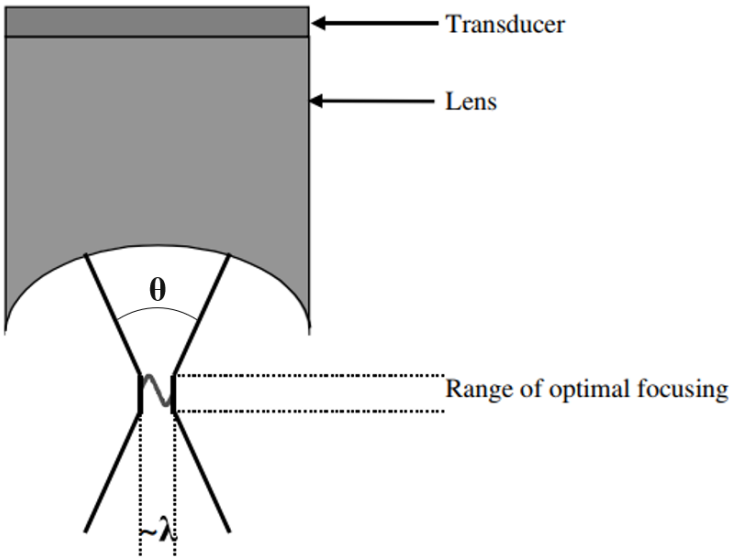

Fig.3.5. In the focusing schematic, the smallest achievable focal spot size is approximately equal to one wavelength [100].

In this research the V(z) curve method in conjunction with scanning acoustic microscopy was used to non-destructively evaluate the elastic properties of epitaxial structures. Fig. 3.6 presents a schematic diagram illustrating the propagation of surface acoustic waves (SAW) between the acoustic lens and the specimen via a coupling medium.

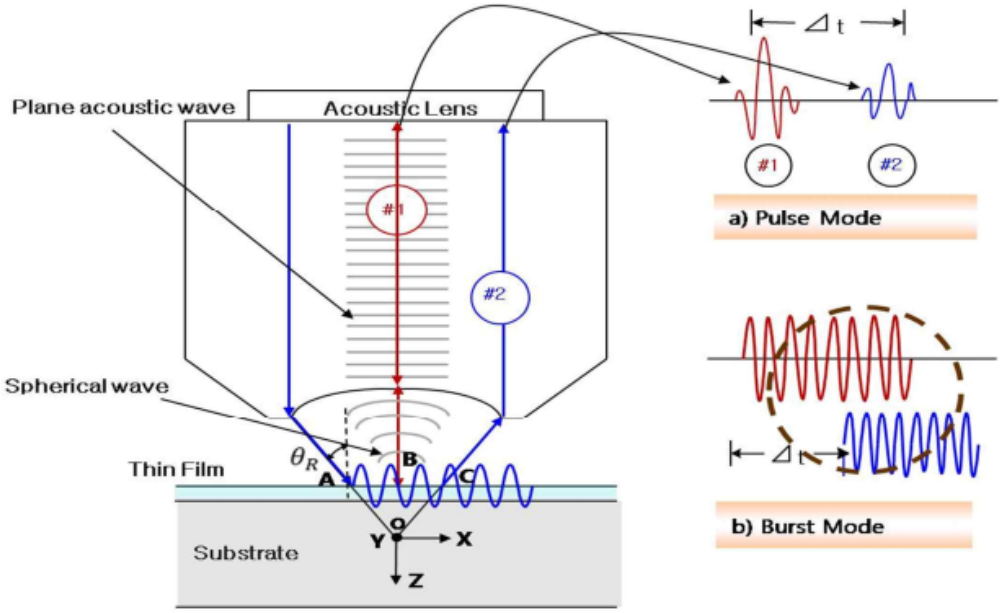

Fig. 3.6. Illustrates a schematic diagram that demonstrates the fundamental concept of the V(z) curve [100].

This diagram highlights the occurrence of different SAW types, with Rayleigh waves being the most common. Rayleigh waves arise at the interface between a solid and non-solid medium, originating from incident waves impinging at the Rayleigh angle θ_R. The generation of a surface acoustic wave at a liquid-solid interface is achievable when the half aperture angle of the acoustic lens exceeds the second critical angle associated with that particular surface.

Interference between the specularly reflected acoustic waves (path #1 in Fig. 3.6) and the surface acoustic waves (path #2) at the acoustic sensor leads to the generation of alternating maxima and minima in the acoustic output signal. The occurrence and spacing of these interference patterns depend on the distance between the acoustic lens and the specimen. The plot depicting the interference patterns and their variation concerning the distance between the acoustic lens and the specimen is commonly referred to as the V(z) curve (Fig.3. 7).

The velocity of the surface acoustic wave (SAW) can be determined by measuring the spacing Δz between consecutive minima in the interference pattern. This arises from considerations of the difference in path and phase change during the interference of two waves. As the specimen (depicted in Figure 3.6) is displaced from z=0 towards the acoustic lens by distance z, paths #1 and #2 undergo

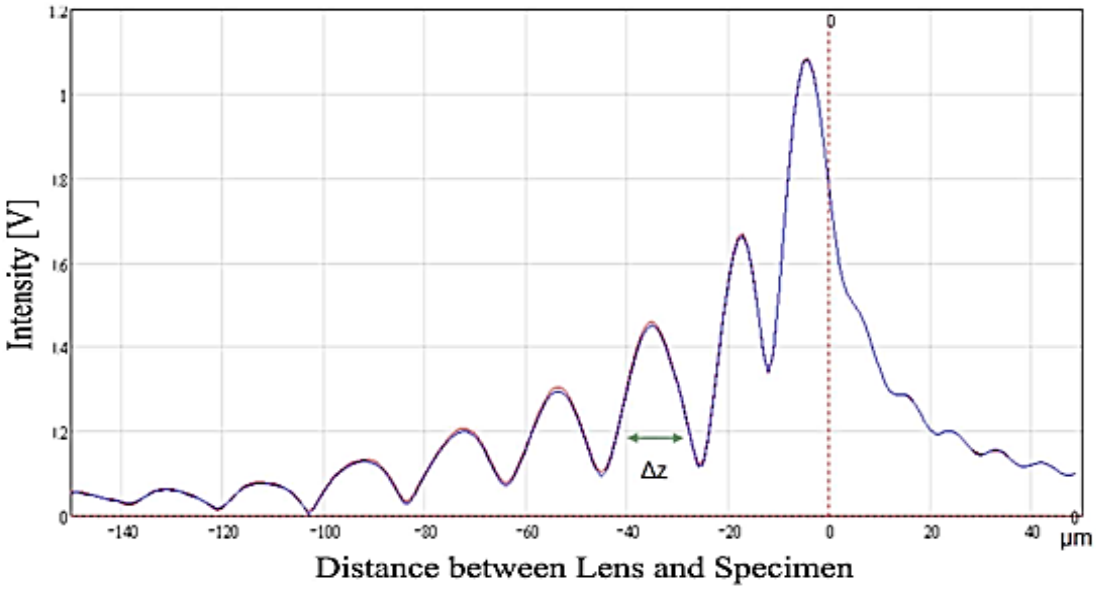

Fig.3.7. An illustrative example showcasing the V(z) curve [101].

distinct phase changes. When the specimen is positioned at a distance z from the focal plane of the lens, the phase changes $\delta_{\#1}$ and $\delta_{\#2}$ can be expressed as follows:

$$\delta_{\#1} = -2\overline{B0} \cdot k_w = -2zk_w$$
$$\delta_{\#2} = -2\overline{A0C} \cdot k_w + \overline{AC} \cdot k_r \quad (3.5).$$

The relative phase change between the two paths can be described as follows:

$$\Delta z = \delta_{\#2}(z) - \delta_{\#1}(z) = 2z\left[k_w\left(1 - \frac{1}{cos\,\theta_R}\right) + k_R\, tan\,\theta_R\right] \quad (3.6),$$

where $k_w$is wavenumber in the water, while k_R is the wavenumber of the surface wave.

Based on Equation (3.6) and applying Snell's law, the following expression can be obtained:

$$\Delta z = \frac{v_\omega}{2f(1-\cos\theta_R)} \quad (3.7),$$

where $v_\omega$represents the acoustic velocity in water, and f denotes the working frequency.

By once again applying Snell's law to determine the angle θ_R, Equation (3.7) can be reformulated to explicitly express the velocity V_R of the surface acoustic wave as a function of Δz.

$$V_R = \frac{v_w}{\sqrt{1-\left(1-\frac{v_\omega}{2f\Delta z}\right)^2}} \quad (3.8).$$

The spacing of the points in Figure 3.7, as described by Equation (5), allows for the calculation of the velocity of the surface acoustic wave (SAW). Indeed, the simple ray optics theory can provide a quantitative measurement of the phase velocity of a surface acoustic wave (SAW) from the V(z) curve, enabling the characterization of the acoustic properties of materials. Additionally, the shape of the curve, including any changes in slope or discontinuities, can indicate variations in the material's density or elastic constants. This information is valuable for characterizing the material's acoustic behavior and understanding its suitability for specific applications.

The V(z) curves were recorded with custom made acoustic microscope operated with frequency at 35, 100 and 200 MHz [101]. The acoustic lens is made of BK7 glass, the lens has an aperture of 1.88 mm. The coupling medium employed in this study to establish the interface between the lens and the specimen was distilled water. All measurements were performed at a constant room temperature throughout the experiment.

3.4 Absorption spectroscopy

The measurement of electromagnetic radiation absorption as a function of frequency or wavelength as a result of its interaction with a sample is known as absorption spectroscopy. The interaction of electromagnetic radiation with matter is accompanied by a decrease in the energy of the light wave. According to experiments, the beam intensity attenuation *dI* after passing through a different thickness *dx* can be expressed as:

$$dI = -\alpha I dx \tag{3.9},$$

where *I* is the intensity of light at a distance *x* into the medium, α is called the absorption coefficient of the material. Integrating the expression (3.9) we get the *Lambert-Beer law*:

$$I = I_0 e^{-\alpha x} \tag{3.10},$$

which establishes an exponential attenuation law between the incoming light intensity I_0 (the incident intensity minus the surface reflection losses) and the thickness x. Each layer of equal size absorbs an equal proportion of the incident monochromatic (i.e., one wavelength) radiation flux. The absorption coefficient is determined by the properties of the substance and generally depends on the wavelength λ of the absorbed light. This dependence is called the *absorption spectrum* of the substance [102].

The absorption of light by the material is caused by the presence of the corresponding electronic transitions in it (Fig.3.8 a).

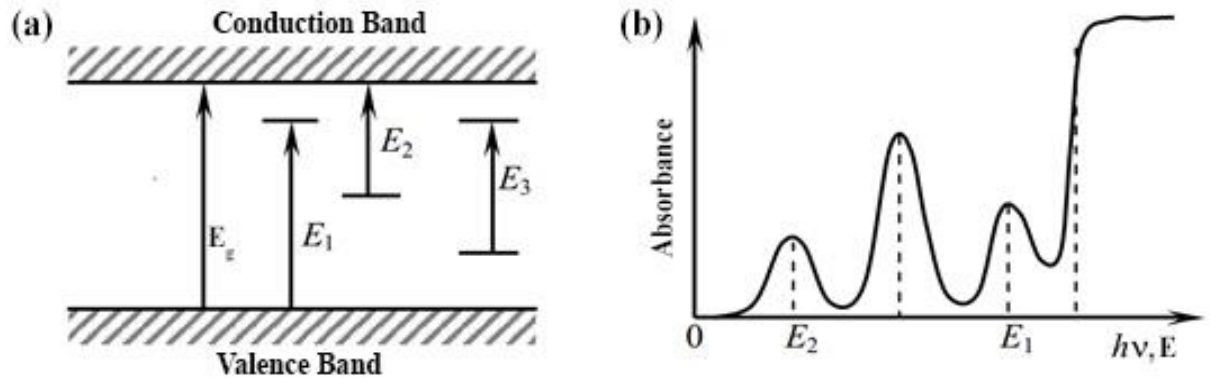

Fig. 3.8. Allowed transitions (a) and the corresponding absorption spectrum (b) in dielectrics ($E_g > E_1 > E_3 > E_2$).

Apart from the main (fundamental) absorption due to electron transitions from the valence band to the conduction band (E_g transition), additional absorption is possible due to the presence of energy levels within the band gap (E1, E2, E3 transitions), which appear with the introduction of impurities or structural defects into the matrix (Fig. 3.8 b).

Absorption spectra are usually registered by instruments known as spectrophotometers. Fig. 3.9a shows a schematic diagram with the main elements of the single-beam spectrophotometer.

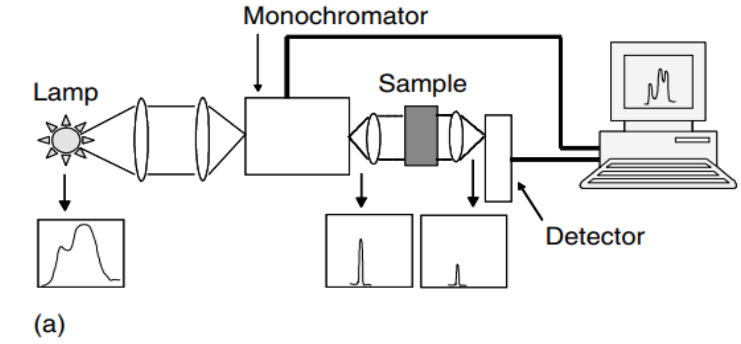

(a)

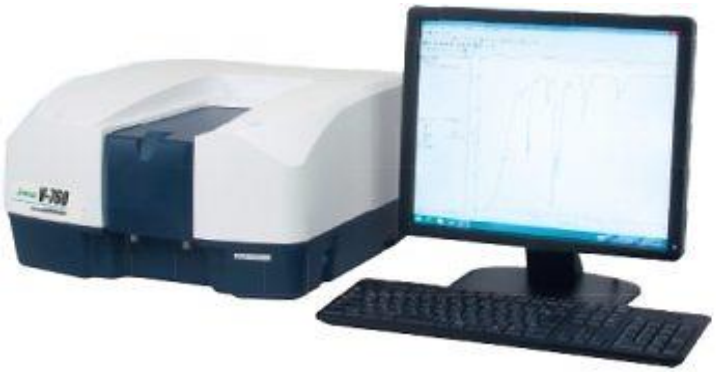

(b)

Fig.3.9 (a) - schematic diagram with the main elements of the single-beam spectrophotometer Jasco V-760 [103].

It consists of two light sources, deuterium and tungsten lamp for the UV and VIS/IR spectral ranges respectively. The light is focused on the entrance of the monochromator which is used to select a single wavelength during the absorption scan in the selected range. The intensity of each monochromatic beam after traversing the sample is measured with a light detector (UV-Vis photomultiplier; IR-SPb cell). Recording and analysis of the spectrum are carried out on a computer.

The absorption spectra presented in this work were measured using V-760 UV-Visible/ NIR spectrophotometer (Fig. 3.9 b). To ensure more accurate measurement over the broadest photometric range, the optical bench in the V-760 UV-visible spectrophotometer uses a double monochromator to provide exceptional resolution with extremely low stray light (0.00008%). The spectral bandwidth can be set as narrow as 0.1 nm for high-resolution measurements, such as gas and vapor phase spectroscopy in the 200-1000 nm range. The device is controlled using Spectra Manager™ innovative cross-platform spectroscopy software [103].

3.5 Luminescence spectroscopy

Photoluminescence spectroscopy (PL)

The PL emission and excitation (PLE) spectra were recorded with an Edinburgh Instruments FS5 Spectrofluorometer, equipped with a 150 W Xenon lamp as the excitation source (Fig. 3.10).

In the classical version of the method, radiation from a Xenon lamp enters an excitation monochromator (blue shoulder of the scheme), which at the output produces monochromatic radiation with a given wavelength, which is focused to a point a few millimeters in diameter on the sample surface. The emitted light is collected by a lens system and focused on the emission monochromator's inlet (red shoulder of the scheme). Inside the monochromator, a moving diffraction grating splits the light so that only photons of a certain wavelength (or a certain narrow range of wavelengths) reach the detector. The exciting beam reflected from the sample surface is cut off by a spectral filter installed at the entrance to the monochromator. The gradual rotation of the diffraction grating provides a measurement of the light intensity at each wavelength of the considered range. Thus, the radiation spectrum is measured in the experiment, that is, the dependence of the radiation intensity on its wavelength. In other words, if λ_{ex} (excitation wavelengths) is held constant and λ_{em} is scanned, then the luminescence spectrum is measured [104].

Photoluminescence excitation spectroscopy (PLE)

This type of photoluminescent spectroscopy differs from the classical one in that the sample is excited not at one wavelength, but successively by different wavelengths, while emission is detected only at one particular wavelength. For excitation at different wavelengths, a halogen lamp or a

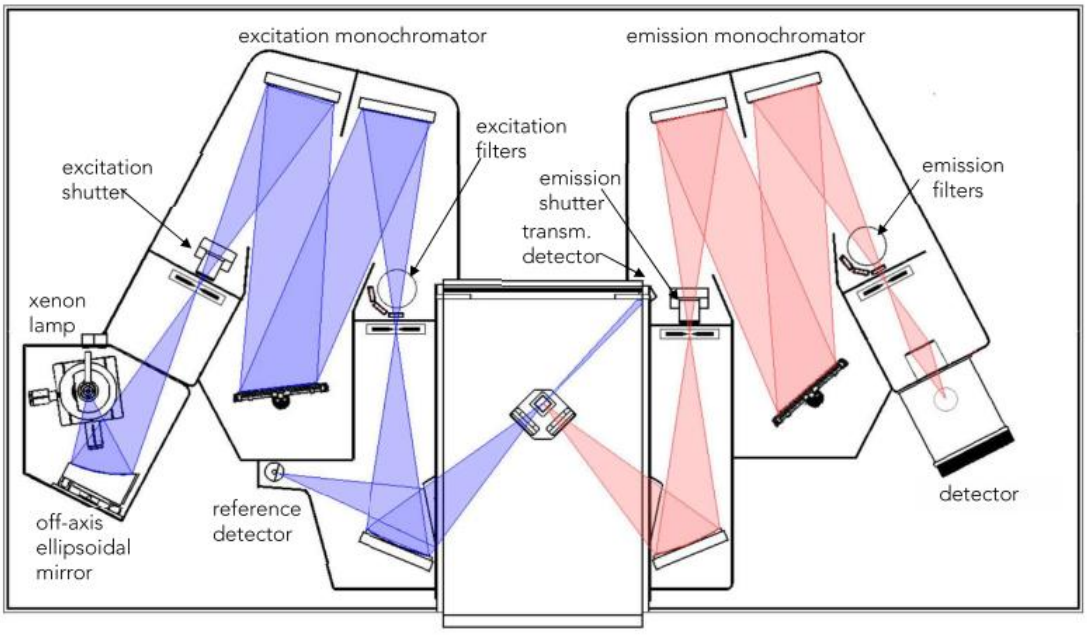

Fig. 3.10. Scheme of Edinburg FS5 spectrofluorometer [105].

combination of xenon and deuterium lamps and an excitation monochromator are used to select the desired excitation wavelength. This method makes it possible to effectively study the structure of energy levels in a sample since recombination between different energy levels becomes more clearly visible than in other methods. To sum up, if λ_{ex} is scanned at a constant λ_{em}, then a luminescence excitation spectrum is obtained (spectral dependence of the luminescence excitation efficiency on wavelength).

The above types of photoluminescence spectroscopy can be carried out at various temperatures (usually below room temperature) and in particular at liquid helium temperature (4K) or liquid nitrogen (77K). For this purpose, the sample is placed in a cryostat, in which a vacuum is created and liquid helium is supplied to the sample, which cools the sample. The heating element in the cryostat makes it possible to compensate for cooling and thus control the temperature, maintaining it at the desired level.

3.6 Colorimetry

Colorimetry is a branch of spectroscopy that deals with the measurement and description of colors. The theory behind colorimetry is based on the tristimulus theory of color perception, which posits that the human eye perceives color through the stimulation of three types of photoreceptor cells, known as cones. Each cone is most sensitive to a different range of wavelengths of light: one to short-wavelength light (**B**lue), one to medium-wavelength light (**G**reen), and one to long-wavelength light (**R**ed). Colorimetry's fundamental challenge is to measure the physiological perception of color resulting from a particular spectral color stimulus function $\varphi_\lambda(\lambda)$. The stimulation of RGB cones can be quantified by three numbers to describe any color that can be perceived by a person with normal vision [106].

In the 1930s, Wright and Guild conducted experiments where participants had to mix light at 435.8 nm, 546.1 nm, and 700 nm to create a color perception that matched the perception produced by monochromatic light at a specific wavelength within the visible spectrum (Fig.3.11). The outcome of

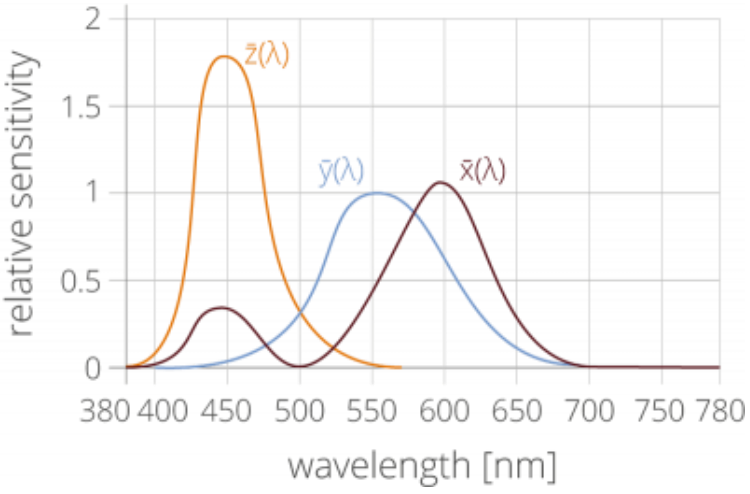

Fig. 3.11. XYZ color matching functions as defined by the CIE1931 standard colorimetric observer [107].

these experiments was the formulation of standardized RGB color matching functions $\bar{r}(\lambda), \bar{g}(\lambda), \bar{b}(\lambda)$. These standardized RGB color matching functions were subsequently converted into the CIE (International Commission on Illumination - *Commission Internationale de l'éclairage*) 1931 XYZ color matching functions $\bar{x}(\lambda), \bar{y}(\lambda)$, and $\bar{z}(\lambda)$. The CIE 1931 standard colorimetric observer is defined by these color matching functions, and they are applicable for an observer with a field of view of 2°.

The XYZ color matching functions can be employed to establish three parameters that accurately describe a particular color perception. To compute the XYZ tristimulus values of a specific spectral color stimulus function $\varphi_\lambda(\lambda)$, one can use the following equation:

$$\begin{aligned} X &= k_\lambda \int \varphi_\lambda(\lambda) \times \bar{x}(\lambda) d(\lambda) \\ Y &= k_\lambda \int \varphi_\lambda(\lambda) \times \bar{y}(\lambda) d(\lambda) \\ Z &= k_\lambda \int \varphi_\lambda(\lambda) \times \bar{z}(\lambda) d(\lambda) \end{aligned} \quad (3.11),$$

where λ represents the wavelength of the corresponding monochromatic light (in nanometers), and the standard range of the integral is between 380 and 780 nm. In case the spectral color stimulus $\varphi_\lambda(\lambda)$ describes a radiometric quantity of a primary light source with a value of k = 683 lm/W, then Y represents the corresponding photometric quantity.

Despite the fact that the XYZ tristimulus values create a three-dimensional color space that encompasses all conceivable color perceptions, a two-dimensional representation is generally sufficient for most purposes. The CIE 1931(x, y) chromaticity diagram is one such representation, where the x and y coordinates are obtained through a projection of the X, Y, and Z values [107]:

$$x = \frac{X}{X+Y+Z} \qquad y = \frac{Y}{X+Y+Z} \quad (3.12).$$

Another important colorimetric parameter is the correlated color temperature (CCT), which is based on the assumption that the color of a light source can be approximated by the color of a blackbody radiator at a certain temperature. The CCT is defined as the temperature of a blackbody radiator that has the same chromaticity coordinates as the light source or test sample. The CCT is expressed in Kelvin (K). The Planckian locus, shown in Fig.3.12b as a black curve, is a graphical depiction of a black body radiator's emission as it relates to its color temperature [108].

Color Rendering Index (CRI, Ra) is a metric that measures how well a light source reproduces the colors of an object compared to a natural or reference light source. CRI is calculated on a scale of 0 to 100, with a higher number indicating better color rendering ability. To calculate CRI, the color appearance of eight standardized test colors (R1 to R8) illuminated by a light source under test is compared to the same colors illuminated by a reference light source of the same CCT. In mathematical terms, Ra is defined as follows:

$$R_a = \frac{1}{8} \sum_{i=1}^{8} R_i \quad (3.13).$$

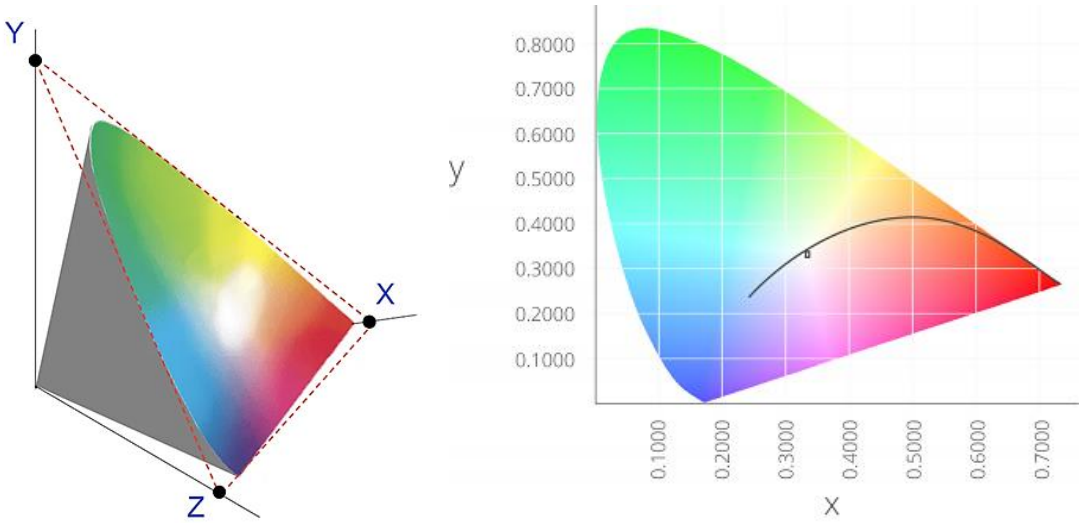

a) **b)**

Fig. 3.12. (a) - projection of XYZ Color Space on a **xy** Chromaticity Diagram-(a), (b) - the CIE 1931 (x,y) chromaticity diagram.

A scheme for measuring the color characteristics of fluorescent converters is shown in Fig. 3.13 The test sample is placed on the surface of the blue LED (1). An integrating sphere (2) is used to collect and register the total radiation.

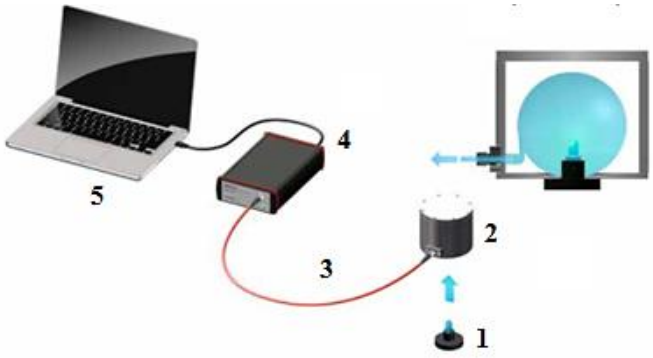

Fig. 3.13. Scheme of standard equipment for measuring the photoconversion properties of phosphors.

The principle of operation of the integrating sphere is that the light that enters the sphere through the input port undergoes multiple diffuse reflections and is uniformly distributed in the inner volume of the sphere. The inner surface of the integrating sphere is made of a material that provides high characteristics of diffuse reflection (> 96%) in a wide range of wavelengths (180-1200 nm) [109]. The receiving fiber optic cable (3) is connected to a connector located at a 90-degree angle relative to the input port in the section of the sphere that is separated by a partition. This arrangement ensures that the illuminance of the input aperture of the receiving light guide is independent of the angular distribution of light. After being collected by the sphere, the radiation is analyzed with a high-sensitivity optical fiber spectrometer, the AvaSpec-ULS2048-LTEC (4), that exhibits ultra-low light scattering across the

200 - 1100 nm range. To maintain optimal performance, the spectrometer's CCD detector is mounted on a cooling Peltier element that decreases its temperature by over 30 degrees Celsius. Reducing the inherent thermal noise of the detector by 2-3 times increases the spectrometer's dynamic range by over 10 times. The AvaSoft 8 program is used for data management and analysis. The spectral intensity is recorded in absolute units (μW/cm2/nm), which enables the generation of a chromatic diagram and extraction of color coordinates, color temperature, and dominant wavelength values from the program. The Osram LBE 6SG (I_f= 30 mA, V=2.9 V) blue LED 455 nm (30 mA, 2.9V) was used as an excitation source to determine the chromaticity parameters of the samples.

Conclusion to Chapter 3

In this chapter, we provide an overview of the experimental techniques used in the study. Each technique brings unique capabilities and contributes to a holistic understanding of the material properties. The techniques employed include:

1. **X-ray Diffraction (XRD):** XRD is a powerful tool for analyzing the crystal structure and determining the interatomic spacing within the samples. This technique enables precise measurements of lattice parameters, strain, and phase identification.
2. **Scanning Transmission Electron Microscopy (STEM**): STEM allows for high-resolution imaging and elemental mapping at the nanoscale. This technique provides valuable information about the morphology, composition, and crystal defects within the samples.
3. **Acoustic Microscopy:** Acoustic microscopy is employed to investigate the mechanical and elastic properties of the materials. By measuring the propagation of acoustic waves, valuable insights into the materials' internal structure and interfaces can be obtained.
4. **Absorption Spectroscopy:** Absorption spectroscopy is utilized to study the interaction of light with the materials. This technique provides information about the optical absorption properties, bandgap energy, and electronic transitions within the samples.
5. **Luminescence Spectroscopy:** Luminescence spectroscopy is employed to study the emission properties of the materials. By analyzing the emitted light, valuable information about the energy levels, radiative transitions, and luminescent efficiency of the samples can be obtained.
6. **Colorimetry:** Colorimetry is used to quantitatively measure and characterize the color properties of the materials. This technique enables the assessment of color coordinates, color purity, and color rendering properties.

With the integration of the abovementioned techniques, we have conducted a comprehensive investigation into the properties of SCF converters and composite color converters. The use of these experimental methods has provided valuable insights, advancing our understanding of new optoelectronic materials.

Chapter 4. Elasto-mechanical properties of epitaxial structures of garnet compounds

4.1 Elastic properties of cubic crystals

The main law of the theory of elasticity of solids in the region of small deformations is Hooke's law. Hooke's law in a generalized form can be written as:

$$\sigma_{ij} = c_{ijkl}\varepsilon_{kl} \quad (4.1),$$

where σ_{ij} is stress tensor, while ε_{kl} is the strain tensor. The strain tensor is defined as follows:

$$\varepsilon_{kl} = \frac{1}{2}\left(\frac{\partial u_k}{\partial x_l} + \frac{\partial u_l}{\partial x_k}\right) \quad (4.2),$$

where u_k and u_l are displacement vectors.

The coefficients of elastic stiffness c_{ijkl} form tensors of the fourth rank. Due to the symmetry of the tensor, instead of 81 coefficients of elasticity, 21 coefficients remain. It is more convenient to write the elasticity coefficients c_{ijkl} using matrix notation (Voigt notation) instead of tensor ones, reducing pairs of Cartesian integers to a single suffix and assuming summation of repeated indices from 1 to 6.

Tensor notation:	11	22	33	23	32	31	13	12	21
Matrix notation:	1	2	3	4		5		6	

Using this notation Hooke's law (Eq. 4.1) can be written in simplified form as:

$$\sigma_i = C_{ij}\varepsilon_j \ (i,j = 1,2,....6) \quad (4.3).$$

In the most general (anisotropic) case, the elastic stiffness matrix has 21 independent components because it is symmetric. Depending on a material's symmetry, the number of independent, nonzero stiffnesses will be further diminished [110]. This reduces the number of necessary stiffness moduli in the case of cubic crystals to three (c_{11}, c_{12}, c_{44}), as shown below:

$$C = \begin{bmatrix} C_{11} & C_{12} & C_{12} & 0 & 0 & 0 \\ C_{12} & C_{11} & C_{12} & 0 & 0 & 0 \\ C_{12} & C_{12} & C_{11} & 0 & 0 & 0 \\ 0 & 0 & 0 & C_{44} & 0 & 0 \\ 0 & 0 & 0 & 0 & C_{44} & 0 \\ 0 & 0 & 0 & 0 & 0 & C_{44} \end{bmatrix} \quad (4.4).$$

C_{11} represents the uniaxial deformation along [001] direction and C_{12} is a mixture of σ_{11} and σ_{22} (or the pure shear stress at (110) plane along [1 $\bar{1}$ 0] direction). The elastic stiffness enables us to obtain also the major elastic properties of a material described by the Zener anisotropy ratio (A), the isotropic shear modulus (G), Young's modulus (E), Poisson's ratio (ν), and the B/G relation given by:

$$A^z = \frac{2c_{44}}{c_{11} - c_{12}}$$

$$G = \frac{1}{2}\left[\frac{c_{11}-c_{12}+3c_{44}}{5} + \frac{5c_{44}(c_{11}-c_{12})}{4c_{44}+3(c_{11}-c_{12})}\right] \quad (4.5).$$

$$E = 2G(1+\nu)$$

$$\nu = \frac{E-2G}{2G}$$

Typical values of these quantities for a YAG crystal are summarized in Table 4.1.

Table 4.1 Typical values of mechanical properties of YAG crystal.

Source	**Method**	**C_{11}**	**C_{12}**	**C_{44}**	**E**	**G**	**ν**	**A^z**
		GPa	GPa	GPa	GPa	GPa	-	-
Alton et al. [111]	Ultrasonic	334	111	115	278.6	114	0.25	1.03
Chistyi et al. [112]	Brillouin scattering	333	114	114	274.8	274.8	0.26	1.04
Z. Huang et al. [26]	DFT(GGA) simulation	309.5	106.8	103.7	254.7	100.7	0.256	1.02

For the cubic crystal, if the interatomic force is central, then C_{12}= C_{14}. In Table 4.1, it is shown that the C_{12} of YAG is very close to C_{44}, but not equal. If the Cauchy relation (C_{12}=C_{14}) exists in cubic crystals, the Poisson ratio is rigidly equal to 0.25. From Table 4.1, we can find the Poisson ratio of most results is close to 0.25. If the Zener anisotropic ratio, calculated from Eq.4.6$_2$, $A^Z \approx 1$ the material can be considered isotropic, which means that the modulus is independent of orientation. From the calculated Zener anisotropic ratios in Table 4.1, the proportion of YAG's anisotropic nature is low.

For isotropic materials the stress tensor can be expressed in terms of the strain tensor, Young's modulus (E) and Poisson's ratio (σ)

$$\sigma_{ij} = \frac{E}{1+\nu}\left(\varepsilon_{ij} + \frac{\nu}{1-2\nu}\varepsilon_{ll}\delta_{ij}\right) \quad (4.6).$$

The mechanical, thermophysical, and acoustic-optical properties of these crystals depend on the elastic constants. If the elastic constants of garnets are known, the main parameters characterizing the mechanical and thermo-physical properties can be calculated. However, it is difficult to find in the literature the properties of simple garnets (YAG:Ce, LuAG:Ce), and even more difficult with mixed garnets or TbAG:Ce and GdAG:Ce which crystallization in the bulk form is extremely difficult or impossible is impossible [32].

4.2 Propagation of elastic waves

Oscillations excited at any point in the medium (solid, liquid, or gaseous) propagate in it with a finite speed, depending on the properties of the medium, being transmitted from one point of the medium to another. The further the particle of the medium is located from the source of oscillations, the later it will begin to oscillate. In other words, the phases of oscillations of the particles of the

medium and the source are more different from each other, the greater this distance. When studying the propagation of vibrations, the discrete (molecular) structure of the medium is not taken into account and the medium is considered as continuous, i.e., continuously distributed in space and possessing elastic properties. When a wave propagates, the particles of the medium do not move along with the wave but oscillate around their equilibrium positions. Together with the wave, only the state of the oscillatory motion and its energy are transferred from the particle to the particle of the medium. Therefore, the main property of all waves, regardless of their nature, is the transfer of energy without the transfer of matter.

Elastic (or mechanical) waves are mechanical disturbances propagating in an elastic medium. Elastic waves can be longitudinal and transverse. In longitudinal waves, particles of the medium oscillate in the direction of wave propagation, in transverse waves, in planes perpendicular to the direction of wave propagation. Longitudinal waves can propagate in media in which elastic forces arise during compressive and tensile deformation, i.e., solid, liquid, and gaseous bodies. Transverse waves can propagate in a medium in which elastic forces arise during shear deformation. Thus, in liquids and gases, only longitudinal waves arise, while in solids, both longitudinal and transverse waves can propagate. Let us further consider the propagation of ultrasonic waves in solids (substrate or film) and it will also be necessary to take into account the propagation of waves in liquids.

In this thesis, an experimental method of acoustic microscopy is proposed, which is very sensitive and can be applied to the ultrasonic examination of thin films. In general, an acoustic signal is sent through a sapphire cylinder into focusing lenses, after which the acoustic field is focused on the lens axis in a coupling medium (water). The coupling medium conducts acoustic pulses from the objective to the sample (a detailed description of the technique is explained in Chapter 3.3 of the thesis). Bulk wave propagation refers to waves that encounter no boundaries, like waves traveling in infinite media. For plates, rods, or tubes influence of the reflection and refraction from material boundaries on wave propagation should be considered. Thus, Solid-Solid/ Solid-Liquid/ Liquid-Solid boundary conditions may occur, depending on the studied material. Hence, for proper interpretation of ultrasonic results, it is necessary to propose a model of wave propagation in layered systems such as: i) fluid/substrate/fluid, ii) fluid/film/substrate/film/fluid (Fig. 4.1).

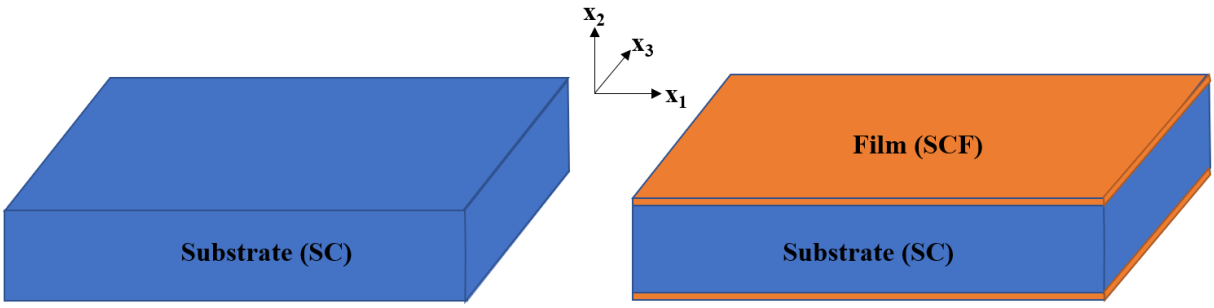

(a) **(b)**

Fig. 4.1(a)- schematically representation of the substrate and (b)-epitaxial structure.

4.3 Elastic waves in an isotropic medium

Wave propagation in an unbounded solid medium

To describe sound waves in continuous media, it is necessary to start by writing down the general equation of motion of an elastic medium:

$$\rho\ddot{u}_i = \frac{\partial\sigma_{ik}}{\partial x_k} \tag{4.7},$$

where: $\frac{\partial\sigma_{ik}}{\partial x_k}$ - internal stress force, $\ddot{u}_i$- acceleration, ρ- density of the unit volume of the body.

Substitute in Eq. (4.8) the expression of the strain (4.2) and stress (4.6) tensors the right-hand side of the equation (4.7) takes the form:

$$\rho\ddot{u}_i = \frac{E}{2(1+\nu)}\frac{\partial^2 u_i}{\partial x_k^2} + \frac{E}{2(1+\nu)(1-2\nu)}\frac{\partial^2 u_l}{\partial x_i \partial x_l} \tag{4.8},$$

which can be conveniently rewritten in vector notation

$$\rho\ddot{\boldsymbol{u}} = \frac{E}{2(1+\nu)}\Delta\boldsymbol{u} + \frac{E}{2(1+\nu)(1-2\nu)}\boldsymbol{\nabla}(\boldsymbol{\nabla}\cdot\boldsymbol{u}) \tag{4.9}.$$

The equation (4.9) can be rewritten as:

$$\ddot{\boldsymbol{u}} = c_t^2\Delta\boldsymbol{u} + (c_l^2 - c_t^2)\boldsymbol{\nabla}(\boldsymbol{\nabla}\cdot\boldsymbol{u}) \tag{4.10},$$

where the longitudinal and transverse speeds of sound c_l and c_t respectively, are introduced

$$c_l = \left[\frac{E(1-\nu)}{\rho(1+\nu)(1-2\nu)}\right]^{\frac{1}{2}}, \quad c_t = \left[\frac{E}{2\rho(1+\nu)}\right]^{\frac{1}{2}} \tag{4.11}.$$

For a monochromatic wave, the displacement vector can be written in the form:

$$\boldsymbol{u}(x_1, x_2, x_3, \mathrm{t}) = \bar{\boldsymbol{u}}\,(x_1, x_2, x_3)\exp(-i\omega t) \tag{4.12},$$

where $\bar{\boldsymbol{u}}\,(x_1, x_2, x_3)$ is a function of spatial coordinates only. Substituting (4.12) into (4.10) we can obtain the following equation

$$\bar{\boldsymbol{u}} = -\frac{1}{k_t^2}\Delta\bar{\boldsymbol{u}} - \left(\frac{1}{k_l^2} - \frac{1}{k_t^2}\right)\boldsymbol{\nabla}(\boldsymbol{\nabla}\cdot\bar{\boldsymbol{u}}) \tag{4.13},$$

where $k_l = \omega/c_l$ and $k_t = \omega/c_t$ are the wave numbers of the longitudinal and transverse waves, respectively.

It is known from vector analysis that the representation of a vector is always possible in the form of the sum of the rotor of a certain vector and the gradient of a certain scalar. Then, to solve equation (4.13), the so-called method of potentials can be used [113]. It is based on the decomposing of the spatial component of the displacement vector $\overline{\boldsymbol{u}}\,(x_1, x_2, x_3)$ into the sum of two components by introducing the potential function φ and the stream function $\boldsymbol{\psi}$.

$$\overline{\boldsymbol{u}} = \boldsymbol{\nabla}\varphi + \boldsymbol{\nabla} \times \boldsymbol{\psi} \tag{4.14}.$$

Applying the divergence and rotation operations on equations (4.13) and (4.14) and using the condition $\boldsymbol{\nabla}\,\boldsymbol{\psi} = 0$ the equations for the introduced potentials can be obtained.

$$\begin{aligned} \varphi &= -k_l^2 \Delta\varphi \\ \boldsymbol{\psi} &= k_t^2 \boldsymbol{\nabla} \times (\boldsymbol{\nabla} \times \boldsymbol{\psi}) \end{aligned} \tag{4.15}.$$

For two-dimensional case the scalar φ and vector $\boldsymbol{\psi}$ potentials can be expressed as:

$$\begin{aligned} \varphi(x_1, x_2) &= \varphi_0(x_2)\exp[i(kx_1 - \omega t)] \\ \boldsymbol{\psi}(x_1, x_2) &= \boldsymbol{\psi}_0(x_2)\exp[i(kx_1 - \omega t)] \end{aligned} \tag{4.16}.$$

Substituting expressions (4.16) into the Eq. 4.15_1 and Eq. 4.15_2 respectively (omitting the temporal components), two Helmholtz equations are obtained:

$$\begin{aligned} \frac{\partial^2 \varphi(x_1, x_2)}{\partial x_1^2} + \frac{\partial^2 \varphi(x_1, x_2)}{\partial x_2^2} + {k_l}^2 \varphi(x_1, x_2) = 0 \\ \frac{\partial^2 \boldsymbol{\psi}(x_1, x_2)}{\partial x_1^2} + \frac{\partial^2 \boldsymbol{\psi}(x_1, x_2)}{\partial x_2^2} + {k_t}^2 \boldsymbol{\psi}(x_1, x_2) = 0 \end{aligned} \tag{4.17}.$$

The solutions of equations (4.17) are as follows:

$$\begin{aligned} \varphi(x_1, x_2) &= \left(ae^{-i\alpha x_2} + be^{i\alpha x_2}\right)e^{ikx_1} \\ \boldsymbol{\psi}(x_1, x_2) &= \left(ce^{-i\beta x_2} + de^{i\beta x_2}\right)e^{ikx_1} \end{aligned} \tag{4.18},$$

where $\alpha = \sqrt{k_l^2 - k^2}$, $\beta = \sqrt{k_t^2 - k^2}$

These general solutions are suitable for describing wave propagation for an unbounded two-dimensional solid medium. In the following paragraphs the solutions for the case when the medium is a layer of a certain thickness and a half-space will be derived.

Wave propagation in solid layer

In Fig. 4.2 scheme of wave propagation in a solid layer is shown.

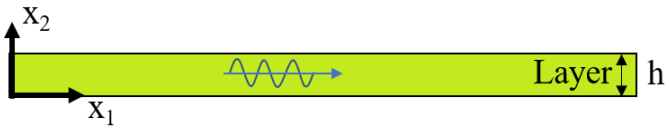

Fig. 4.2 Scheme of wave propagation in solid layer.

If the waves propagate along the x_1-axis within the x_1-x_2 plane, substituting Eq. (4.18) into Eq. (4.14) the displacement components of solid layer during wave propagation can be written as:

$$u_1 = \frac{\partial \varphi_1}{\partial x_1} + \frac{\partial \psi_1}{\partial x_2} = \left[a_1 ike^{-i\alpha_1 x_2} + b_1 ike^{i\alpha_1 x_2} - c_1 i\beta_1 e^{-i\beta_1 x_2} + d_1 i\beta_1 e^{i\beta_1 x_2}\right]e^{ikx_1}$$

$$u_2 = \frac{\partial \varphi_1}{\partial x_2} - \frac{\partial \psi_1}{\partial x_1} = \left[-a_1 i\alpha_1 e^{-i\alpha_1 x_2} + b_1 i\alpha_1 e^{i\alpha_1 x_2} - c_1 ike^{-i\beta_1 x_2} - d_1 ike^{i\beta_1 x_2}\right]e^{ikx_1} \quad (4.19),$$

where: $\alpha_1 = \sqrt{k_{l1}^2 - k^2}$, $\beta_1 = \sqrt{k_{t1}^2 - k^2}$ $k_{l1} = {}^{\omega}/_{c_{l1}}, k_{t1} = {}^{\omega}/_{c_{t1}}$.

For isotropic cases, the stress components of a solid can be expressed using Lame's constants (μ_1, λ_1) as follows:

$$\sigma_{ij} = \mu_1\left(u_{i,j} + u_{j,i}\right) + \lambda_1 u_{k,k}\delta_{ij} \quad (4.20).$$

Substituting Eq. (4.19) into Eq. (4.20) the stress components can be written as:

$$\sigma_{12} = \mu_1\left(\frac{\partial u_1}{\partial x_2} + \frac{\partial u_2}{\partial x_1}\right) =$$

$$= \left[a_1 2\mu_1 k\alpha_1 e^{-i\alpha_1 x_2} - b_1 2\mu_1 k\alpha_1 e^{i\alpha_1 x_2} + c_1\mu_1(k^2 - \beta_1^2)e^{-i\beta_1 x_2} + d_1\mu_1(k^2 - \beta_1^2)e^{i\beta_1 x_2}\right]e^{ikx_1}$$

$$\sigma_{22} = \mu_1\left(\frac{\partial u_2}{\partial x_2} + \frac{\partial u_2}{\partial x_2}\right) + \lambda_1\left(\frac{\partial u_1}{\partial x_1} + \frac{\partial u_2}{\partial x_2}\right) = \lambda_1\frac{\partial u_1}{\partial x_1} + (2\mu_1 + \lambda_1)\frac{\partial u_2}{\partial x_2} =$$

$$= \left[a_1\mu_1(k^2 - \beta_1^2)e^{-i\alpha_1 x_2} + b_1\mu_1(k^2 - \beta_1^2)e^{i\alpha_1 x_2} - c_1 2\beta_1 k\mu_1 e^{-i\beta_1 x_2} + d_1 k\beta_1 2\mu_1 e^{i\beta_1 x_2}\right]e^{ikx_1} \quad (4.21).$$

Wave propagation in solid half-space

In Fig. 4.3 scheme of wave propagation in solid half-space is shown.

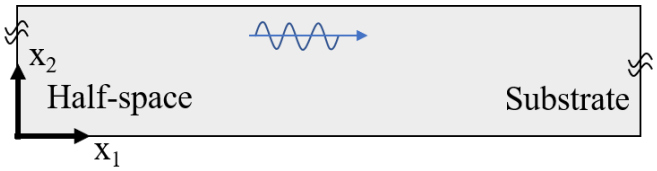

Fig. 4.3 Scheme of wave propagation in solid half-space.

General equations for potentials (4.18) in the case of a half-space take the following form,

$$\varphi_2 = a_2 e^{-i\alpha_2 x_2}e^{ikx_1}, \psi_2 = c_2 e^{-i\beta_2 x_2}e^{ikx_1} \quad (4.22).$$

To ensure that there are no displacements in half-space as x_2 approaches infinity, the values of b_2 and d_2 should be 0. In this case, the displacement and stress components for solid half-space can be written as:

$$u_1^s = \frac{\partial \varphi_2}{\partial x_1} + \frac{\partial \psi_2}{\partial x_2} = \left[a_2 ike^{-i\alpha_2 x_2} - c_2 i\beta_2 e^{-i\beta_1 x_2}\right]e^{ikx_1}$$

$$u_2^s = \frac{\partial \varphi_2}{\partial x_2} - \frac{\partial \psi_2}{\partial x_1} = \left[-a_2 i\alpha_2 e^{-i\alpha_2 x_2} - c_2 ike^{-i\beta_2 x_2}\right]e^{ikx_1} \quad (4.23)$$

$$\sigma_{12}^s = \mu_2\left(\frac{\partial u_1^s}{\partial x_2} + \frac{\partial u_2^s}{\partial x_1}\right) =$$

$$\left[a_2 2\mu_2 k\alpha_2 e^{-i\alpha_2 x_2} + c_2\mu_2(k^2-\beta_2^2)e^{-i\beta_2 x_2}\right]e^{ikx_1}$$

$$\sigma_{22}^s = \mu_2\left(\frac{\partial u_2^s}{\partial x_2}+\frac{\partial u_2^s}{\partial x_2}\right)+\lambda_2\left(\frac{\partial u_1^s}{\partial x_1}+\frac{\partial u_2^s}{\partial x_2}\right)=\lambda_2\frac{\partial u_1^s}{\partial x_1}+(2\mu_2+\lambda_2)\frac{\partial u_2^s}{\partial x_2}=$$

$$\left[a_2\mu_2(k^2-\beta_2^2)e^{-i\alpha_2 x_2} + c_2 2\beta_2 k\mu_2 e^{-i\beta_2 x_2}\right]e^{ikx_1} \qquad (4.24)$$

4.4 Elastic wave propagation in an ideal fluid

- ***Wave propagation in unbounded fluid media***

The main focus of this section will be paid on examining the propagation of a plane harmonic wave through a layer of an ideal fluid (the shear and volumetric viscosity are equal to zero). The starting point for the considerations to obtain the equation governing wave propagation in the fluid are: the linear Navier-Stokes equation for an ideal fluid; continuity equation and equation of state:

$$\begin{aligned} \rho^f\frac{\partial \boldsymbol{V}^f}{\partial t} &= -\boldsymbol{\nabla} p \\ \frac{\partial \rho^f}{\partial t}+\rho^f\boldsymbol{\nabla}\cdot\boldsymbol{V}^f &= 0 \\ p &= c_0^2\rho^f \end{aligned} \qquad (4.25),$$

where c_0 is the velocity of the acoustic wave in the fluid, p - fluid pressure, $\boldsymbol{V}^f$ the fluid particle velocity and ρ^f is the fluid mass density.

Differentiating equations (4.25_1) and (4.25_3) with respect to time, we obtain another form of Eq. (4.25):

$$\begin{aligned} \rho^f\frac{\partial^2 \boldsymbol{V}^f}{\partial t^2} &= -\boldsymbol{\nabla}\frac{\partial p}{\partial t} \\ \frac{\partial \rho^f}{\partial t}+\rho^f\boldsymbol{\nabla}\cdot\boldsymbol{V}^f &= 0 \\ \frac{\partial p}{\partial t} &= c_0^2\frac{\partial \rho^f}{\partial t} \end{aligned} \qquad (4.26).$$

Substituting (4.26_2) into (4.26_3) and then the resulting expression into (4.26_1) we obtain the differential equation of wave propagation in an ideal fluid:

$$\frac{\partial^2 \boldsymbol{V}^f}{\partial t^2} = c_0^2\boldsymbol{\nabla}(\boldsymbol{\nabla}\cdot\boldsymbol{V}^f) \qquad (4.27).$$

Describing the medium disturbance accompanying the propagation of a harmonic wave, the velocity field vector $\boldsymbol{V}^f$ can be decomposed into the product of two factors: time dependent $e^{-i\omega t}$ and spatial dependent $\overline{\boldsymbol{V}}^f(x_1,x_2,x_3)$ components, which can be written as:

$$\boldsymbol{V}^f = \overline{\boldsymbol{V}}^f(x_1,x_2,x_3)e^{-i\omega t} \qquad (4.28),$$

where ω is the circular frequency and $i = \sqrt{-1}$. Substituting (4.28) into (4.27) and grouping like terms, we obtain an equation describing the spatial components of the velocities of the particles of an ideal fluid during the propagation of a monochromatic wave, which we can write as follows.

$$\overline{\boldsymbol{V}}^f = -\frac{1}{k_f^2}\boldsymbol{\nabla}(\boldsymbol{\nabla}\cdot\overline{\boldsymbol{V}}^f) \tag{4.29},$$

where $k_f = \frac{\omega}{c_0}$ is the wavenumber in an unbounded fluid medium.

As in the Section 4.3, we are looking for a solution using the potential method by separating the spatial component of the velocity vector of fluid particles $\overline{\boldsymbol{V}}^f(x_1, x_2, x_3)$ into the sum of two components (potentials) of the form:

$$\overline{\boldsymbol{V}}^f = \boldsymbol{\nabla}\varphi^f + \boldsymbol{\nabla}\times\boldsymbol{\psi}^f \tag{4.30}.$$

Substituting (4.30) in (4.29), we obtain:

$$\overline{\boldsymbol{V}}^f = -\frac{1}{k_f^2}\boldsymbol{\nabla}(\boldsymbol{\nabla}\,(\boldsymbol{\nabla}\varphi^f + \boldsymbol{\nabla}\times\boldsymbol{\psi}^f) = -\frac{1}{k_f^2}\boldsymbol{\nabla}(\Delta\varphi^f) \tag{4.31}.$$

It means that the spatial components of the velocity of fluid particles will be expressed only in terms of the scalar potential ($\overline{\boldsymbol{V}}^f = \boldsymbol{\nabla}\varphi^f$). It can be determined from the following Helmholtz equations:

$$\Delta\varphi^f + k_f^2\varphi^f = 0 \tag{4.32}.$$

The solution of equation (4.32) for a plane harmonic wave propagating in x_1 axis is a function of the form:

$$\varphi = \left(ae^{-i\alpha_f x_2} + be^{i\alpha_f x_2}\right)e^{ikx_1} \tag{4.33},$$

where $\alpha_f = \sqrt{k_f^2 - k_0^2}$.

- ***Wave propagation in fluid half-space***

In Fig. 4.4 scheme of wave propagation in fluid half-space is shown.

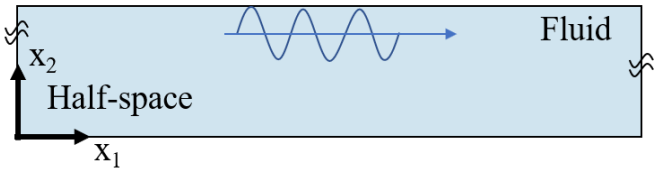

Fig. 4.4 Scheme of wave propagation in fluid half-space.

As the displacements should be zero when $\mathbf{x}_2$ tends to infinity thus the constant a in Eq. (4.33) should be equal to zero and expression for the scalar potential takes a simplified form as:

$$\varphi_3 = b_3e^{i\alpha_3 x_2}e^{ikx_1} \tag{4.34},$$

where: $\alpha_3 = \sqrt{k_{l3}^2 - k^2}$ and $k_{l3} = {}^{\omega}/_{c_{l3}}$.

Substitution of Eq. (4.34) into Eq.(4.30) gives the velocities components of ideal fluid:

$$\bar{V}_1^f = \frac{\partial\varphi_3}{\partial x_1} = ikb_3e^{i\alpha_3 x_2}e^{ikx_1}$$

$$\bar{V}_2^f = \frac{\partial \varphi_3}{\partial x_2} = i\alpha_3 b_3 e^{i\alpha_3 x_2} e^{ikx_1} \quad \ldots \quad (4.35).$$

Given the velocity of the fluid particles, the displacements of fluid components (integrals of velocity with respect to time) can be derived as follows:

$$u_1^f = \int V_1^f \, dt = \omega k b_3 e^{i\alpha_3 x_2} e^{ikx_1}$$

$$u_2^f = \int V_2^f \, dt = \omega \alpha_3 b_3 e^{i\alpha_3 x_2} e^{ikx_1} \quad (4.36).$$

In the ideal fluid, tangential stresses are equal to zero normal stresses are limited only to pressure.

$$\sigma_{ij}^f = -p\delta_{ij} \quad (4.37).$$

$$p = -\lambda_3 \left(\frac{\partial u_1^f}{\partial x_1} + \frac{\partial u_2^f}{\partial x_2} \right) = b_3 \lambda_3 (k^2 + \alpha_3^2) e^{i\alpha_3 x_2} e^{ikx_1} \quad (4.38),$$

where $\lambda_3 = \rho^f c_0^2$.

4.5 Elastic wave propagation in layered structures

The elastic waves in layered structures are guided and that means they are dispersive; i.e., the phase velocities vary with the frequencies. To obtain the dispersion relation, the equations of motion obtained in the previous sections for a plane wave in a liquid and a solid, are used to proceed with the description of the layered structures. Accordingly, to the geometry of the acoustic microscopy experiment (see Section 3.3) and the objects under study, in this section we propose two simplified models of propagation of an ultrasonic wave, corresponding to measurements of substrate (model M1) and substrate with grown on it SCF (model M2). In Fig.4.5, the schemes of these two models are shown.

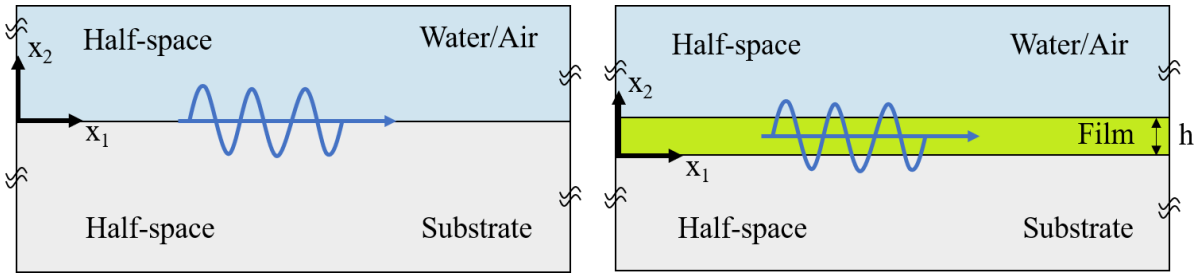

(a) Model M1 (b) Model M2

Fig.4.5. a-fluid/substrate (model M1) and (b)-fluid/film/substrate (model M2).

For modeling of wave propagation in the YAG substrate with the thickness (L=500 μm), the simplified model of two adjacent half spaces is considered. The upper half-space is occupied by fluid (water) or air, while the lower by the substrate. Considering the substrate layer as a solid half-space is justified by the fact that the thickness of the substrate (L) is much greater than the wavelengths (λ=20-80 μm) calculated for the range of frequencies (35-200 MHz) used in acoustic microscopy experiments.

Similar reasoning is applied for modeling wave propagation for the YAG substrate and LuAG:Ce SCF with the thickness (h ≈ 30 μm) grown onto it. In this case, two half-spaces of YAG substrate and coupling fluid are separated by a thin layer (film). For low frequencies (~35 MHz) the wavelengths (λ~80 μm) are greater than the film thickness. For the higher frequencies (100 and 200 MHz) the wavelengths (λ=20-40 μm), became closer to the film thickness and justified the choice of the model.

Interfacial conditions

To find analytical solutions for both models the relationships derived in sections 4.3 and 4.4 (concerning the displacements and stress component for a specific medium), need to satisfy specific interfacial boundary conditions (ICs). For both models, we will consider that the upper half-space can be occupied by liquid fluid (water or air) thus two sets of ICs are proposed.

- interfacial boundary conditions ($x_2=0$) for model *M1*

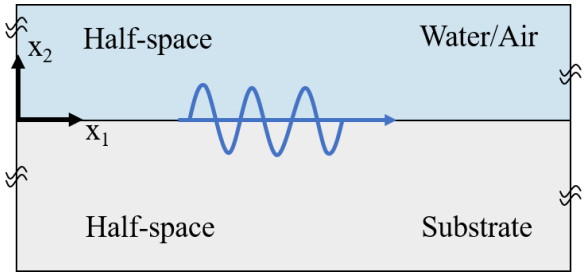

Water Air

$$\begin{cases} u_2^s = u_2^f \\ \sigma_{22}^s = 0 \\ \sigma_{12}^s = 0 \end{cases} \quad x_2=0 \quad \begin{cases} \sigma_{22}^s = 0 \\ \sigma_{12}^s = 0 \end{cases} \qquad (4.39).$$

- interfacial boundary conditions ($x_2=0$ *and* $x_2=h$) for model *M2*

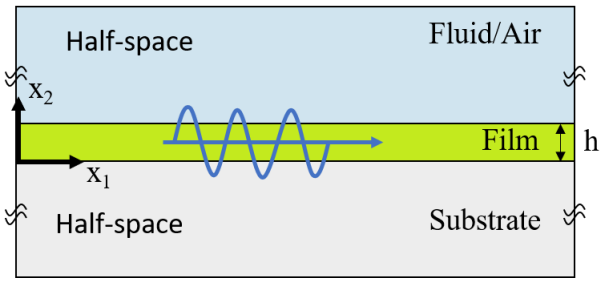

Liquid(water) Air

$$\begin{cases} u_1 = u_1^s \\ u_2 = u_2^s \\ \sigma_{22=}\ \sigma_{22}^s \\ \sigma_{12=}\ \sigma_{12}^s \end{cases} \quad x_2=0 \quad \begin{cases} u_1 = u_1^s \\ u_2 = u_2^s \\ \sigma_{22=}\ \sigma_{22}^s \\ \sigma_{12=}\ \sigma_{12}^s \end{cases}$$

(4.40).

$$\begin{cases} u_2 = u_2^f \\ \sigma_{22=} - p \\ \sigma_{12=} 0 \end{cases} \qquad x_2=h \qquad \begin{cases} u_2 = u_2^f \\ \sigma_{12=} 0 \end{cases}$$

Substitution of appropriate expressions for the displacements and stresses into interfacial conditions leads to a set of linear algebraic equations, which can be generally written in matrix form as:

$$\boldsymbol{M}[a_1, b_1, c_1, d_1, a_2, c_2, b_3]^T=0 \tag{4.41}$$

The requirement for the existence of nontrivial solutions of Eq. (4.41) is that

$$\det(\boldsymbol{M}) = 0 \tag{4.42}$$

determines the dispersion relationships of the guided waves.

For model M1 and liquid in the upper half space the matrix can be written as:

$$M_1^{water} = \begin{bmatrix} -\alpha_2 & -k & \alpha_3\omega \\ \mu_2\left(k^2 - \beta_2^2\right) & 2\mu_2 k\beta_2 & 0 \\ 2\mu_2 k\alpha_2 & \mu_2\left(k^2 - \beta_2^2\right) & 0 \end{bmatrix} \tag{4.43}$$

When the water is replaced by air the simplified version of the relationship (4.43) can be derived:

$$M_1^{air} = \begin{bmatrix} \mu_2\left(k^2 - \beta_2^2\right) & 2\mu_2 k\beta_2 \\ 2\mu_2 k\alpha_2 & \mu_2\left(k^2 - \beta_2^2\right) \end{bmatrix} \tag{4.44}$$

In turn, for model M2 and liquid in the upper half space the matrix can be written as:

$$M_2^{liquid} = \begin{bmatrix} k & k & -\beta_1 & \beta_1 & -k & \beta_2 & 0 \\ -\alpha_1 & \alpha_1 & -k & -k & \alpha_2 & k & 0 \\ \mu_1(k^2-\beta_1^2) & \mu_1(k^2-\beta_1^2) & -2\mu_1 k\beta_1 & 2\mu_1 k\beta_1 & -\mu_2(k^2-\beta_2^2) & 2\mu_2 k\beta_2 & 0 \\ 2\mu_1 k\alpha_1 & -2\mu_1 k\alpha_1 & \mu_1(k^2-\beta_1^2) & \mu_1(k^2-\beta_1^2) & -2\mu_2 k\alpha_2 & -\mu_2(k^2-\beta_2^2) & 0 \\ -\alpha_1 e^{-i\alpha_1 h} & \alpha_1 e^{i\alpha_1 h} & -ke^{-i\beta_1 h} & -ke^{i\beta_1 h} & 0 & 0 & -\alpha_3\omega e^{i\alpha_3 h} \\ \mu_1(k^2-\beta_1^2)e^{-i\alpha_1 h} & \mu_1(k^2-\beta_1^2)e^{i\alpha_1 h} & -2\mu_1 k\beta_1 e^{-i\beta_1 h} & 2\mu_1 k\beta_1 e^{i\beta_1 h} & 0 & 0 & \lambda_3(\alpha_3^2+k^2)e^{i\alpha_3 h} \\ 2k\alpha_1 e^{-i\alpha_1 h} & -2k\alpha_1 e^{i\alpha_1 h} & (k^2-\beta_1^2)e^{-i\beta_1 h} & (k^2-\beta_1^2)e^{i\beta_1 h} & 0 & 0 & 0 \end{bmatrix} \tag{4.45}$$

When the water half-space is replaced by air half-space the simplified version of the relationship (4.45) can be derived:

$$M_2^{air} = \begin{bmatrix} k & k & -\beta_1 & \beta_1 & -k & \beta_2 \\ -\alpha_1 & \alpha_1 & -k & -k & \alpha_2 & k \\ \mu_1(k^2-\beta_1^2) & \mu_1(k^2-\beta_1^2) & -2\mu_1 k\beta_1 & 2\mu_1 k\beta_1 & -\mu_2(k^2-\beta_2^2) & 2\mu_2 k\beta_2 \\ 2\mu_1 k\alpha_1 & -2\mu_1 k\alpha_1 & \mu_1(k^2-\beta_1^2) & \mu_1(k^2-\beta_1^2) & -2\mu_2 k\alpha_2 & -\mu_2(k^2-\beta_2^2) \\ -\alpha_1 e^{-i\alpha_1 h} & \alpha_1 e^{i\alpha_1 h} & -ke^{-i\beta_1 h} & -ke^{i\beta_1 h} & 0 & 0 \\ 2k\alpha_1 e^{-i\alpha_1 h} & -2k\alpha_1 e^{i\alpha_1 h} & (k^2-\beta_1^2)e^{-i\beta_1 h} & (k^2-\beta_1^2)e^{i\beta_1 h} & 0 & 0 \end{bmatrix} \tag{4.46}$$

Conclusion to Chapter 4

Throughout this chapter, we have emphasized the significance of elasticity in characterizing the mechanical properties of materials and understanding wave phenomena. By gaining insights into the main law of elasticity and wave propagation, we can further our knowledge in fields such as materials science, mechanical engineering, and acoustics. As part of theoretical and numerical research, a microscopic model for a layered epitaxial structure was developed to explain the propagation of ultrasonic waves with wavelengths comparable to the thickness of the film.

Chapter 5. Acoustoelastic properties of LuAG:Ce film/YAG:Ce crystal epitaxial structures

5.1 Acoustic microscopy investigation of YAG:Ce crystal and LuAG:Ce film/YAG:Ce crystal epitaxial structure

In this section, the experimental results on measuring the phase velocity of acoustic surface waves on YAG:Ce substrate and LuAG:Ce SCF/YAG:Ce SC epitaxial structure. A schematic representation of the studied structures is shown in Fig. 5.1.

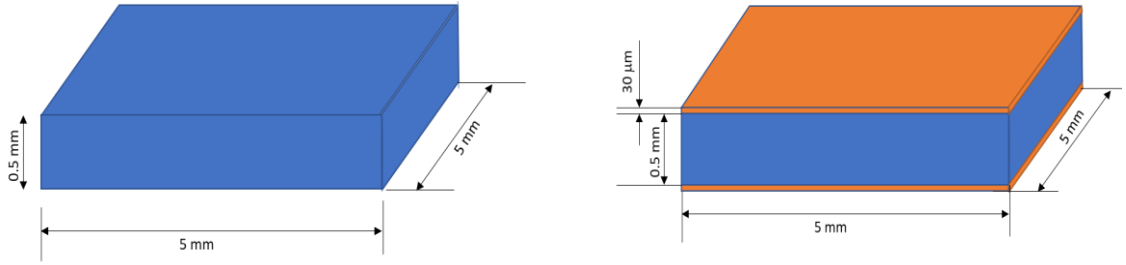

a) YAG:Ce substrate b) LuAG/YAG:Ce SC epitaxial structure

Fig. 5.1 Schemes of the geometry of measured samples.

For each sample, a V(z) curve was obtained by using an acoustic microscope (see section 3.3). The Δz value was measured for each specimen at different wave frequencies (35;100; 200 MHz), and the surface acoustic wave velocity was calculated using Eq. (3.7). To minimize measurement errors, the V(z) curve was measured 5 times for each sample at different positions of their surfaces.

First, acoustic microscopy measurements were performed for YAG:Ce substrate. Fig.5.2 demonstrates the exemplary V(z) curve for YAG:Ce substrate sample of thickness (500 µm) obtained using a 200 MHz transducer.

The velocity of the surface acoustic wave was determined by measuring the spacing Δz between successive minima and maxima in the V(z) curve pattern. The calculated phase velocities measured at different excitation frequencies for YAG:Ce substrate are presented in Table 5.1.

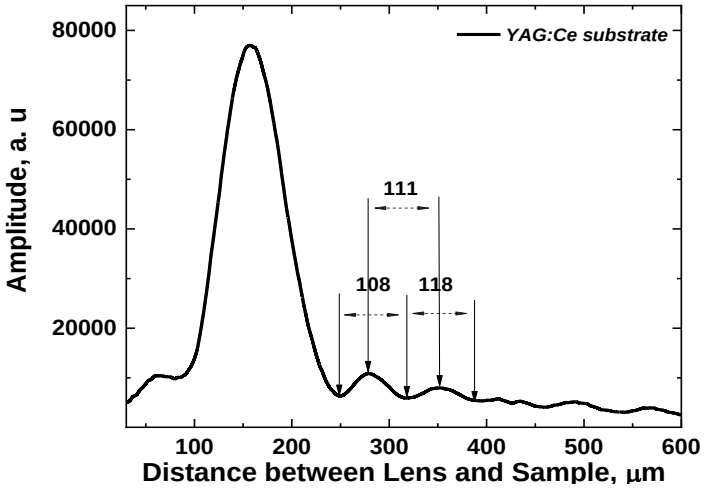

Fig. 5.2 Exemplary V(z) curve for YAG:Ce SC substrate measured using 200 MHz transducer.

Table 5.1. Measured phase velocities in YAG:Ce substrate for three frequencies.

Frequency, MHz	Phase velocity, m/s
35	4633 ± 57
100	4648 ± 33
200	4596 ± 45

It can be seen from the table that measured values of the phase velocity are very close and weakly depend on the frequency of the exciting wave. Thus, we conclude that the dispersion in the experimental frequency range (35-200 MHz) is small. The wavelengths calculated as a ratio of wave velocity and transducer frequency (*λ=velocity/frequency*) range from 130 μm (for 35 MHz transducer) to 23 μm (for 200 MHz transducer). The obtained results for YAG:Ce SC substrate are expected because the above-mentioned wavelengths are at least 5 times smaller than the substrate thickness (500 μm). Thus, it seems justified to conclude that in this case, a nondispersive surface Rayleigh type of wave propagates in the YAG:Ce substrate material.

In the second stage, the V(z) acoustic curves for the epitaxial structures at different frequencies were measured. In Fig. 5.3, the exemplary curve measured by a 100 MHz transducer is shown for the epitaxial structure containing YAG:Ce SC substrate with 500 μm thickness covered by LuAG:Ce SCF with the thickness of ~30 μm.

The calculated values of the phase velocities obtained at three frequencies are summarized in Table 5.2. The SAWs in epitaxial structure exhibit a dispersive nature, meaning that their phase velocity depends on their frequency. This dispersion is a consequence of the complex interaction of the surface wave with the layered structure of the material.

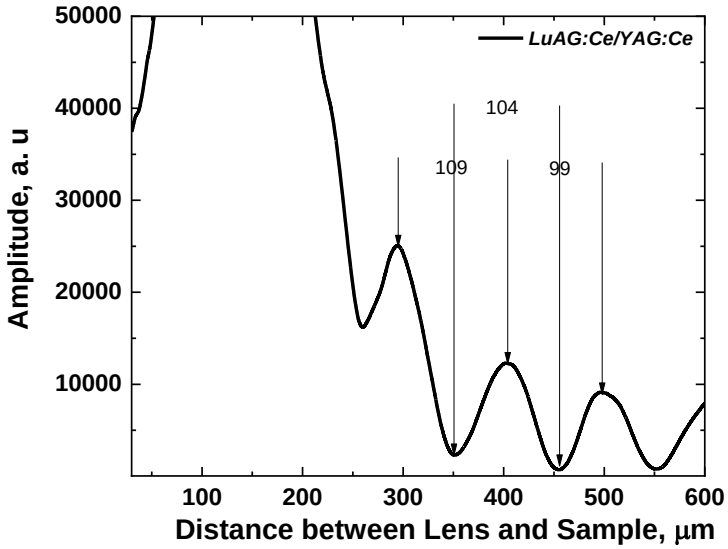

Fig.5.3 Exemplary V(z) curve for LuAG:Ce SCF/YAG:Ce SC substrate epitaxial structure measured using 100 MHz transducer.

Table 5.2 Measured phase velocities in LuAG:Ce SCF/YAG:Ce SC epitaxial structure.

Frequency, MHz	Phase velocity, m/s
35	4177 ± 95
100	3986 ± 150
200	5052 ± 135

5.2 Comparison of model predictions with experimental results

To obtain a dispersion curve experimentally, a significant number of measurements need to be conducted using ultrasonic transducers with a precise frequency increment. The other solution is to use the wideband transducers and ultrasonic spectroscopy method. The above-mentioned experimental methods are difficult to apply for samples of small dimensions. Thus, the present study employs an alternative approach that involves the validation of experimental data by comparing them to predictions derived from a theoretical model. In Section 4.5, the problem of harmonic wave propagation in a substrate and film/substrate structures was considered. In this section, the numerical solution of the proposed models regarding the phase velocity will be presented. Solving numerical models of physical processes is crucial as it provides a deeper understanding of complex phenomena and enables exploration of inaccessible conditions. In the thesis, the MATLAB programming software was used to solve numerically the dispersion equations.

Initially, the microscopic material parameters used in the model were taken from the literature [26, 114]. Table 5.3 presents a list of initial parameters that were utilized in the numerical calculations related to the M1 and M2 models.

Fig. 5.4 demonstrates numerically calculated dispersion curves for the M1 model. In this model wave propagation in two-adjacent half-spaces is considered (see Section 4.4). To simulate experimental conditions two cases were examined i.e. the case when the upper half-space is occupied by water or air while the bottom half-space was YAG:Ce SC substrate.

Table 5.3. Input material parameters for the numerical calculations of the models.

Parameter	Symbol	Value
Density of bulk YAG:Ce	ρ^s	6000 [g/cm^3]
Density of bulk LuAG:Ce	ρ^l	4500[g/cm^3]
Density of the fluid	ρ_f	1000 [g/cm^3]
Density of the air	ρ_a	1 [g/cm^3]
Speed of sound in the fluid	V_f	1500 [m/s]
Velocity of a longitudinal and shear wave in YAG:Ce SC substrate	c_L^s, c_{SH}^s	8500, 5070 [m/s]
The velocity of a longitudinal and shear wave in LuAG:Ce layer	c_L^l, c_{SH}^l	7000, 4500 [m/s]

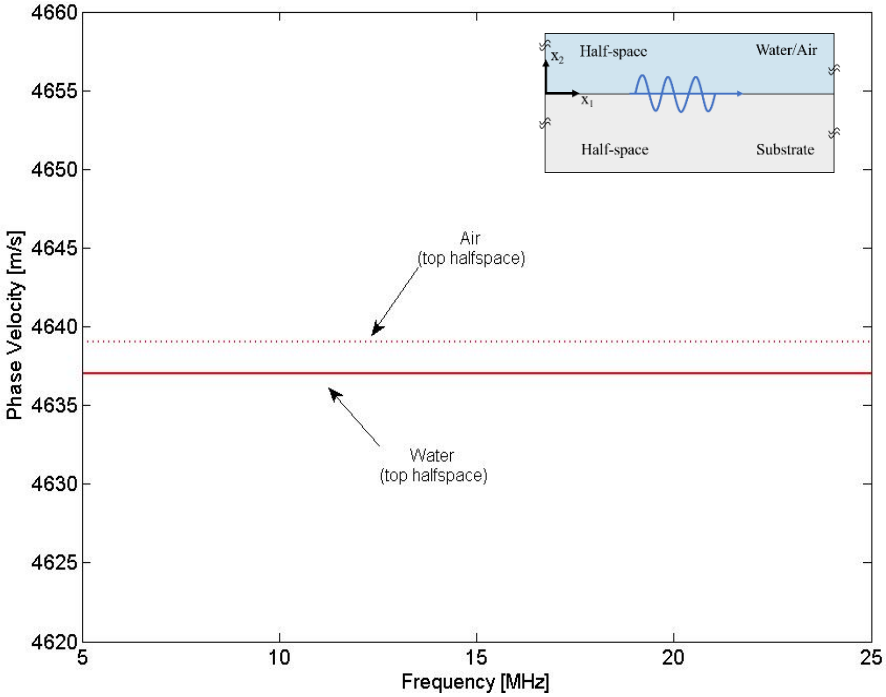

Fig. 5.4 Phase velocity dispersion curve for M1 model (two-adjacent half-spaces). The upper half-space is occupied by water or air while the bottom half-space is by YAG:Ce SC substrate.

In ultrasonic microscopy experiments, the focused probe is immersed in water (coupling medium) to ensure the transmission of the wave to the sample. The wave propagates mainly in the solid sample, but part of its energy leaks to the coupling medium which, in general, may lead to the dispersion. The results presented in Fig. 5.4 show, that theoretical predictions of the dispersion curves differ very little when the water is replaced by air (within 2-3 m/s). Thus, we conclude that the presence of water or air in the top half-space practically does not influence the wave velocity in the substrate (solid) and in further analysis, a simplified model (with air in the upper half-space) will be used.

In Fig. 5.5 the experimental results (from ultrasonic microscopy) with error bars for the YAG:Ce SC substrate are compared with the dispersion curves numerically calculated for the simplified M1 model. The experimental values overlap to a large extent with the simulated results in the low-frequency region. For a frequency of 200 MHz, there is a deviation of the experimental data to the region of lower phase velocities, which can be associated with experimental errors.

In Fig. 5.6 a similar comparison of measured and theoretically predicted phase velocity dispersion for an epitaxial structure LuAG:Ce SCF/YAG:Ce SC is shown. Within the considered frequency range theory predict the existence of three different modes (B0, B1, B2). The B0 (fundamental) mode exists in the whole frequency range, while the higher order modes (B1, B2) in the higher frequencies. Based on the results shown in Fig. 5.6, one can conclude, that in the experiments for an epitaxial structure LuAG:Ce/YAG:Ce only B1 and B2 wave modes are observed. The absence of experimental results lying in the region of the B0 mode is most likely associated with the sensitivity of the measuring equipment.

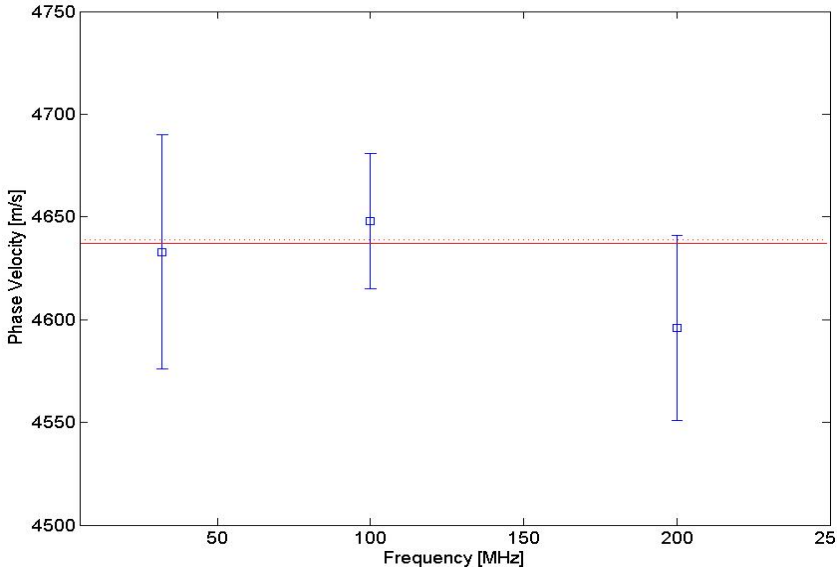

Fig. 5.5 Comparison of calculated (red continuous and dotted line) and measured (blue squares) phase velocities for YAG:Ce substrate.

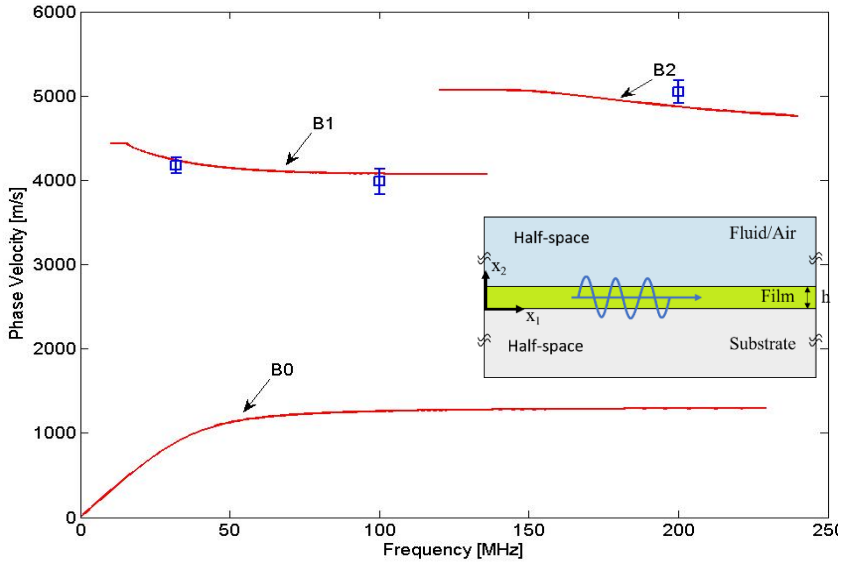

Fig. 5.6 Comparison of calculated (red lines) and measured (blue squares) phase velocities for YAG:Ce/LuAG:Ce epitaxial structure.

5.3 Extraction of material properties based on the optimization procedure

The model's accuracy and reliability need to be assessed by comparing its predictions with experimental data from well-designed experiments. This validation process helps establish confidence in the model's ability to accurately represent the physical process under investigation. The optimization procedure involves comparing the calculated or predicted velocities of the wave modes with the experimental results. This process aims to find the best set of parameters or conditions that can reproduce the observed modes most accurately. During the optimization, various parameters related to the material properties or experimental setup may be adjusted or fine-tuned. These parameters can

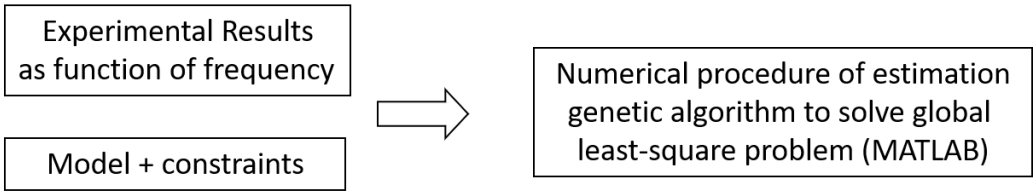

Fig.5.7. Block diagram of the optimization process

include dimensions, compositions, boundary conditions, or any other relevant variables that affect the wave modes. The optimization procedure typically involves iterative steps, where the calculated values are compared with the experimental data, schematically shown in Fig. 5.7. Based on the level of agreement or discrepancy between the two parameters are adjusted, and the calculation is repeated. In the context of modeling, optimization is often used to minimize a cost function. The cost function represents the measure of error or discrepancy between the predicted and actual values.

To minimize the cost function, the optimization procedure iteratively adjusts the parameters of the model or algorithm to find the values that yield the lowest cost. This process involves searching through the parameter space to identify the optimal configuration. There are various optimization algorithms available, each with its own advantages and limitations. Some commonly used techniques include gradient descent, stochastic gradient descent, Newton's method, and genetic algorithms. In the context of this work, a standard genetic algorithm toolbox embedded in the MATLAB libraries was chosen [115]. Genetic algorithms are a type of evolutionary optimization method inspired by natural selection. They involve the creation of a population of candidate solutions, where each solution represents a set of parameters. Through selection, crossover, and mutation operations, the algorithm evolves the population over generations to find the optimal solution.

The cost function (CF) is defined as follows:

$$CF = \sum_{i=1}^{N} [y_i(f) - H(\boldsymbol{b}, f)]^2 \quad (5.1),$$

where y_i – vector experimental phase velocities,

f – frequency

H – model predictions (phase velocity) for a given frequency (f)

$\boldsymbol{b}$ – vector of identified parameters [(1) - longitudinal velocity, (2) - shear velocity in the layer material, (3) - layer density, and (4) - layer thickness).

Since the ultimate goal is to determine the mechanical parameters of the LuAG:Ce SCF, the optimization of the parameters for the YAG substrate was carried out first, and then these values were used in the optimization procedure for the LuAG:Ce SCF/YAG:Ce SC epitaxial structure.

The estimation of the optimization procedure for four identified parameters of the film is shown in Fig. 5.8. The red circle shows the area of convergence of the parameters that were originally set in a certain area of assumed values.

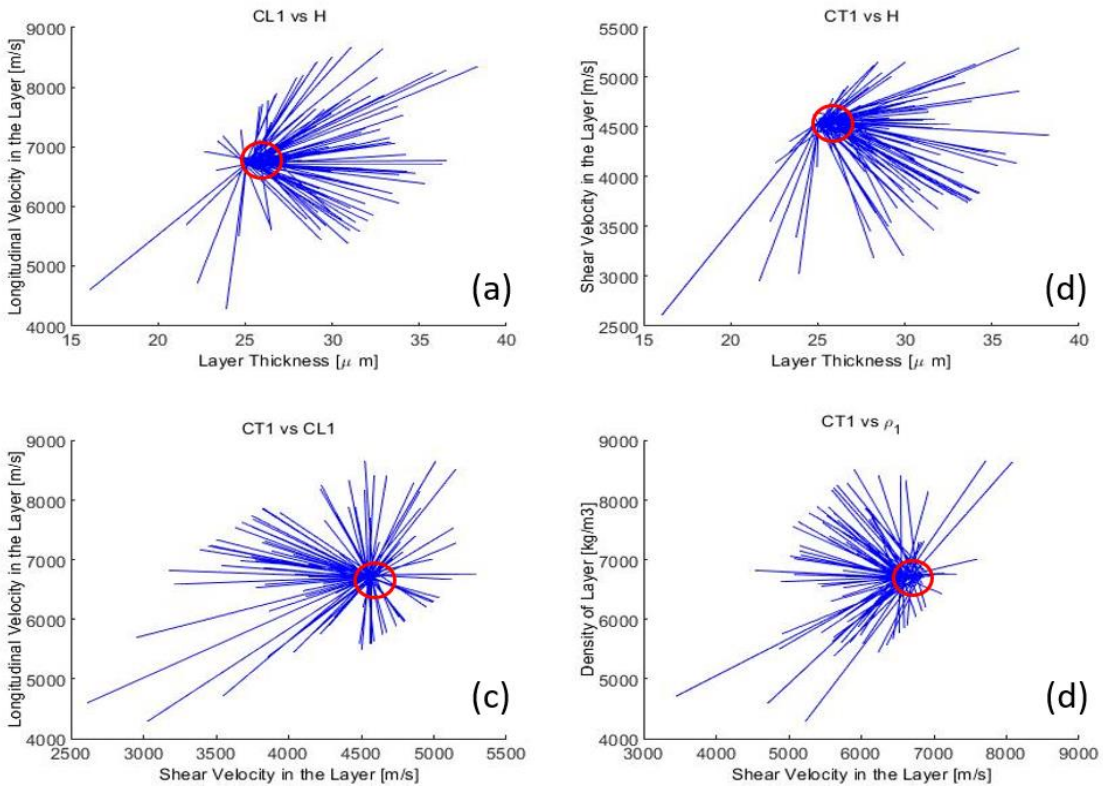

Fig. 5.8 The estimation of optimization procedure: (a) - longitudinal velocity depends on layer thickness, (b) - shear velocity depends on layer thickness, (c) - longitudinal velocity depends on shear velocity, (d) - density of layer depends on shear velocity.

Based on the minimum, optimal and maximum values of the parameters obtained from the optimization procedure, three dispersion curves for LuAG:Ce SCF/YAG:Ce SC epitaxial structure were plotted together with the experimental values observed for B1 and B2 modes (Fig 5.9).

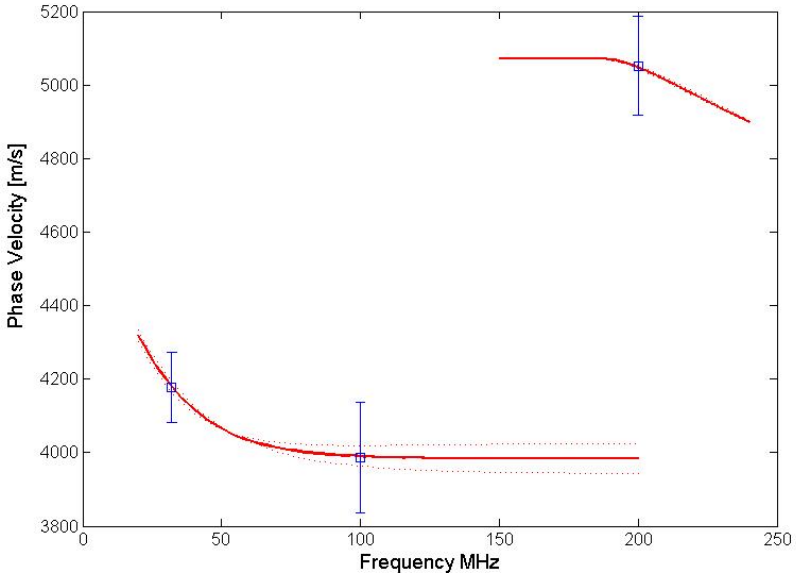

Fig.5.9 Dispersion curves for an LuAG:Ce SCF/YAG:Ce SCepitaxial structure. The dotted line shows the dependence for the minimum and maximum values of the parameters, the solid line shows the optimal curve.

Based on the values of the four identified parameters obtained from the optimization procedure, using Eq. 5.2, it is possible to obtain the values of the main mechanical parameters of the LuAG:Ce SCF, the minimum optimal and maximum values of which are summarized in Table 5.

$$\lambda = \rho(c_L^{l\,2} - 2c_{SH}^{l\,2})$$
$$\mu = \rho c_{SH}^{l\,2}$$
$$E = \frac{\mu(3\lambda + 2\mu)}{\lambda + \mu}$$
$$\nu = \frac{\lambda}{2(\lambda + \mu)} \qquad (5.2).$$
$$c_{11} = 2\mu + \lambda$$
$$c_{12} = \lambda$$
$$c_{44} = \mu$$

Table 5.4**.** Mechanical properties of LuAG:Ce film obtained from optimization procedure. E-Young modulus, ν - Poisson ratio.

Parameter	**Minimum value**	**Optimal value**	**Maximum value**
E, [GPa]	278	290	302
ν	0.22	0.23	0.24
Film Thickness [μm]	21	22	23
Film Density [kg/m^3]	6650	6799	6948

To the present, the literature remains devoid of information concerning the mechanical properties of LuAG:Ce in the SCF form. Table 5.5 shows the values for LuAG in single-crystal and ceramic form [116-118], which could be found in the literature in comparison to optimal values obtained for LuAG:Ce SCF. As can be seen from Table 5.5, the mechanical properties of crystals are approximately the same, while ceramics have slightly lower values, which is explained by the of presence significant content of air porous in the ceramic. *The density value for LuAG film (6799 ± 149 kg/m^3) slightly exceeds the literature values for single crystals.* Such difference can be explained by the large concentration of Lu_{Al} antisite defects in the LuAG crystals, grown from the high-temperature melt and non-stochiometric composition $Lu_3Lu_xAl_{5-x}O_{12}$ of these crystals, where x=0.024 [23].

Table 5.5. Mechanical properties of LuAG bulk crystal and ceramic.

Source	**C_{11}**	**C_{44}**	**E, [GPa]**	**ν**	**ρ, [g/cm^3]**
M. J. Weber et al. [116] values for bulk crystal	339	113	282.7	0.251	6.71
P.D. Dragic et al. [117] values for bulk crystal	342	115	286.7	0.246	6.71
Fu et al. [118] values for LuAG:Yb ceramic	-	-	275		6.65
Our results	**320**	**122**	**290**	**0.23**	**6.8**

The values of Young's modulus and Poisson's coefficient are in line with literature values, but it's important to note that direct comparisons cannot be made with materials in different crystalline forms. It's worth emphasizing once more that there is currently no existing literature that specifically investigates the mechanical properties of garnet SCFs. It's crucial to recognize that the low-temperature melt growth technique results in a minimal concentration of defects in these materials, distinguishing them from counterparts in different crystalline forms. Consequently, we have successfully determined the elastic properties of LuAG:Ce SCF for the first time.

Conclusion to Chapter 5

The measurements using acoustic microscopy were conducted to determine the phase velocity of acoustic surface waves on YAG:Ce crystalline substrate and the LuAG:Ce SCF/YAG:Ce SC epitaxial structure. The resultant phase velocities at distinct excitation frequencies for the YAG:Ce substrate are very close (~4600 m/s) and weakly depend on the frequency of the exciting wave. However, the surface acoustic waves in epitaxial structure exhibit a dispersive nature, meaning that their phase velocity depends on their frequency. This dispersion is a consequence of the complex interaction of the surface wave with the layered structure of the material.

This chapter delves also into the problem of harmonic wave propagation in substrate and film/substrate structures, with a focus on the numerical solution of the proposed models regarding phase velocity. A significant aspect of the discussion revolves around the influence of the upper half-space, particularly when it is occupied by water or air. It is concluded that the presence of water or air has a negligible effect on wave velocity in the substrate, leading to the use of a simplified model with air in the upper half-space for further analysis. A specific optimization sequence is described, starting with the optimization of parameters for the YAG substrate. The values obtained in this initial step are then utilized in the optimization procedure for the LuAG:Ce SCF/YAG:Ce SC epitaxial structure. Experimental results, obtained through ultrasonic microscopy, were compared with the dispersion curves numerically calculated for the simplified model. This comparison reveals a high degree of agreement in the low-frequency region, with slight deviations at higher frequencies, possibly attributed to experimental errors.

The optimization procedure for extracting material properties illustrates its practical implementation in analyzing the LuAG:Ce SCF/YAG:Ce SC epitaxial structure and offers valuable insights into the mechanical characteristics of this material. It highlights the unique and pioneering aspect of this research, specifically in uncovering the elastic properties of LuAG:Ce SCF, an area that had remained unexplored in prior literature.

Chapter 6. Single crystalline film converters for WLED

6.1 Structural, luminescence and photoconversion properties of $Lu_3Al_5O_{12}$:Ce single crystalline film phosphors for WLED application

The interest in LuAG garnet is rapidly increasing in the last two decades due to its excellent properties such as high shock resistivity, and outstanding chemical, thermal and radiation stability. Nowadays the Ce^{3+} doped LuAG is known mainly as an efficient heavy high response scintillator due to the fast 5d–4f radiation transitions of Ce^{3+} ions with high light yield under excitation of different types of ionizing radiation [119, 23]. Apart from the bulk crystals, grown typically by the conventional Czochralski or modified Bridgman methods [119], and transparent ceramics, produced using the different solid-state reaction methods [120, 121], the SCF of LuAG:Ce garnet were developed as well using LPE [85, 122] and Pulse Laser Deposition (PLD) growth methods [123]. Such films with thickness in the few micrometer range are suitable as a heavy scintillating screen for visualization of X-ray images even with submicron spatial resolution in the micrographic devices working with the traditional X-ray sources and synchrotron radiation [122].

However, LuAG:Ce garnet can be also considered as an excellent temperature stable green phosphor for WLEDs. Furthermore, the quenching temperature for Ce^{3+} in the LuAG host is the highest for garnet with the onset of the quenching above 700 K, with small deviations depending on the material structure, e.g. bulk crystal, SCFs, ceramics, or powders [124]. It is the most ideal choice for green phosphor converters for high-power WLEDs, especially for laser driven lighting [125-127] presupposed the material converter heating even to high (above 350 K) temperatures. Recently it was demonstrated that single crystal phosphors (SCPs), based on $(Y,Lu,Gd)_3Al_5O_{12}$:Ce garnets, are promising candidates to substitute currently used ceramic phosphors, phosphors in the glass (PiS), and powder phosphors in applications for high power WLEDs, laser headlights and laser projectors [52, 64, 127].

Currently, the high temperature melt growth methods (Czochralski or Bridgman) are the most widely used techniques for the production of high-quality LuAG:Ce SCPs for mentioned applications [23]. Nevertheless, the technical features of high-temperature growth of LuAG:Ce SCPs from the melt lead to the presence of intrinsic crystal defects (e.g. antisite defects and oxygen vacancies). Thus, the high cost and complexity of these processes require the search for new suitable solutions.

The SCF of LuAG:Ce garnet, typically prepared by the LPE method from PbO-BaO flux at much lower temperatures, is characterized by higher stoichiometric and structural disorder and lower concentration of intrinsic defects concerning bulk crystal counterparts. Namely, LPE grown LuAG SCFs does not possess any types of antisite defects, where part of the Lu and Ce ions occupy the Al octahedral sites [128, 129]. The application of LuAG:Ce SCFs is hampered due to the lack of a

sufficient red component, such WLEDs have a poor color rendering index CRI of about 60 and a high CCT in the 7000–8000 K range, which limits its application and can harm the human retina. To solve the problem the screen-printing of green LuAG:Ce pc with red $CaSiAlN_3$:Eu phosphor is considered [120]. In principle, the LuAG:Ce SCF can be grown both onto undoped or/and YAG:Ce substrates due to suitable film/substrate misfit below 1% [85]. Therefore, the creation of high-quality LuAG:Ce SCF phosphors is now a highly demanded topic in the development of the next generation of solid-state lighting devices using LPE or other film technologies.

6.11 Structural properties of LuAG:Ce single crystalline film

The diffraction profile of the (880) plane of a LuAG:Ce SCF grown on YAG substrate from the PbO-BaO flux is shown in Fig. 6.1b. XRD proved that only the LuAG phase was identified in film and no peak was assigned to other crystalline phases within the precision of using XRD setup. Moreover, the good quality of LuAG:Ce SCF is confirmed by comparing the XRD peak width Δ of the epitaxial films with that of the SC substrate. Indeed, a very close value of peak width of Δ=0.12° is measured for the LuAG:Ce SCF and YAG SC substrate of 0.115° (Fig.6.1b). The measured lattice constant of the YAG SC substrate was a_s= 12.0063 Å, when the lattice constant of LuAG:Ce SCF was determined as a_f=11.9082 Å. Therefore, the lattice mismatch between the substrate and the film was estimated to be **m** = $(a_{SCF}-a_{sub})/a_{sub}\times 100$ = - 0.82%.

According to the lattice mismatch between the films and the substrates, the LuAG:Ce SCF are presumed to undergo a *tensile epitaxial strain*. The control of the strain is very important for material properties engineering as it can be used for the tuning of their physical properties or the creation of new functionalities in the existing compound. Strain may lead to changes in microstructure, crystal structure, and film composition [98].

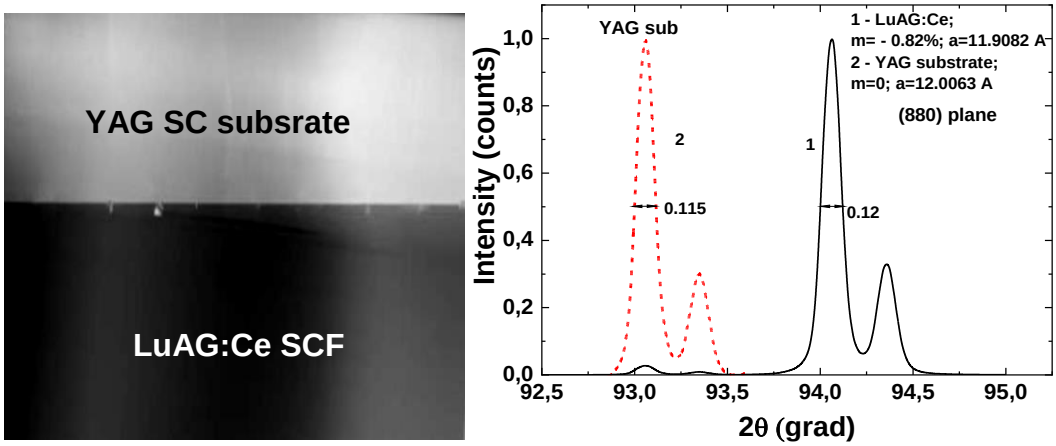

(a) **(b)**

Fig.6.1. (a) specially-prepared and chemically polished cross-section of the LuAG:Ce SC/YAG SC epitaxial structures; (b) XRD pattern of (880) plane of 19 μm thick LuAG:Ce SCF, LPE grown onto (110) oriented YAG substrate.

The small degree of lattice mismatch found by XRD is further locally probed at the film-substrate interface by selected area electron diffraction (SAED). The SAED pattern of the [011] zone axis, as well as the extracted line cut along the <100> direction, is displayed in Fig. 6.2a and Fig. 6.2 b, respectively. In this context, peak splitting could only be observed for higher-order reflections like the -16 0 0 reflection as highlighted with a pink circle in Fig. 6.2a. The extracted lattice mismatch of around - 0.5 %, is notably smaller, but in the range of the value extracted from XRD for the <110> direction (0.82 %). Thus, the local crystal structure at the interface exhibits only subtle changes compared to the one of the "bulk" film.

The local structure of the interface of LuAG:Ce SCF/YAG SC epitaxial structure is further investigated by HR STEM imaging in bright-field (BF), high-angle annular dark-field (HAADF), and dark-field (DF) modes as displayed in Fig. 6.3a, b and c, respectively. In all imaging modes a nanoscale contrast variation towards the LuAG:Ce film directly at the film- substrate interface is

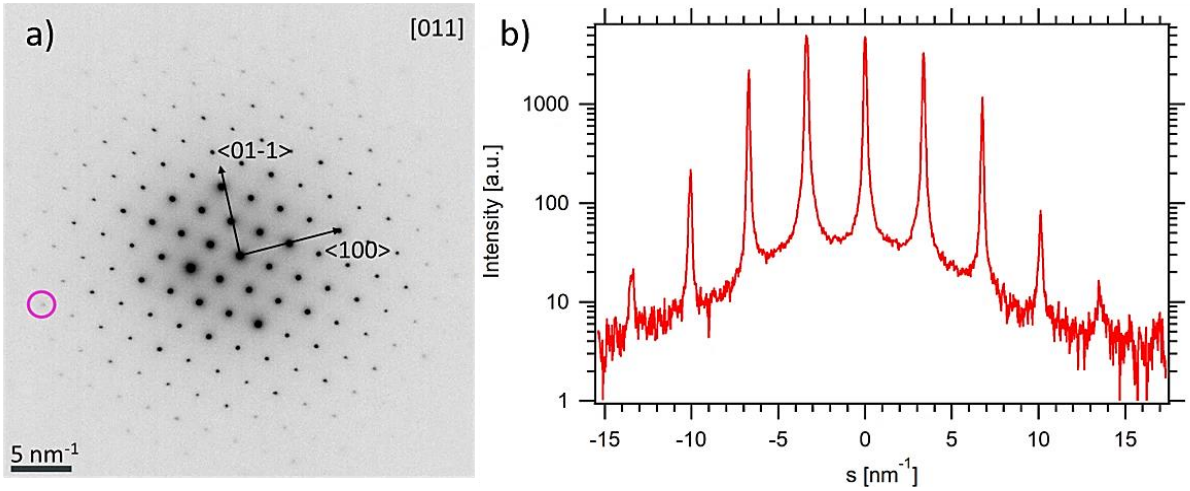

Fig.6.2. (a) SAED pattern of the film-substrate interface taken in [011] zone axis. The pattern intensity is contrast inverted and further, the third root of the intensity is displayed (I(displayed)=I(measured)$^{(-1/3)}$) to reveal weaker higher-order reflection within the first Laue zone. Here, the pink circle highlights the peak splitting of the -16 0 0 reflection. (b) Linecut along the <100> direction in the SAED pattern.

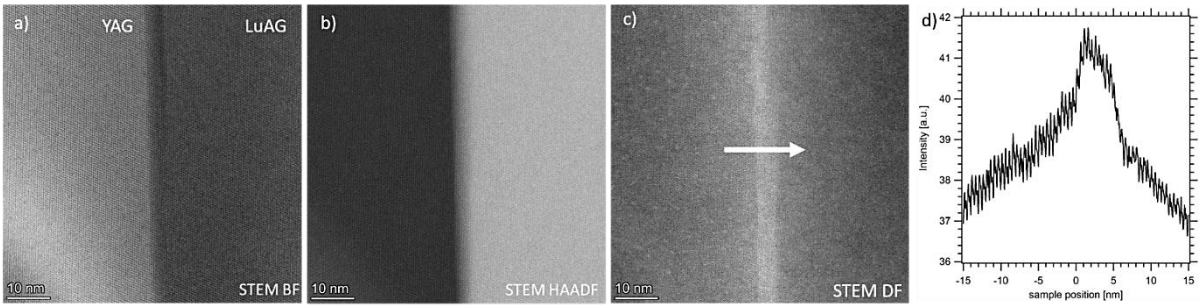

Fig. 6.3 (a-c) HR STEM BF (a), HAADF (b) and DF(c) images of the film-substrate-interface, respectively. (d) Line cut along the white arrow displayed in (c).

present. Whereas HAADF imaging is sensitive to mass contrast, BF and DF imaging are in addition sensitive to strain contrast; thus HR STEM imaging indicates a local nanoscale change in the chemistry accompanied by a build-in strain field at the interface. In this context, a line profile extracted from the STEM DF image across the film-substrate interface as indicated by a white arrow in Fig. 6.3c is displayed in Fig. 6.3d. The profile clearly shows an area bounded by a region of increased deformation with a thickness of ~6 nm directly at the interface. In addition, *no misfit dislocations manifest in the investigated area*. Although the residual misfit is likely compensated by misfit dislocations, the small lattice mismatch implies a low density of dislocations, and thus misfit dislocations can only be coincidently found by HRSTEM [98, 131].

Energy-dispersive X-ray spectroscopy (EDXS) sheds further light on the local chemistry at the interface. In Fig. 6.4a the elemental Lu and Y distribution at the interface is displayed, already indicating a greenish (Y) blurring towards the LuAG:Ce SCF, which is well in line with the mass contrast as well as strain variation found in HR STEM imaging. The effect is quantitatively evaluated by line profiles of the at. % Al, Lu, Y and Ce across the interface as displayed in Fig. 6.4b. Whereas the Lu content rises parallel to the HAADF signal, Y is still present in ~6 nm area towards the LuAG:Ce SCF. This Y segregation into the LuAG:Ce SCF is likely also the source of the local strain, as found by BF and DF imaging. It should also be noted that the Al content is constant at the interface within the error bars, while Ce follows the same pattern as Lu, increasing within the layer from 0 to ~1%.

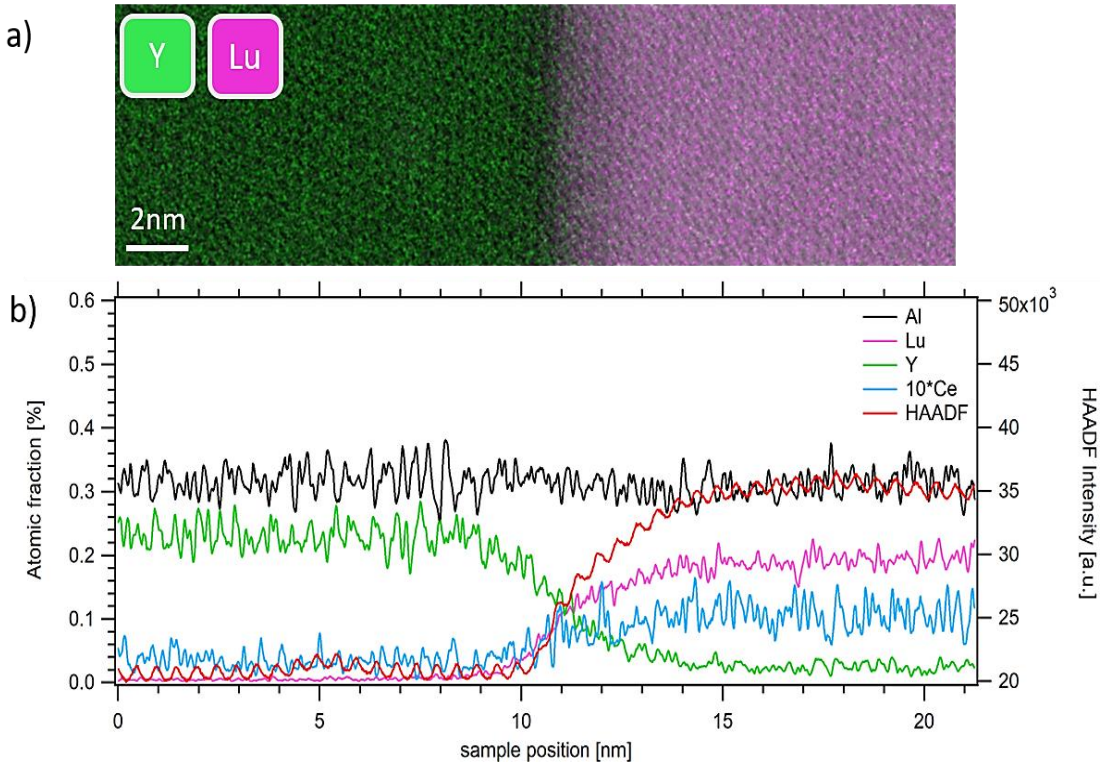

Fig.6.4. (a) EDXS map and extracted elemental distribution across the interface (b). The Ce concentration in at. % is multiplied by a factor of 10 for better visibility.

Therefore, electron microscopy confirms a regular high structural quality interface of LuAG:Ce SCF/YAG SC epitaxial structure with an absence of a high density of dislocations at the interfacial plane. The high structural quality of LuAG:Ce SCF indicates also their key potential for various optoelectronic applications, including scintillation screens for high-resolution microimaging techniques [122] and photoconverters production for WLEDs from large-dimensional epitaxial wafers as well [76].

6.1.2 Mechanical stress LuAG SCF/ YAG SC substrate epitaxial structure

In general, in the case of epitaxial deposition of LuAG SCF onto the YAG substrate with different lattice constants, we expect the presence of residual stresses and material deformations. Simulations of the mechanical state of such a system using the theory of elasticity and the finite element method (see Moridi [132]) show, that if the film thickness is much smaller than the thickness of the substrate (at least 20 times) and there are no dislocation-type defects, the residual stresses are significant, especially in a thin layer, but remain approximately uniform in both the layer and the substrate.

However, the experimental results obtained in this work for the LuAG SCF/YAG SC structure, for the case where the ratio of SCF/substrate thickness exceeds 1/20, prove the existence of significant differences in the lattice constants (0.82%), although no defects were observed (Fig. 6.2). To explain such incompatibility of the above-mentioned theoretical model and the experimental results, the role of a thin, approximately 6 nm *interface transition layers* (TL) should be taken into account. According to the results obtained by the STEM method (Fig.6.4), in this very thin TL, the concentrations of Lu and Y change smoothly and the deformation of the material reaches a much higher level than in the vicinity of the SCF (Fig.6.3d).

It is worth mentioning here that for the solid solution of $Y_{3-x}Lu_xAG$ garnets at $x = 0 \div 3$, Vegard's law was previously experimentally confirmed [10, 133], which shows that the lattice constant varies approximately linearly with the concentration of the Lu or Y cations from the value of a_f=11.9082 Å for the LuAG garnet to the value a_s=12.0063 Å for the YAG garnet. Based on this, it can be assumed that a significant part of the lattice mismatch is reduced in the TL layer of the interface. Due to the very small interface TL thickness of 6 nm (e.g. approximately six lattice constant of $(Y_{3-x}Lu_x)AG$ garnets), in which changes of the chemical composition of garnets take place, it should be assumed that not all mismatching of the lattices disappears in this layer, and the remaining part of the mismatch causes residual stresses and associated deformations. From the approximate measurements of the lattice constant on both sides of the interface, a lattice constant difference value of 0.5% was obtained. That means that the rest of the lattice constant misfit (about of 0.32 %) can be compensated in the main volume of the film. However, further studies of this effect are needed to accurately assess the residual stress in the main part of the SCF.

Fig. 6.5 shows an illustration of the above-discussed two conceptual composite models without the interface TL (Fig.6.5a) and in the presence of such TL (Fig.6.5b) with schematically depicted changes in the lattice constant (a) and residual stresses (σ). The TL model (Fig.6.5b) fits the experimental results much better and shows the existence of significant changes in the lattice constant around the TL and even greater differences in the lattice constant in the main volume of the SCF and the substrate.

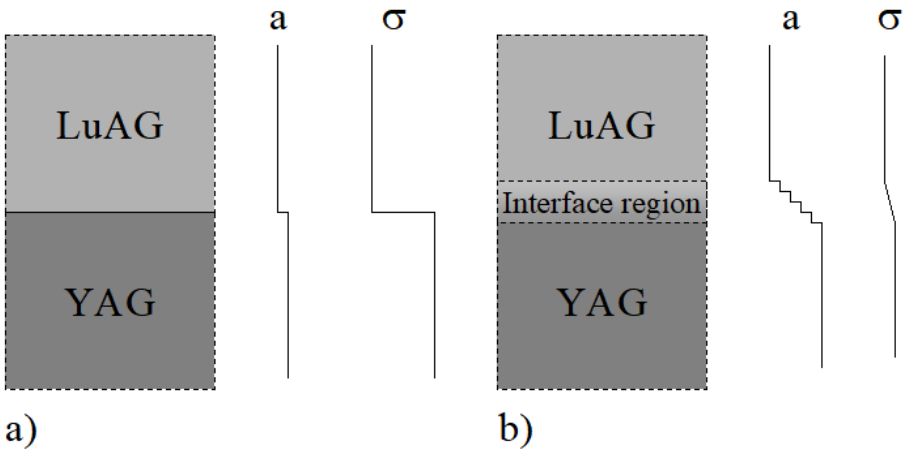

Fig. 6.5 The film-substrate system and schematically presented distributions of the lattice constant - **a** and residual stresses - **σ** in the model without (a) and with the interface zone (b).

6.1.3 Optical, luminescence and photoconversion characteristics of LuAG:Ce SCF/YAG SC substrate structures

The RT absorption spectra of LuAG:Ce SCF/YAG SC epitaxial structure is shown in Fig.6.6. Intense allowed absorption transitions are caused by the allowed $4f \rightarrow 5d_{1,2}$ transitions of Ce^{3+} ions (E_1 and E_2 bands). Other Ce^{3+} absorption bands are located around 230 nm (E3) and related to the 4f-5d (T_{2g}) transitions and partly overlapped by the Pb^{2+} absorption band peaked at 262 nm [23]. The last bands correspond to the absorption of Pb^{2+} flux-related impurity in LuAG:Ce SCF and are caused by the $^1S_0 \rightarrow {}^3P_1$ transitions of these ions [134].

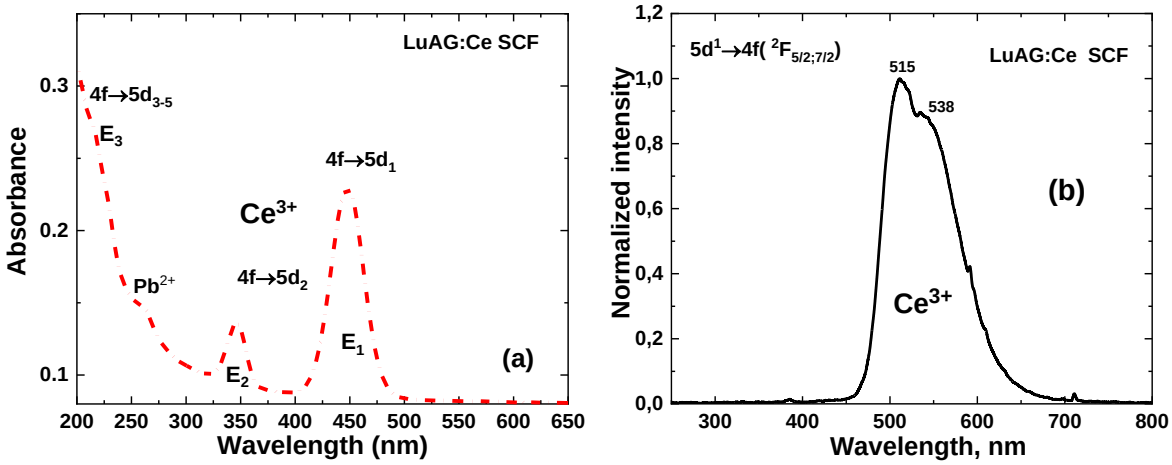

Fig.6.6. Absorption - (a) and CL - (b) spectra of LuAG:Ce SCF, LPE grown onto YAG substrate.

Fig. 6.6b shows the normalized CL spectra of LuAG:Ce SCF under e-beam excitation with the dominant Ce^{3+} luminescence band in the garnet host peaking at 515 nm. It is important to note here the absence of the Ce^{3+} luminescence in other phases as well as the luminescence of the defect-related centers (antisite defects and F^{+} centers), which are usually present in single crystals [128]. The lack of defect-related centers means that the radiative relaxation of the high energy excitation in LuAG:Ce SCF takes place in the final stage only in the form of the radiative Ce^{3+} transitions.

PL emission and excitation spectra of LuAG:Ce SCF are presented in Fig.6.7a and compared with the YAG:Ce SCF counterpart. The spectral peaks in the excitation spectra (Fig. 6.7a) come from the allowed 5d→4f transitions in Ce^{3+} ions and this spectrum shows a close correspondence with the absorption curves in Fig. 6.6a. The excitation band at 448 nm corresponding to $4f(^2F_{5/2}) \rightarrow 5d_1(E_{2g})$ transition, is not perfect but significantly overlaps with the commercial blue LED emitting at 450 nm.

Under excitation at 450 nm in a strong Ce^{3+} excitation band, the broadband emission of LuAG:Ce SCF is ranging from 460 to 660 nm with a maximum at 532 nm. Considering that the ionic radii of Y^{3+} and Lu^{3+} in 8-fold coordination are 1.019 Å and 0.977 Å, respectively, replacing the Y^{3+} cations with the smaller Lu^{3+} ion results in a decrease in the crystal field strength at the dodecahedral sites of the garnet host [135]. As a consequence, a blue shift of the Ce^{3+} emission band to 525 nm is observed for LuAG:Ce SCF in comparison with YAG:Ce counterpart (560 nm).

The $5d_1 \rightarrow 4f$ PL decay kinetic of Ce^{3+} ions was measured under excitation at 440 nm and emission was collected at 520 nm by a single photon counting method. As can be seen from Fig. 6.7b, Ce^{3+} luminescence in LuAG:Ce SCF possesses one exponential PL decay profile with decay time τ=53 ns. This value is typical for Ce^{3+} luminescence in LuAG host [124] and indicates the absence of energy transfer from the Ce^{3+} relaxed excited $5d_1$ state towards any impurity ion or nearby defect state in LuAG:Ce SCFs.

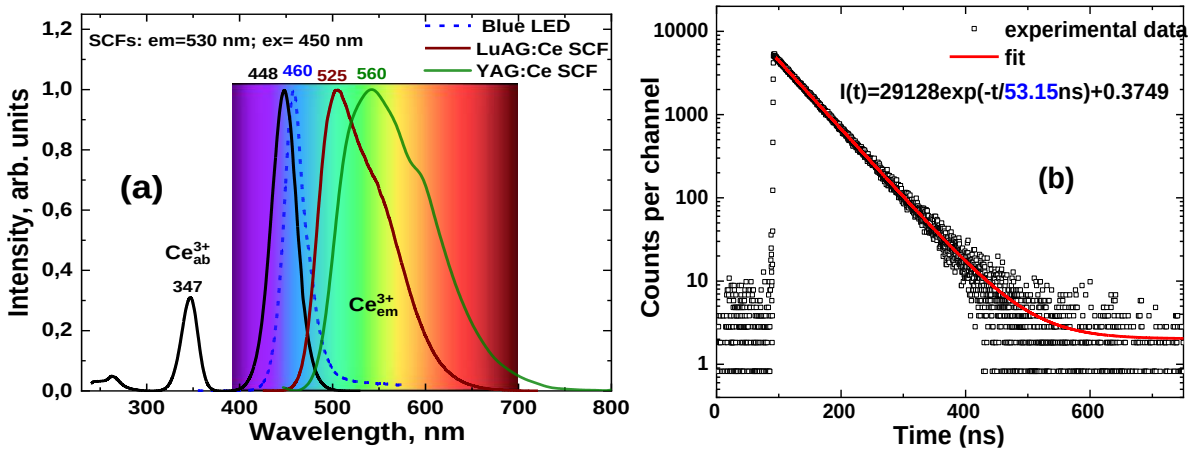

Fig. 6.7. (a) RT PL emission and excitation spectra of LuAG:Ce and YAG:Ce SCFs, registered at the respective wavelength; (b) – RT PL decay kinetic of LuAG:Ce SCF under excitation in Ce^{3+} absorption band at 440 nm.

Finally, the prototypes of pc-WLEDs were fabricated to evaluate the device performance and find the optimal thickness of LuAG:Ce SCF converter. The related spectra of WLEDs fabricated by a surface-mounting of LuAG:Ce SCF converter with different thicknesses (19 μm, 78 μm, 92 μm, 160 μm) onto InGaN blue chip (450 nm excitation, 2.9 V forward-bias voltage, and 20 mA current driving) are shown in Fig. 6.8 and normalized at the maximum of yellow emission. In this luminescence system, two strong spectral bands centered at 450 nm and 525 nm are attributed to the excitation of blue LED and the yellow-green emission of LuAG:Ce SCF, respectively. The green-yellow light intensity of LuAG:Ce SCFs gradually rises with the increasing thickness of the film converter. The luminous efficiency (LE) increases with increasing film thickness, which is explained by a stronger yellow-light emission, while CCT and the CRI decrease due to higher absorption of blue light and stronger emission of yellow light [136]. Fig. 6.8b shows the change of WLED device colors, from cold greenish-white to warm greenish-white with increasing film thickness.

The optical parameters of fabricated pc-WLEDs are shown in Table 6.1. However, such an approach limits the CRI due to the lack of red emission in the LuAG:Ce luminescent spectrum. Meanwhile, LuAG:Ce SCF/YAG SC epitaxial structures can be considered for the creation of advanced composite multilayered converters. Namely, the SCF of green-emitting LuAG:Ce SCF phosphor, can be grown onto YAG:Ce substrates with different Ce^{3+} concentrations and different thicknesses. It will be a very prospective approach for tuning the white light tons from cold white/daylight white (CCT > 7600 K) obtaining for LuAG:Ce SCF converters (Table 1) to neutral white (6000 K > CCT > 3300 K) for expected LuAG:Ce SCF/YAG:Ce SC composites. LuAG:Ce SCF/YAG SC and LuAG:Ce SCF / YAG:Ce SC epitaxial structures can be also used as “substrates” for LPE growth of additional TbAG:Ce SCF converters [126] with the aim of more precisions CCT tuning and CRI improvement.

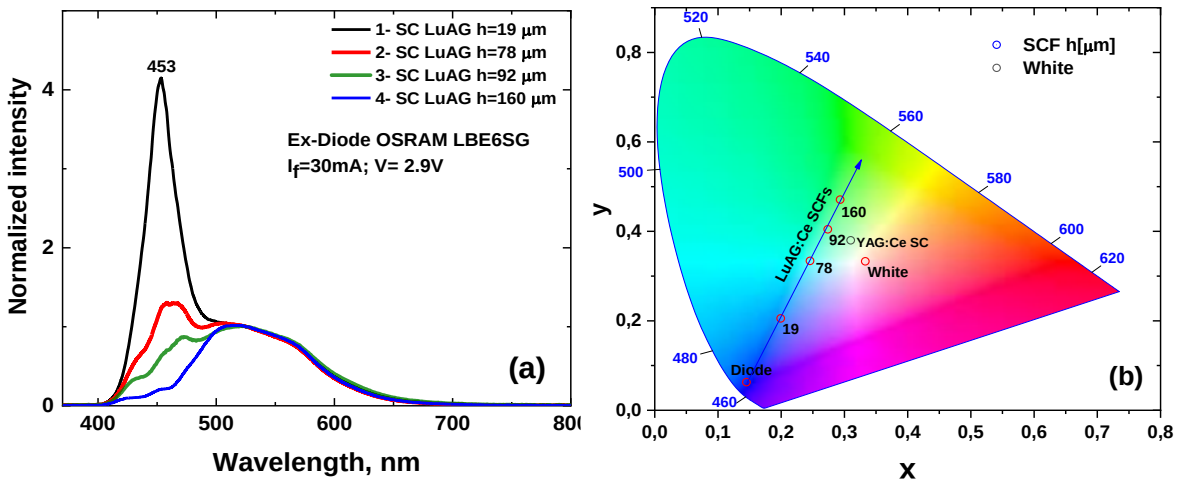

Fig. 6.8. (a) - the spectral performance of WLED prototypes with LuAG:Ce SCFs converter with different thicknesses under blue LED excitation; (b) - CIE-1931 color space chromaticity diagram for these prototypes.

Table 6.1. Photoconversion properties of LuAG:Ce SCFs with total thickness in the (19-160)x2 μm range and reference YAG:Ce crystal with a thickness of 1000 μm.

Samples	h, μm	x	y	CCT	CRI	LE, lm/W
LuAG:Ce SCF	19	0.2818	0.2737	N/A	N/A	79
	78	0.301	0.3063	11630	59	112
	92	0.3351	0.3454	7569	57	129
	160	0.3778	0.4017	4226	44	151
YAG:Ce SC [136]	1000	0.31	0.38	6476	70.9	-

6.2 Structural and photoconversion properties of LPE grown $Tb_3Al_5O_{12}$:Ce single crystalline films for WLED application

Recently, powder and ceramic of TbAG:Ce garnet were considered as promising materials for photoconversion applications [52,137,138]. Compared to the well-known YAG:Ce phosphor, the Ce^{3+} emission spectrum in TbAG:Ce is significantly red-shifted due to the increase of crystal field strength in the dodecahedral sites of the garnet lattice where the Ce ions are localized. This advantage allows for resolving the problem of a high color temperature of YAG:Ce pc based WLEDs and thus better suited for warmer-light indoor illumination. Moreover, the energy transfer from the Tb^{3+} sublattice towards the Ce^{3+} activator significantly enhances the luminescence performance of the TbAG:Ce phosphor for WLEDs [81,139-142]. However, according to the Al_2O_3-Tb_2O_3 phase diagram, the $Tb_3Al_5O_{12}$ melts incongruently and it is difficult to grow a high-quality and large-size bulk TbAG:Ce crystal by Czochralski (Cz) technique which is a great barrier for its practical applications [143]. Meanwhile, in a few reports, the admixing of Lu^{3+} or Yb^{3+} ions in the TbAG matrix allows growing congruently melting $Tb_{3-x}Lu_xAl_5O_{12}$ or $Tb_{3-x}Yb_xA_5O_{12}$ crystals by micro pulling down and Cz methods [77, 144].

Meanwhile, the single crystalline $Tb_3Al_5O_{12}$ matrix can be fabricated in the pure garnet phase using low-temperature synthesis methods such as LPE crystallization [78]. The LPE technique is a versatile method for the production of SCFs with thicknesses in the range of several micrometers even up to 200 micrometers for different optoelectronic applications [145, 75]. Namely, such SCFs could be grown onto a single crystal substrate with a diameter of about a few inches and can be cut into converters with demanded size. In addition to the above-mentioned advantages, further benefits of such WLEDs will be a higher mechanical, chemical, and temperature resistance in comparison to the conventional Volume-Casting-Conversion design products.

Nowadays only a few works in the literature considered the use of epitaxially grown film phosphors for pc-WLED. The pioneering work in this field was carried out by Kundaliya et al. [9], who proposed WLED convectors produced by epitaxial depositing of YAG:Ce and LuAG:Ce film phosphors onto a YAG and GGG substrates using PLD method. However, due to the specific

manufacturing procedure of PLD, the conversion efficacy of these films is very low due to their small film thickness and low structural quality. Recently Zorenko et al. [78,86,146] reported the successful quasy-homoepitaxial growth of TbAG:Ce SCFs with thickness in the tens microns range onto YAG substrates using LPE method. The crucial question is to confirm the high crystal quality of the LPE grown TbAG:Ce SCFs and to demonstrate the advantages of the TbAG:Ce film converters in comparison with the standard YAG:Ce based analogs.

This part of the work is devoted to the results of a complementary study of the structural, luminescence, and photoconversion properties of LPE grown Ce^{3+} doped TbAG SCFs in light of their possible application as blue-to-yellow-converter in WLEDs.

6.2.1 Structural properties of TbAG:Ce single crystalline films

XRD patterns of the TbAG:Ce SCF, grown onto YAG substrate, are shown in Fig.6.9. Besides a TbAG phase, no other crystalline phases were identified in the SCFs. The lattice constants for TbAG:Ce SCF and YAG substrate are equal to 12.076 Å and 12.011 Å, respectively. Therefore, the misfit value was estimated to be equal to $m= (a_{SCF} - a_{sub})/a_{sub} \times 100 = + 0.53\%$. Moreover, the perfect quality of TbAG:Ce SCF is confirmed by comparing the width Δ of the XRD peak for TbAG:Ce SCF with that for the YAG substrate. Indeed, the same peak widthness of Δ=0.11° is measured for both the TbAG:Ce SCF and YAG substrate (Fig.6.9).

HR STEM measurements of the specially-prepared cross-section of the TbAG:Ce SCF/ YAG SC epitaxial structures reveal the high structural quality of the film-substrate interface (Fig. 6.10 a, b). The very high quality of TbAG:Ce SCFs is connected with the realization of the Frank-der Merve mechanism of film epitaxial growth [147], namely the layer-per-layer repetition of the crystalline structure of high-quality single crystal substrate by the film material.

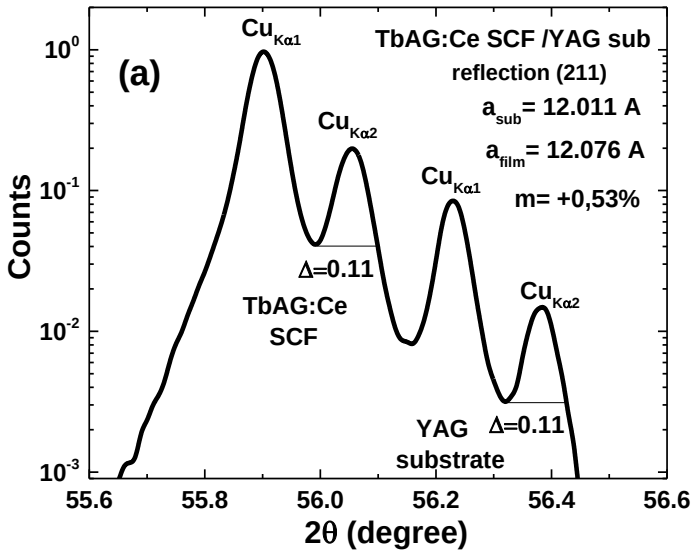

Fig. 6.9. XRD pattern of (211) plane of 19 μm thick TbAG:Ce SCF, grown onto YAG substrate.

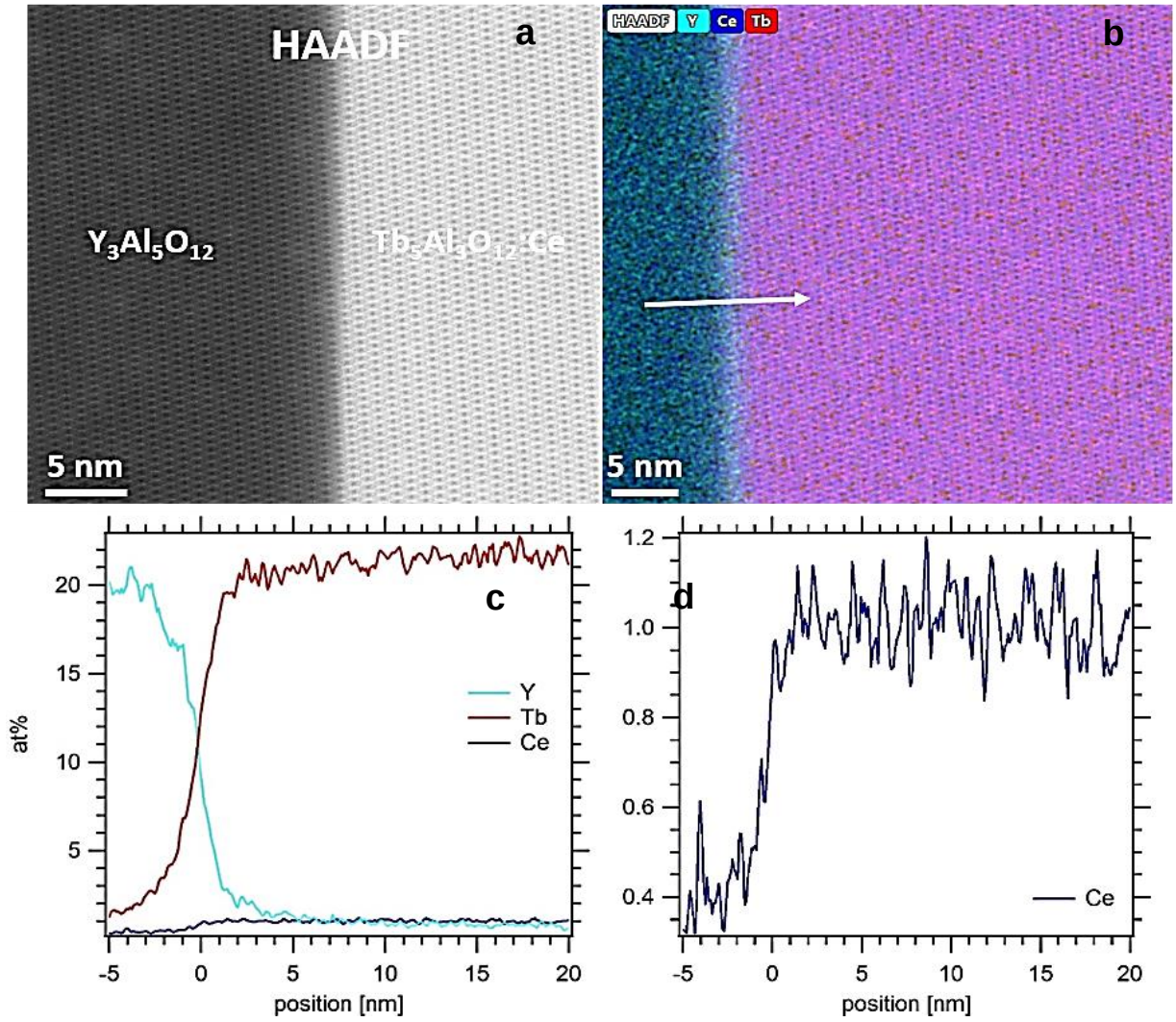

Fig.6.10. High-resolution STEM HAADF (high-angle annular dark field) image (a) and elemental map (b) of the interface TbAG:Ce SCF/YAG SC epitaxial structure. (c, d) - EDX line profile analysis of the cations and dopant content across the interface. The line profile was extracted along the white arrow displayed in (b).

Generally, the term epitaxy refers to the growth of a crystalline layer on (*epi*) the surface of a crystalline substrate, where the crystallographic orientation of the substrate surface imposes a crystalline order (*taxis*) onto the thin film.

At the initial stage of film growth, the film-forming Tb^{3+}, Ce^{3+}, Al^{3+} cations from the melt-solution will occupy the respective positions of the substrate garnet host, suitable for selective localization of the mentioned cations depending on their size and preference in localization. That means that the Tb^{3+} and Ce^{3+} ions will be located exclusively in the largest dodecahedral sites of a garnet host in place of Y^{3+} cations; when Al^{3+} ions from the melt-solution will be located both in the octahedral and tetrahedral sites instead of Al^{3+} cations in the substrate, respectively. Finally, the stoichiometric garnet film compound is formed continuously layer-per-layer during all stages of

epitaxial film growth. Furthermore, such general statements are clearly confirmed by the high-resolution STEM HAADF images of the substrate-film interface (Fig.6.10a), where the perfectly oriented rows of atoms in $Y_3Al_5O_{12}$ garnet substrate followed by the respective perfect oriented rows of $Tb_3Al_5O_{12}$ atoms without any visible breaking of the translation symmetry. HR STEM measurements indicate also the formation of a TL with a thickness of about 5-7 nm between TbAG:Ce SCF and YAG substrate (Figs .6.10a,b). The chemical analysis via energy-dispersive X-ray spectroscopy revealed that TL consists of a mixture of solid solutions between TbAG:Ce and YAG garnets gradually evolving from pure YAG to TbAG:Ce towards the film (Figs.6.10c,d). After equalizing the SCF/ substrate crystalline misfit, the stable growth of TbAG:Ce SCFs is observed.

6.2.2 Absorption, luminescence and photoconversion properties of TbAG:Ce single crystalline films

The investigation of RT CL and PL spectra of TbAG:Ce SCF was performrd on the 19 μm thick sample. For absorption and photoconversion (PC) measurements, the whole sample set of TbAG:Ce SCFs was used to evaluate the required properties.

Absorption spectra of TbAG:Ce SCF in a 190–650 nm range are displayed in Fig.6.11 and show two sets of bands associated with the absorption transitions of Ce^{3+} and Tb^{3+} ions. Two broad absorption bands located around 464 nm and 330 nm are caused by the allowed $4f \rightarrow 5d_{1,2}$ (^2E) transition of the Ce^{3+} ions in the garnet phase. The bands centered at ~239 and ~290 nm belong to the low spin-allowed (LS) $4f \rightarrow 5d_2$ and $4f \rightarrow 5d_1$ absorption transitions of Tb^{3+} ions, respectively. The weak lines in the 375-385 nm range are ascribed to the $^7F_6 \rightarrow {}^5G_6$ absorption transitions of Tb^{3+} cations [148, 149].

Fig. 6.11b shows the CL spectra of TbAG:Ce SCF under e-beam excitation with the dominant Ce^{3+} luminescence band peaking at 577 nm in comparison with Ce^{3+} luminescence in the reference YAG host which is centered around 555 nm. CL spectra of TbAG:Ce SCF demonstrate the absence of the Ce^{3+} luminescence in other phases as well as the luminescence of the defect-related centers

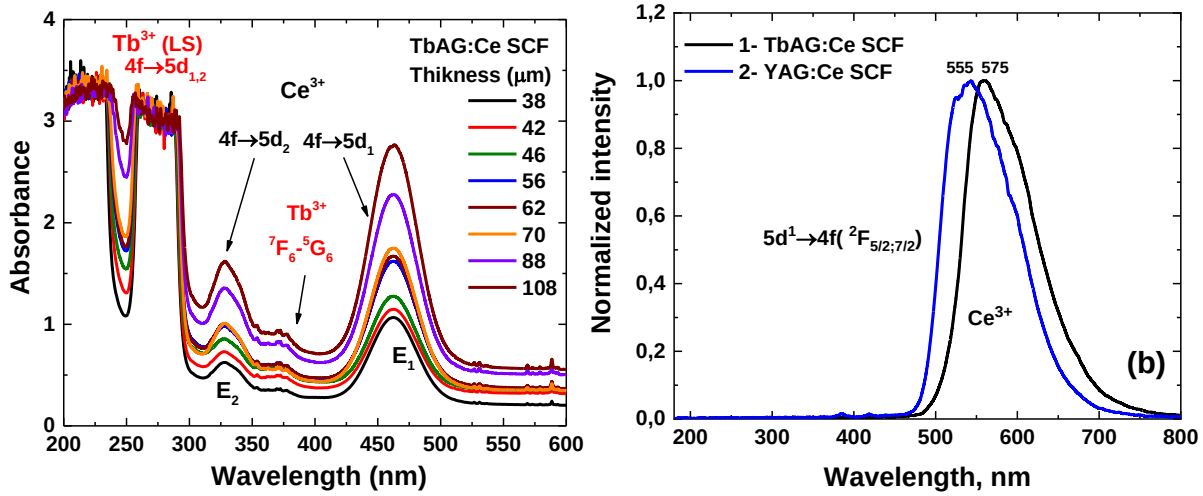

Fig.6.11. RT absorption (a) and CL (b) spectra of TbAG:Ce SCFs.

(antisite defects and F^+ centers). This is due to the very low temperature of SCF crystallization in the range of 950-1025 ^oC [146]. Furthermore, the lack of the mentioned defects is very important for the scintillation applications of TbAG:Ce SCFs [150].

The PL/PLE spectra of TbAG:Ce SCF were measured at RT and are displayed in Fig. 6.12. The PLE spectrum of TbAG:Ce SCF was measured for Ce^{3+} emission at 575 nm and is consistent with their absorption bands (Fig.6.11, curve 1).

The presence of Tb^{3+} related bands in the excitation spectrum of the Ce^{3+} luminescence indicates the efficient $Tb^{3+}\rightarrow Ce^{3+}$ energy transfer, as was reported earlier [151]. Furthermore, the bidirectional $Ce^{3+}\rightarrow Tb^{3+}$ and $Tb^{3+}\rightarrow Ce^{3+}$ energy transfer enhances the Ce^{3+} emission in TbAG:Ce phosphor converter both in high-power and low-power WLEDs application, with UV laser and blue LED excitation, respectively. Moreover, it is worth stressing that the excitation band at 463 nm corresponding to $4f(^2F_{5/2})\rightarrow 5d_1(E_{2g})$ transition overlaps well with the commercial blue LED emission band (Fig. 6.12, curve 3) [33]. The emission spectra of TbAG:Ce excited at 460 nm are mostly identical with the CL spectra and correspond to the overlapped broad yellow emission of the two $5d_1(E_{2g})\rightarrow 4f(^2F_{5/2,}\ ^2F_{7/2})$ transitions of Ce^{3+} ions in the garnet phase. In comparison to the typical 560 nm emission of YAG:Ce SCF (Fig.6.12. curve 3), the TbAG:Ce SCF shows red-shifted emission bands peaked at 575 nm and has more red components in their emissions. This is mainly explained by the increased crystal-field splitting of the Ce^{3+} 5d energy level since the ionic radius of Tb^{3+} (r_{VIII} =1.04 Å) in dodecahedral positions of the garnet host is larger than Y (r_{VIII}=1.019 Å) [20, 78].

For confirmation of the energy transfer processes between Tb^{3+} and Ce^{3+} ions in TbAG:Ce SCF phosphor-converter, the luminescence decay kinetics were measured under UV or blue light

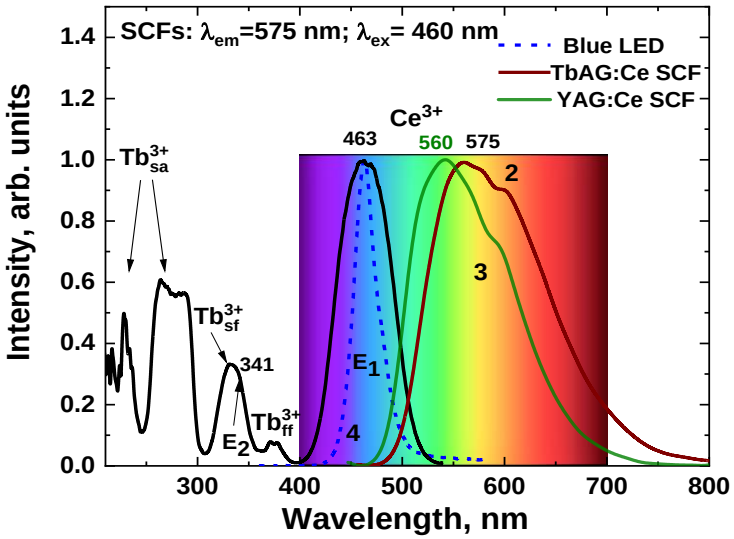

Fig.6.12. RT PLE spectrum (1) of the Ce^{3+} luminescence at 575 nm in TbAG:Ce SCF and PL spectrum of this film excited at 460 nm (2) in comparison with PL spectrum of reference YAG:Ce SCF (3) and radiation of blue diode (4).

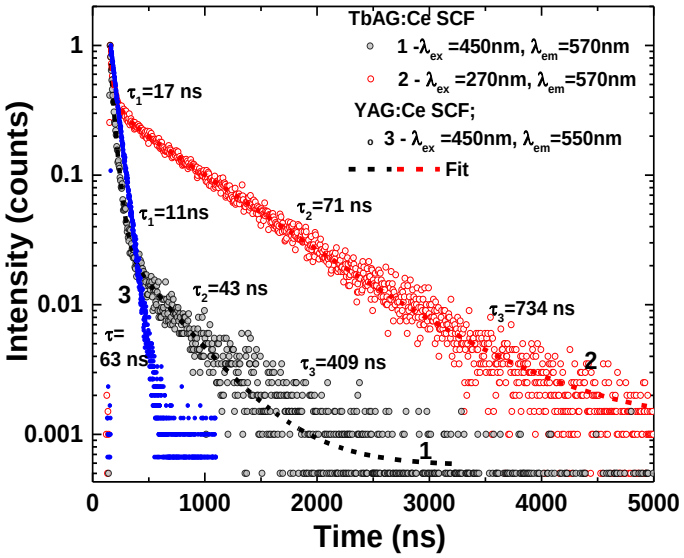

Fig.6.13 Decay kinetics of Ce^{3+} luminescence in TbAG:Ce SCF under excitation in Ce^{3+} (1) and Tb^{3+} (2) absorption bands at the wavelength, indicated in the figure, in comparison with YAG:Ce SCF counterpart (3).

excitation in the absorption bands of Tb^{3+} cations (at 260 nm) and Ce^{3+} ions (at 450 nm), respectively (Fig. 6.13). Both decay curves are fitted with three-exponential functions: $I= \Sigma A_i \exp(-t/\tau_i)+B$ ($i=3$). The decay kinetics of the Ce^{3+} luminescence in TbAG:CeSCF under excitation in Ce^{3+} absorption band at 450 nm consists of accelerated (τ_1=11 ns), fast (τ_2=44 ns), and slow (τ_3=409 ns) decay constants. Such behavior points presence of the complex energy transfer process between Ce^{3+} and Tb^{3+} ions.

Namely, the accelerated and fast decay components, τ_1=11 ns and τ_2=43.5 ns are associated with the radiative transition of Ce^{3+} ions, whereas, the slow decay component with τ_2= 409 ns suggests the energy transfer from Tb^{3+} cations to Ce^{3+} ions (Fig.6.13, curve 1) [86]. Meanwhile, the presence of accelerated and fast decay components in the initial parts of the Ce^{3+} decay kinetic in TbAG:Ce SCF (curve 1) under excitation in Ce^{3+} absorption band at 450 nm in comparison with typical one-exponential decay kinetic of Ce^{3+} ions in YAG:Ce SCF counterpart (curve 3) indicates the presence also of back-energy transfer from Ce^{3+} towards Tb^{3+} ions. Under excitation into Tb^{3+} ions at 270 nm, the accelerated, fast and slow decay components of Ce^{3+} luminescence (τ_1=17 ns, τ_2=43.5 ns and τ_2=734 ns, respectively) are slowed in comparison with respective decay components under selective Ce^{3+} excitation at 450 nm (Fig.6.13, curve 2). We suppose that such slowing decay kinetics of TbAG:Ce SCF may result from the Forster efficient transfer from Tb^{3+} cations to Ce^{3+} ions through nonradiative dipole-dipole coupling and exchange interactions[12, 86].

As a proof-of-concept experiment, the prototypes of pc-WLED were constructed by placing TbAG:Ce SCFs with different thicknesses in the 38-108 μm range directly on the blue LED chip. The generated emission spectrum of such white LEDs demonstrates the dependence of Ce^{3+} emission

intensity on TbAG:Ce SCF thickness. With increasing film thickness, the amount of Ce^{3+} ions, excited by the blue light, strongly increases. It leads to higher absorption of the blue component to the total emission and consequently allows tailoring the blue/yellow radiation ratio [152] (Fig. 6.14a). For a more detailed analysis, the emission of WLEDs is plotted in a CIE diagram Fig. 6.14b.

The red component in the emission spectra with TbAG:Ce SCF is promoted in comparison to the conventional YAG:Ce crystal phosphor converter with a thickness about 1 mm [67, 137]. Thus the white light with higher CRI and CCT in the 7600 - 3700 K range can be obtained upon controlling the thicknesses of TbAG:Ce SCF converters. The luminous efficiency rises with increasing sample thickness up to 132.6lm/W for the 108 μm-thick TbAG:Ce SCF converter. Table 6.2 lists the color coordinates, CCT, CIE and luminous efficiency of WLEDs prototypes based on the developed TbAG:Ce PCs.

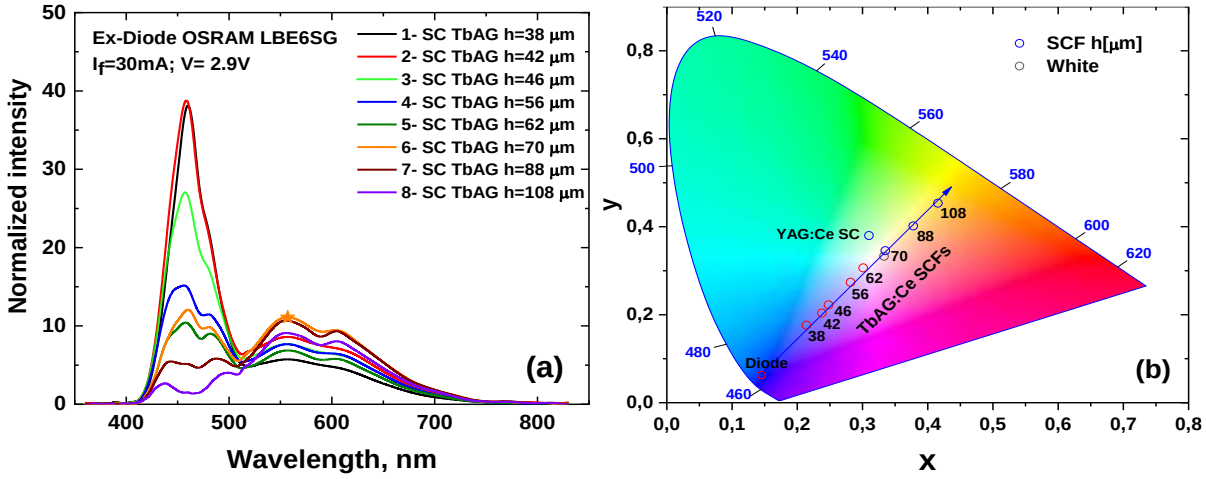

Fig. 6.14. Spectral performance of TbAG:Ce SCFs under blue LED excitation (a), and corresponding color coordinates plotted on CIE chromaticity diagram.

Table 6.2. Photoconversion properties of TbAG:Ce SCFs with total thickness in the 56-108 μm range and reference YAG:Ce crystal with a thickness of 1000 μm.

Samples	h, μm	x	y	CCT	CRI	LER, lm/W
TbAG:Ce SCF	56	0.2818	0.2737	10647	91	93
	62	0.301	0.3063	7516	91	100.4
	70	0.3351	0.3454	5387	86	111
	88	0.3778	0.4017	4226	78	122.5
	108	0.4157	0.4534	3717	73	132.6
YAG:Ce SC [67]	1000	0.31	0.38	6476	70.9	-

6.3 Development of $Tb_{1.5}Gd_{1.5}Al_5O_{12}$:Ce single crystalline film converters for WLED using LPE growth method

This part of the work contains the results of research complementing our previous investigation [76], regarding the photoconversion properties of TbAG:Ce SCF, but with a fundamentally different

approach, which is based on additional co-doping of the TbAG matrix with gadolinium ions. In this study, the structural, optical, luminescent, and photoconversion properties of novel $Tb_{1.5}Gd_{1.5}Al_5O_{12}$:Ce (TbGdAG:Ce) SCF color converters, are studied by varying film thicknesses in 45-83 μm range.

6.3.1 Structural properties of TbGdAG:Ce single crystalline films

The XRD pattern of a 6 μm thick $Tb_{1.5}Gd_{1.5}$AG:Ce SCF test sample is presented in Fig. 6.15. Such a test sample with such a small thickness is used for the verification of single crystallinity and successful crystallization of the films of the selected compound onto YAG substrate before the growth of the main set of samples with the higher thickness (up to 100 μm) was performed. On the other hand, the small thickness of the tested sample (in the order of a few μm) is also justified by the high absorption of X-rays of the tested garnet matrixes; therefore the intensity of reflections from the YAG substrate strongly decreases with increasing the film thickness.

It is clearly seen from Fig. 6.15 that diffraction peaks of $Tb_{1.5}Gd_{1.5}$AG:Ce SCF almost coincide with a slight deviation in the narrow 2θ range towards the smaller side in comparison with YAG substrate. The calculated from XRD patterns lattice parameters of $Tb_{1.5}Gd_{1.5}$AG:Ce film and YAG substrates were 12.0788 Å and 12.001 Å, respectively. The estimated lattice misfit m= $(a_{film} - a_{sub})/a_{sub} \times 100\%$) between the film and substrate was + 0.65%. The halfwidth of 880 diffraction peak originating from the epitaxial film is 13 ang. s, is comparable to that of the single crystal substrate (12 ang. s) demonstrating the film's excellent crystallographic quality and the lack of any additional second phases.

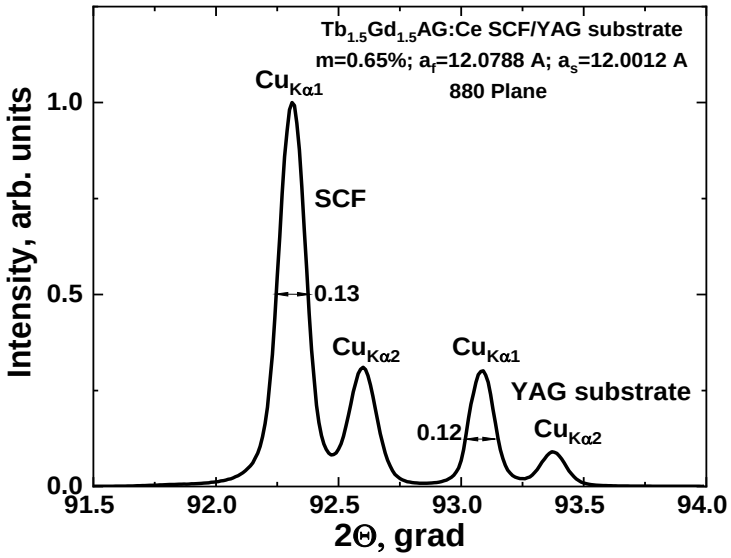

Fig. 6.15. XRD pattern of 880 plane of 6 μm thick $Tb_{1.5}Gd_{1.5}$AG:Ce SCF grown onto (110) oriented YAG substrate.

6.3.2 Absorption and photoluminescence properties of $Tb_{1.5}Gd_{1.5}$AG:Ce SCFs

The RT absorption spectra of $Tb_{1.5}Gd_{1.5}$AG:Ce SCF/YAG SC epitaxial structures in the 200-800 nm range are shown in Figure 6.16. Generally, the absorption bands of Ce^{3+} ions in the

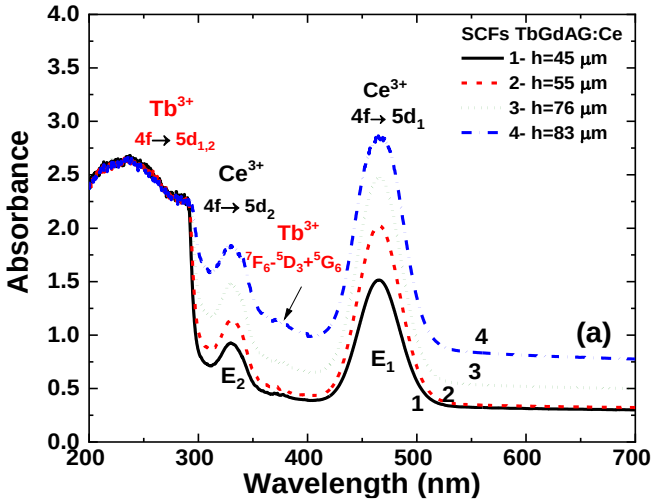

Fig. 6.16. RT absorption spectra of $Tb_{1.5}Gd_{1.5}AG$:Ce SCF/YAG SC converters with different SCF thicknesses.

$Tb_{1.5}Gd_{1.5}AG$:Ce lattice can be detected at 330 and 465 nm corresponding to the $4f \rightarrow 5d_1$ transitions [153]. The absence of Ce^{3+} absorption band near 230 nm, related to the $4f \rightarrow 5d_{3\text{-}4}$ transitions, may result from the strong absorption of Tb^{3+} ions in the shorter wavelength range that covers the nearby absorption bands of Ce^{3+} ions. In addition, the absorption spectra contain sets of bands belonging to the transitions of Tb^{3+} and Gd^{3+} ions. Namely, the bands centered around ~224 and ~270 nm belong to the low spin-allowed (LS) $4f \rightarrow 5d_2$ and $4f \rightarrow 5d_1$ absorption transitions of Tb^{3+} ions. The last band is strongly overlapped with the bands peaked at 275 nm corresponding to the $4f \rightarrow 4f$ Gd^{3+} transitions. The weak line centered at 373 nm is ascribed to the $^7F_6 \rightarrow {}^5D_3{+}{}^5G_6$ absorption transitions of Tb^{3+} cations [127]. Minor absorption bands peaked in the 313-317 nm range, are related to the $4f \rightarrow 4f$ Gd^{3+} transitions and overlapped with the bands related to the $4f \rightarrow 5d$ (HS) transitions of Tb^{3+} ions.

The PL/PLE spectra measured at RT are shown in Fig. 6.17**.** The PLE spectrum of $Tb_{1.5}Gd_{1.5}AG$:Ce SCF (55μm) was measured for Ce^{3+} emission at 580 nm and is consistent with their absorption bands (Fig. 6.16). The presence of the Tb^{3+} and Gd^{3+} related bands in the excitation spectrum of the Ce^{3+} luminescence indicates the efficient $Gd^{3+} \rightarrow Ce^{3+}$ and $Tb^{3+} \rightarrow Ce^{3+}$ energy transfer processes (Fig. 6.17b), as was reported earlier [12,142,154, 155]. In comparison with other Ce-doped garnet phosphor converters such as YAG:Ce or LuAG:Ce, it can be seen from the PLE spectrum that the Gd^{3+} and Tb^{3+} cations in $Tb_{1.5}Gd_{1.5}AG$:Ce can be used as a sensitizer itself. Energy transfer mechanisms enable excitation of the Ce^{3+} emission in $Tb_{1.5}Gd_{1.5}AG$:Ce phosphor converters for both high-power and low-power WLED applications, with UV laser and blue LED excitation, respectively. It is also important to note that the Ce^{3+} $4f(^2F_{5/2}) \rightarrow 5d_1(E_{2g})$ excitation band in $Tb_{1.5}Gd_{1.5}AG$:Ce host well overlaps with the commercial blue LED emission band at 460 nm (Fig. 6.17**,** curve 4) [156].

The emission spectra of $Tb_{1.5}Gd_{1.5}AG$:Ce SCF excited at 460 nm present broad yellow emission, related to electronic transitions from the first excited state to the two ground state levels

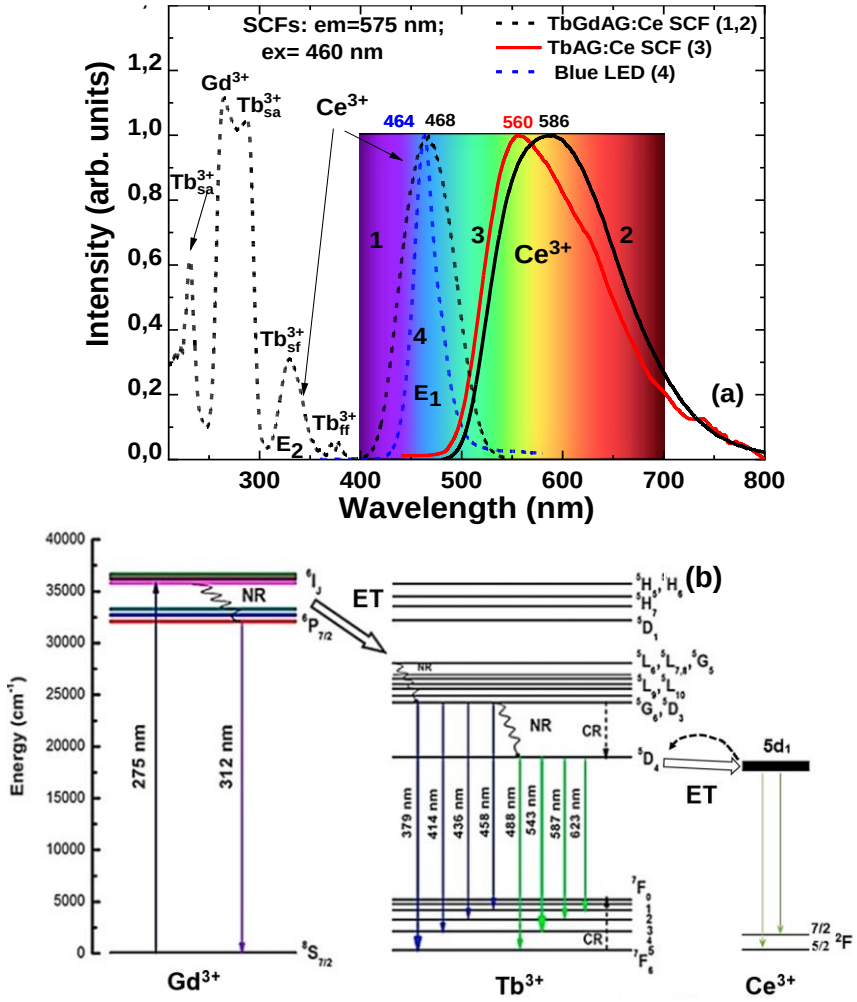

Fig. 6.17. (a) - RT PLE/PL spectra of $Tb_{1.5}Gd_{1.5}AG$:Ce SCF converters (1, 2) in comparison with emission spectra of TbAG:Ce SCF counterpart (3) and blue diode (4). (b) - energy diagram of cascade $Gd^{3+} \rightarrow Tb^{3+} \leftrightarrows Ce^{3+}$ energy transfer. ET – energy transfer; NR - not radiative transitions; CR - cross-relaxation process of Tb^{3+} ions; blue and green arrows – luminescence from $^5D_3$ and $^5D_4$ levels, respectively.

($^2F_{5/2}$, $^2F_{7/2}$)of Ce^{3+} ions. In comparison with TbAG:Ce SCF, the Ce^{3+} emission maxima in TbGAG:Ce SCF is greatly red shifted from 560 nm to 586 nm.

Fig 6.18a shows the example of the decay kinetics curve of Ce^{3+} emission in $Tb_{1.5}Gd_{1.5}AG$:Ce SCF (55μm) at RT under excitation at 450 nm for the Ce^{3+} luminescence at 520 nm related to $5d_1$-4f emission transitions. The decay curve is fitted with the three-exponential approximation according to equation (1) (i=3) with the decay times τ_1=34 ns, τ_2=76 and τ_3=400 ns.

$$I(t) = \sum I_i \exp[-t/\tau_i] + B, \qquad i = 1 \; to \; 3, \qquad (6.1)$$

where I is the luminescence intensity, I_i is the intensity at 0 s, t is the time and τ_i is the decay time, and B is the time-independent background intensity.

Fig. 6.18b shows the intitial part of non-exponential decay kinetics in the hudred μs time range of the Ce^{3+} luminescence at 520 nm excited at 450 nm into 4f-$5d_1$ absorption band. This figure clearly shows all processes related to the *bidirectional* $Ce^{3+} \leftrightarrows Tb^{3+}$ *energy transfer*. The non-exponential

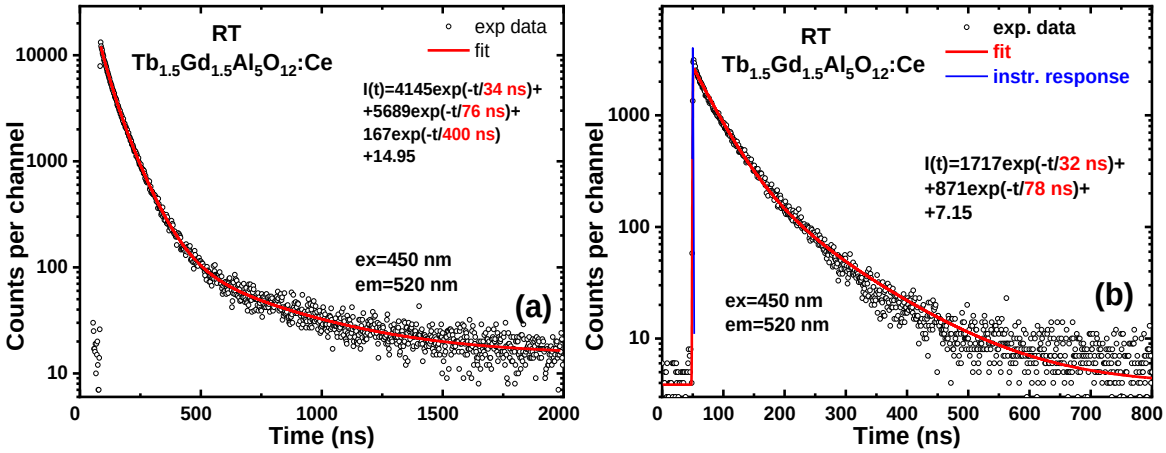

Fig. 6.18. (a) - RT PL decay profilre of Ce^{3+} luminescence at 520 nm in $Tb_{1.5}Gd_{1.5}AG$:Ce SCF, shown in μs time range under excitation at 450 nm. (b) - RT prompt decay curves of the Ce^{3+} luminescence in $Tb_{1.5}Gd_{1.5}AG$:Ce SCF recorded at 520 nm under excitation at 450 nm.

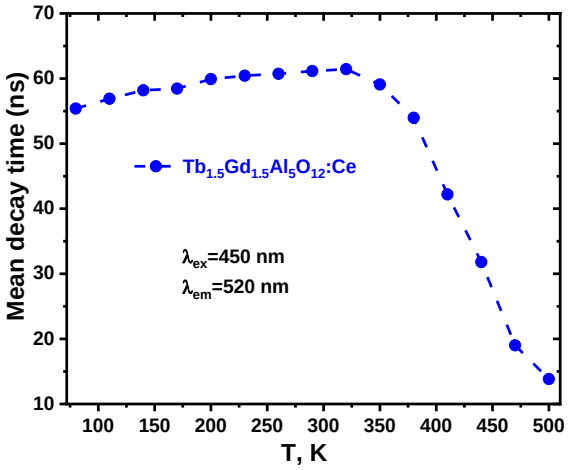

Fig. 6.19. Temperature dependence of the PL mean decay times of Ce^{3+} emission at 520 nm in $Tb_{1.5}Gd_{1.5}AG$:Ce SCF under excitation into 4f→5d_1 absorption band of Ce^{3+} at 450 nm.

accelerated initial part of the decay curve characterized by first τ_1=34 ns and second τ_2=76 ns components (with mean time τ_{mean} around 60 ns) might arise due to the Ce^{3+}→Tb^{3+} backside energy transfer shown in the simplified energy transfer scheme (Fig. 6.17b), which was built based on the experimental results of this work and our previous studies [12, 81]. Moreover, the backside Tb^{3+}→Ce^{3+} resonant energy transfer process can occur via the short-range and long-range electro-static multipolar interactions between the donor and the activator [157]. The third decay component with τ_3=400 ns, is significantly slower than the typical decay time of Ce^{3+} luminescence in garnets [158]. This may indicate that after direct Ce^{3+}→Tb^{3+} excitation, the excitation energy migrates among Tb^{3+} cations and finally is transferred back to the Ce^{3+} ions causing the decelerating of the decay time. The energy migration between Tb^{3+} ions in the garnet host lattice is well known to be extremely effective when the concentration of Tb^{3+} is around 50% [81, 158]. This once again confirms the successful choice of this composition for LPE grown films for photoconversion applications.

Fig. 6.18(b) shows also only prompt decay constants of the Ce^{3+} luminescence at 520 nm under excitation at 450 nm important for the estimation of the thermal stability of the Ce^{3+} luminescence (Fig. 6.19). It is assumed that the slowest component of the decay time with τ_3=400 ns has a rather minor contribution to the overall decay time process (Fig. 6.18(a); hence, this component plays a minor role in the estimation of the thermal stability of the Ce^{3+} luminescence. For this reason, Fig. 6.19 shows the temperature dependence of the decay times of the Ce^{3+} ($5d_1 \rightarrow 4f$) luminescence registered at 520 nm. Due to the non-exponential character of the decay curves, mean decay time, τ_{mean}, is introduced for consideration, defined by Equation 6.2:

$$\tau_{mean} = \frac{\sum A_i \tau_i^2}{\sum A_i \tau_i} \qquad (6.2)$$

where A_i is the amplitude and τ_i is the decay time value of the *i*-th component from the fit.

The mean decay time of the Ce^{3+} emission shows more or less constant values (τ_{mean}=60 ns) to 320K. Above this temperature, the decay significantly accelerates due to thermal quenching and/or thermal ionization [81]. Concluding, $Tb_{1.5}Gd_{1.5}Al_5O_{12}$:Ce SCF shows relatively low thermal stability of the luminescence in comparison with YAG:Ce garnet, but is nevertheless sufficient to be taken into account as a photoconversion material, at least in the ±50°C range.

6.3.3 Photoconversion properties of $Tb_{1.5}Gd_{1.5}$AG:Ce single crystalline films

For confirmation that the conversion properties of $Tb_{1.5}Gd_{1.5}$AG:Ce SCFs is suitable for white solid state lightning application, Fig. 6.20a displays the emission spectra of SCF converters under study in combination with a 460 nm InGaN blue LED.

For convenience in describing the photoconversion spectra are usually divided into blue and yellow components, which belong to the emission of the blue LED and the Ce^{3+} luminescence in the

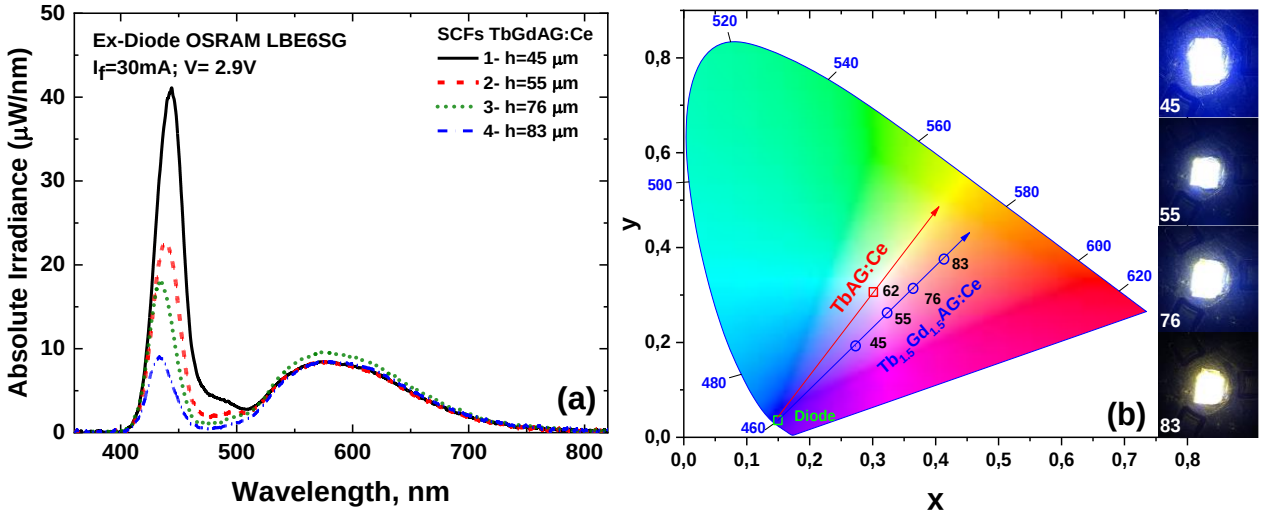

Fig. 6.20. Spectral performance (a) and color coordinates (b) of $Tb_{1.5}Gd_{1.5}$AG:Ce SCFs under blue LED excitation plotted on CIE chromaticity diagram.

garnet matrix, respectively. It is seen that, with an increase in the film thickness, the intensity of the blue component decreases, but the intensity of the yellow component is almost unchanged. This can be explained by the maximum light yield of the yellow component at a chosen Ce^{3+} concentration in the films when excited by a blue LED with a given spectral characteristic. Thus, by increasing the thickness of the SCF converter, it is possible to control only the contribution of the blue component with subsequent adjustment of CCT from 6360 K to 3230 K. It should be noted that the dependence of the photoconversion characteristics on the Ce^{3+} content and the power of the excitation diode is beyond the scope of this study.

For comparative analysis, a trend line for TbAG:Ce SCF photoconverters [76] is shown on the chromaticity color diagram together with the obtained trend for the $Tb_{1.5}Gd_{1.5}$AG:Ce SCF counterparts under study (Fig. 6.20b). The chromaticity color coordinates of the combination of excitation and emission light from $Tb_{1.5}Gd_{1.5}$AG:Ce SCFs shifted from the blue to the yellow-orange range with increasing the thickness of the films. The promotion of the red component is related to the redshift of the Ce^{3+} emission due to the larger split of its 5d energy level and the increased Stokes shifts with the replacement of dodecahedral Tb^{3+} (r_{VIII} =1.040 Å) by the larger Gd^{3+} (r_{VIII} =1.053 Å) ions [51,135]. A detailed comparison of photoconversion properties including the CRI, CCT, and CIE coordinates of reference TbAG:Ce SCFs [76] and $Tb_{1.5}Gd_{1.5}$AG:Ce SCFs is presented in Table 6.3.

It has been shown that a much lower CCT of 6361 K was obtained in $Tb_{1.5}Gd_{1.5}$AG:Ce SCF (55 μm) compared to TbAG SCF (62 μm) at approximately comparable thicknesses and color coordinates around the theoretical white light point.

However, the CRI for the studied samples is lower than that in the case of TbAG:Ce SCF converter [76], since the resulting trend line for $Tb_{1.5}Gd_{1.5}$AG:Ce SCFs does not pass through the theoretical white point with the (0.333,0.333) coordinates and shifts to the red region of the diagram. However, the observed trend of conversion properties of the $Tb_{1.5}Gd_{1.5}Al_5O_{12}$:Ce SCFs is very suitable for the development of the composite color converters on their base using the Ce^{3+} doped YAG:Ce substrate. Such an approach will allow resolving the problem of a high color temperature or low color rendering index of conventional YAG:Ce based white LEDs.

Table 6.3. Comparison of the CRI, CCT, CIE coordinates $Tb_{1.5}Gd_{1.5}$AG:Ce SCFs in comparison with TbAG:Ce SCF counterpart.

Samples	**h,** μm	**x**	**y**	**CCT**	**CRI**
$Tb_{1.5}Gd_{1.5}$AG:Ce	45	0.273	0.193	N/A	N/A
	55	0.323	0.263	6361	78
	76	0.314	0.241	3971	73
	83	0.413	0.376	3233	67
TbAG:Ce SCF [76]	91	0.301	0.306	7516	91

Conclusions to Chapter 6

LuAG:Ce SCF/YAG SC converter. The detailed study of structural properties of the LuAG:Ce SCF phosphors grown using the LPE method onto YAG SC substrates was performed using XRD patterns and HR STEM analyses. HR STEM and composition analysis of the cross-section of LuAG:Ce SCF/YAG SC epitaxial structure revealed a film-substrate interface with high structural quality including the formation of a TL with a 6 nm thickness between LuAG:Ce SCF and YAG substrate. The content of this TL changes gradually from YAG substrate with a lattice constant of 12.0063 Å towards LuAG:Ce SCF with a lattice constant of 11.9082 Å. The large misfit between LuAG:Ce SCF and YAG substrate being equal to 0.82% results in the strong stretching of the LuAG:Ce lattice starting from SCF/substrate interface. Furthermore, the relaxation of such mechanical stress towards the main volume of LuAG:Ce SCF can result in the gradual changing of their optical properties.

The optical properties of LuAG:Ce SCFs were characterized using absorption, cathodo- and photoluminescence spectra. The photoconversion properties (LE, CCT and CRI) of LPE grown LuAG:Ce SCF phosphors with different thicknesses in the 19-160 μm range were performed as well under excitation by 460 nm commercial blue LED. The LE of LuAG:Ce SCF phosphors increases while CCT and CRI values decrease with increasing film thickness. The optimal optical performance values in terms of an LE of 129 lm/W, a CCT of 7569 K, and a CRI of 57 are achieved for the 92 μm thick sample. All of the above-mentioned results reveal that LuAG:Ce SCFs are promising candidates for the creation of the temperature stable green emitting crystal converter. Furthermore, the LuAG:Ce SCF converter can be also used as suitable green components in the composite converters for high-power WLEDs, produced using the LPE method.

TbAG:Ce SCF/YAG SC converter. A set of TbAG:Ce SCFs with different thicknesses in the 38-108 μm range and high-performance structural and optical quality were produced by the LPE method onto YAG substrate. The lattice constants for TbAG:Ce SCF and YAG substrate were determined to be 12.076 and 12.011 Å, with the SCF/substrate misfit value m= + 0.53%. Such a large difference between the lattice constants of film and substrate results also in huge mechanical stress on the film-substrate interface which can strongly influence the luminescent properties of the main volume of TbAG:Ce film.

HR STEM images confirmed the very high structural quality of the SCF-substrate interface. HR STEM measurements indicate also the formation of a TL with a thickness of about 5-7 nm between TbAG:Ce SCFs and YAG substrate. Energy-dispersive X-ray spectroscopy content analysis revealed that TL consists of a solid solution between TbAG:Ce and YAG garnets gradually changing from pure YAG garnet in substrate towards TbAG:Ce garnet in the film. The formation of the TL

during the SCF growth allows to reduction a large difference in the garnet lattices and leads to the decrease of SCF/substrate mismatch-related stress.

The absorption and photoluminescence properties of TbAG:Ce SCFs were investigated. Furthermore, the dependence of photoconversion properties on the TbAG:Ce SCF thicknesses were studied to construct the prototypes of efficient warm WLEDs. The systematic variation in the SCF thickness enables tuning the white light tones from cold white/daylight white (CCT > 6000 K) for the 62 μm thick sample to neutral white (6000 K > CCT > 3300 K) for the samples with a thickness in 70-108 μm range. Meanwhile, the CRI values were higher for all TbAG:Ce SCFs compared with reference YAG:Ce single crystal phosphor converters. The highest LE value of 132.6 lm/W was obtained for the 108 μm-thick SCF sample. Therefore, TbAG:Ce SCFs exhibit a large promising potential for a planar phosphor converter in high-power WLEDs and in general for color tuning in solid-state lighting.

$Tb_{1.5}Gd_{1.5}$AG:Ce SCF/YAG SC converter. The SCFs of $Tb_{1.5}Gd_{1.5}$AG:Ce mixed garnets with different thicknesses in the 45-83 μm range were grown using the LPE method using PbO-B_2O_3 based flux onto undoped YAG substrates. The investigation of structural, luminescence, and photoconversion properties (CCC, CRI, and LE) of the mentioned films was performed as well.

It was shown that the developed $Tb_{1.5}Gd_{1.5}$AG:Ce SCFs are responsible for producing white light when directly combined with commercially available blue LEDs. The trend line on the color coordinates diagram was obtained for the first time for the $Tb_{1.5}Gd_{1.5}$AG:Ce SCF converters by the variation of film thickness in the 45-83 μm range. The ideal white color was almost achieved for the SCF converter with a thickness of 55 μm under 455 nm blue LED excitation. Furthermore, the $Tb_{1.5}Gd_{1.5}$AG:Ce converters can be suitable for the development of multilayered composite color converters based on YAG:Ce or other Ce^{3+} doped garnet crystal substrates using the LPE growth method.

Chapter 7. Composite film-crystal converters for WLED

7.1 Composite color converters based on $Tb_3Al_5O_{12}$:Ce single crystalline films and $Y_3Al_5O_{12}$:Ce crystal substrates

In this chapter, we report for the first time on the creation of composite phosphor converters based on the LPE grown TbAG:Ce SCFs and YAG:Ce SC substrates. Such composite converters are responsible for producing white light when directly combined with commercially available LEDs. Herein, the structural, luminescent, and photoconversion properties of three sets of composite TbAG:Ce SCF/YAG:Ce SC color converters with variable film/substrate thickness and Ce^{3+} concentration in substrates are discussed in detail.

7.1.1 Structural properties of TbAG:Ce SCF/YAG:Ce SC composite color converters

From the XRD patterns of this epitaxial structure, the lattice constants of the TbAG:Ce SCF and YAG:Ce substrate have been evaluated as 12.0688 Å and 12.0023 Å, respectively. Therefore, the misfit **m** between the lattice constants of TbAG:Ce SCF and YAG:Ce substrate has been equal to **m=**$(a_{SCF}-a_{sub})/a_{sub}$*100 % = 0.55 % (Fig.7.1b). For investigation of the uniformity of TbAG:Ce SCFs, grown onto YAG:Ce substrates, we have measured also their rocking curves (RC) using a double crystal spectrometer at $Cu_{K\alpha}$ radiation with a silicon monochromator adjusted to (1040) reflection (Fig. 7.1b). Finally, the RCs of the SCF and substrates were compared. As can be seen from Fig. 7.1b, the TbAG:Ce SCF with a thickness of 15 μm shows a significantly larger FWHM of RC peak being equal to 0.049 degrees than that for YAG substrate with Δ= 0.0127 degree.

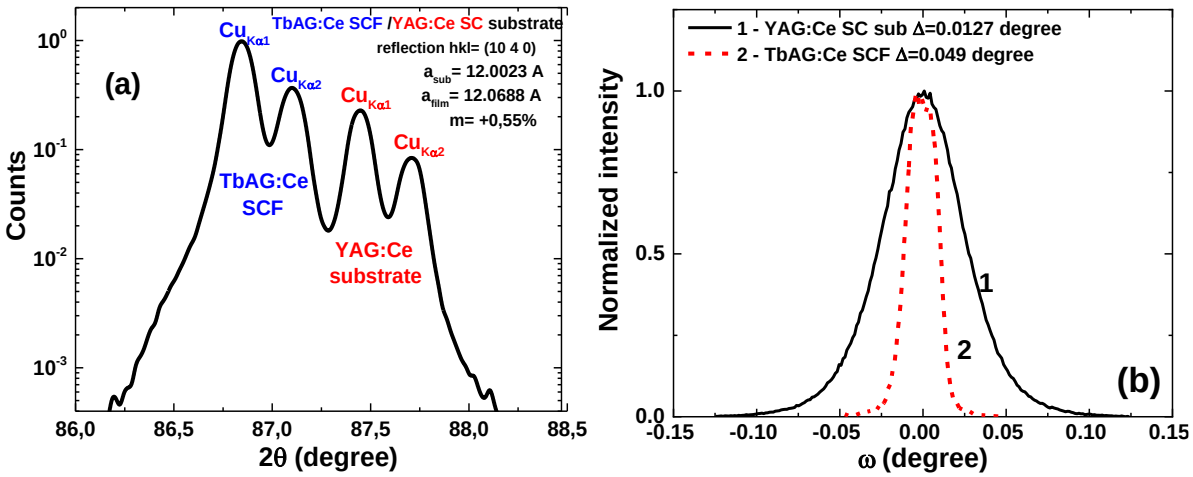

Fig. 7.1. (a) - XRD pattern of the (1040) plane of S2.1 $Tb_3Al_5O_{12}$:Ce SCF/$Y_3Al_5O_{12}$:Ce SC epitaxial structure; (b) - rocking curve of TbAG:Ce SCF (1) and YAG:Ce (2) crystal substrate.

7.1.2 Absorption, luminescence and photoconversion properties of TbAG:Ce SCF / YAG:Ce SC composite color converters

The RT absorption spectra of the YAG:Ce substrates and TbAG:Ce SCF/YAG:Ce SC epitaxial structures are shown in Figs. 7.2a and 7.2b, respectively. The absorption spectrum of YAG:Ce substrate

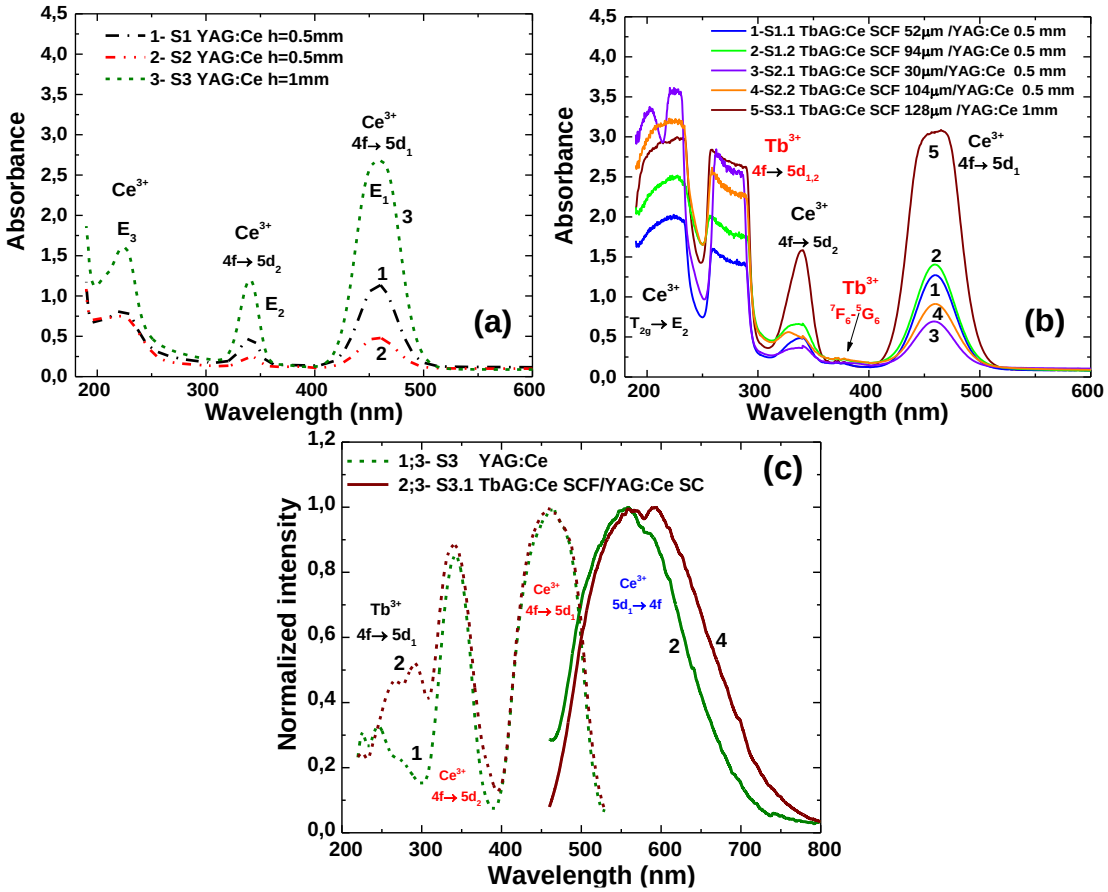

Fig.7.2. (a, b) - RT absorption spectra of YAG:Ce SC substrates (a) and TbAG:Ce SCF/ YAG:Ce SC composite converters (b). (c) - RT PLE spectrum of the Ce^{3+} luminescence at 585 nm and PL spectrum excited at 460 nm of YAG:Ce SC substrate (1, 3) and S3.1 sample of TbAG:Ce SCF/YAG:Ce SC epitaxial structure (2, 4).

(Fig. 7.2a) shows the two main absorption bands centered at ~460 nm (E_1) and ~340 nm (E_2) attributed to the allowed electric dipole transitions in Ce^{3+} ions from 4f (^4F_J) ground state to $5d_{1,2}$(^2E) excited states, respectively. Another Ce^{3+} absorption band (E_3) is located around 230 nm and related to the Ce^{3+} 4f–5d(T_{2g}) transitions [159]. Intensities of all main absorption bands are enhanced with increasing of Ce^{3+} concentration from 0.1 to 0.25 at.% (S2 and S1 samples) and substrate thickness from 0.5 to 1.0 mm (S1, S2 and S3 samples), which is in agreement data presented in [160]. It is obvious that in the case of TbAG:Ce SCF/YAG:Ce SC structure (Fig. 7.2b), the absorption spectra represent the superposition of absorption bands of Ce^{3+} ions in TbAG and YAG hosts. Such an imposition of Ce^{3+} absorption bands originating from both garnet matrices leads to a significant broadening of the main E_1 absorption band of TbAG:Ce SCF/YAG:Ce SC composite, which is an advantage for better fitting with commercially available blue LEDs.

The absorption bands of TbAG:Ce SCF/YAG:Ce SC structure centered at ~239 and ~290 nm belong to the low spin-allowed (LS) 4f→$5d_2$ and 4f→$5d_1$ transitions of Tb^{3+} ions, respectively. The weak line at 373 nm is ascribed to the $^7F_6$→$^5G_6$ absorption transitions of Tb^{3+} cations [141].

The RT PL excitation and emission spectra of YAG:Ce S3 substrate and S3.1 sample of TbAG:Ce SCF/YAG:Ce SC structure are shown in Fig. 7.2c**.** The excitation spectra (dashed lines 1 and 2) were measured at an emission wavelength of 540 nm (S3), 570 nm (S3.1), and are similar to the absorption spectra (Fig.7.2a and 7.2b). The spectra possess the main Ce^{3+} excitation band related to $4f \rightarrow 5d_1$ transitions centered at 465 nm (S3) and 460 nm (S3.1), with a full width at half maximum (FWHM) of 86 nm and 90 nm, respectively. The presence of Tb^{3+} related bands in the excitation spectra of Ce^{3+} emission is associated with an efficient energy transfer (ET) from the matrix (Tb^{3+} cations) to the Ce^{3+} activator and occurs in both directions (from Ce^{3+} to Tb^{3+} and vice versa), for details see previous reports [12, 142, 161]. Such a bidirectional ET enhances the Ce^{3+} emission both in TbAG:Ce SCF and YAG:Ce substrate of the composite color converter under UV or blue LED excitation [149,162].

The Ce^{3+} emission spectrum in TbAG:Ce garnet compared with YAG:Ce counterpart, is significantly shifted from 540 nm to 560 nm [86,138]. The emission redshift is related to increased crystal field splitting and consequently the larger split of 5d energy level of Ce^{3+} ions and the increased Stokes shifts due to the replacement of Y ions (r_{VIII}=1.019 Å) by larger Tb^{3+} (r_{VIII}=1.04 Å) ions in dodecahedral sites of the garnet structure [34,20]. Thus, we observe the redshift of Ce^{3+} emission maxima in the S3.1 sample of TbAG:Ce SCF/YAG:Ce SC composite to 565 and 591 nm in comparison with 559 and 584 nm for YAG:Ce S3 substrate, the FWHM increased from 155 to 182 nm, respectively. This is reflected in the ability to control the photoconversion properties of pc-WLEDs based on composite color converters of this type. Namely, the redshift may greatly improve the CRI of such pc-WLEDs due to the compensation of the red component in the spectrum [163].

As a proof-of-concept experiment, the pc-WLED devices were constructed by placing YAG:Ce SC substrate and TbAG:Ce SCF/YAG:Ce SC composite directly on the blue chip. Fig. 7.3a displays the emission spectra normalized at the maximum of yellow emission of pc-WLEDs under a forward-bias voltage of 2.9 V and a current of 30 mA. The bands around 455 nm are attributed to the emission of LED transmitted through the sample and not absorbed by Ce ions. According to the absorption spectra (Figs. 7.2a and 7.2b), the profile of blue emission, bands varies with the intensities and broadening of absorption bands of YAG:Ce SC substrates and TbAG:Ce SCF/YAG:Ce SC structures, as well as in connection with a strong re-absorption of the blue and green light components [164].

The color coordinates of S2 and S3 samples of YAG:Ce SC substrates with different thicknesses lie in a straight line directed to the yellow area of the diagram. For the S2 and S1 samples of YAG:Ce SC with different Ce concentrations, the straight line connecting their color coordinates will be directed into the yellow-green area of the diagram. Both trends of the color coordinate for variable thicknesses and Ce concentrations in single-crystalline or ceramic YAG:Ce converters are well studied and published (insert in Fig. 7.3b) [164-166].

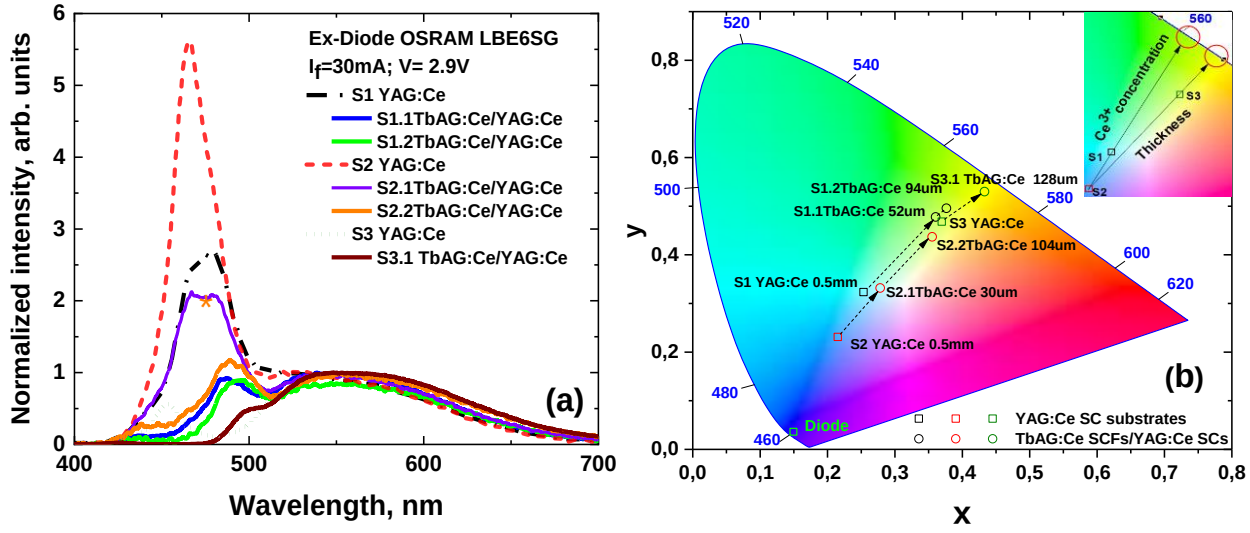

Fig.7.3. (a) The spectral performance of TbAG:Ce SCF/YAG:Ce SC composite color converter under 460 nm blue LED excitation; *-star corresponds to near white spectrum; (b) color coordinates of TbAG:Ce SCF/YAG:Ce SC composite converter in CIE-1931 color space chromaticity diagram under 455 nm blue LED excitation.

The photoconversion parameters of the WLEDs based on TbAG:Ce SCF/YAG:Ce SC structure with various film thicknesses and YAG:Ce substrate thicknesses and doping concentrations are listed in Table 7.1. Crystallization of TbAG:Ce SCFs onto YAG:Ce SC substrates (S1, S2, S3 samples) allows observation of the tilt trend line of composite phosphor conversion to the orange-yellow area. The results of the measurement indicate that LPE grown TbAG:Ce SCFs with a thickness of 30 µm onto S1 substrate allow tuning and significantly improve their photoconversion properties. Namely, the color coordinates of S2.1 sample of composite converter were dramatically shifted from (0.215, 0.231), which is inappropriate for WLEDS, to near white coordinates (0.278, 0.332). The LE and

Table 7.1. Photoconversion properties of YAG:Ce substrates and TbAG:Ce SCF/YAG:Ce SC epitaxial structures.

Sample	Substrate thickness [mm]	Film thickness [µm]	x	y	CCT [K]	CRI	LE [lm/W]
S1 YAG:Ce 0.25 at.% Ce SC	0.5		0.253	0.323	10811	66	104
S1.1 TbAG:Ce SCF/YAG:Ce SC	0.5	52	0.360	0.478	4915	60	144
S1.2 TbAG:Ce SCF/YAG:Ce SC	0.5	94	0.376	0.495	4648	59	145
S2 YAG:Ce 0.1 at.% Ce SC	0.5		0.215	0.231	N/A	N/A	83
S2.1 TbAG:Ce SCF /YAG:Ce SC	**0.5**	**30**	**0.278**	**0.332**	**8532**	**73**	**108**
S2.2 TbAG:Ce SCF /YAG:Ce SC	**0.5**	**104**	**0.355**	**0.437**	**4944**	**70**	**130**
S3 YAG:Ce 0.1 at.% Ce SC	1		0.369	0.468	4702	60	155
S3.1 TbAG:Ce SCF /YAG:Ce SC	1	128	0.433	0.530	3835	47	157

CCT are significantly enhanced with increasing the film and substrate thicknesses and substrate doping concentration, mainly due to the higher ratio of blue absorbed and yellow emitted light. In the case of S1.1, S1.2, S2.2 samples of composite converters, the yellow to blue ratio increases and the resulting luminescence color tends towards warm white and finally yellow light for S3.1 sample, with the expected decrease of CRI.

7.2 Composite color converters based on $Tb_{1.5}Gd_{1.5}Al_5O_{12}$:Ce single crystalline films and $Y_3Al_5O_{12}$:Ce crystal substrates

The following stage in the developed composite color converters is connected with the application of the SCF converters based on the mixed Tb^{3+} and Gd^{3+} containing garnet compounds. Namely, the combination of the emission coming from $Tb_{3-x}Gd_xAl_5O_{12}$ SCF and YAG:Ce crystal part of such composite color converter under blue or UV LED excitation, allows obtaining a wide emission spectrum of WLEDs, similar to the spectrum of natural white light with enhanced luminous efficacy in comparison with standard photoconverters.

Recently the luminescent and scintillation properties of the $Tb_{3-x}Gd_xAl_5O_{12}$ SCFs, LPE grown onto undoped YAG substrates, were investigated [93, 155]. However, the possibility of application of such films as WLED phosphor-converters strongly needs experimental confirmation. In this part, we report for the first time on the creation of composite color converters based on LPE grown SCFs of $Tb_{1.5}Gd_{1.5}Al_5O_{12}$:Ce (TGdAG:Ce) and YAG:Ce SC substrate. The results of a study of the structural, luminescence and photoconversion properties of three sets of $Tb_{1.5}Gd_{1.5}$AG:Ce SCF/YAG:Ce SC composite color converters with variable film thickness and Ce^{3+} content in substrates (0.1; 0.15; 0.5 at. %) are presented in detail in this Chapter.

7.2.1 Structural properties of $Tb_{1.5}Gd_{1.5}$AG:Ce SCF/YAG:Ce SC substrate composite color converters

The diffraction pattern of TGAG:Ce SCF/YAG:Ce SC substrate composite structure is shown in Fig.7.4. The XRD identified pure garnet phase both in film and substrate without any other crystalline phases, within the precision of XRD setup. The experimentally obtained lattice constant of the YAG:Ce substrate was a_{sub}=12.0072 Å, and the lattice constant of TbGAG:Ce SCF was determined as a_{film}=12.0906 Å. According to the measurement results, the lattice mismatch between the substrate and the film was estimated to be m= $(a_{film} - a_{sub})/a_{sub} \times 100 = +0.69\%$. The higher lattice constant of the films is associated with larger sizes of ionic radius of Gd^{3+}(r_{VIII}=1.053 Å) and Tb^{3+} (r_{VIII} =1.040 Å) cations in dodecahedral positions of the garnet host in comparison with the size of Y^{3+} (r_{VIII}=1.019 Å) ions [135].

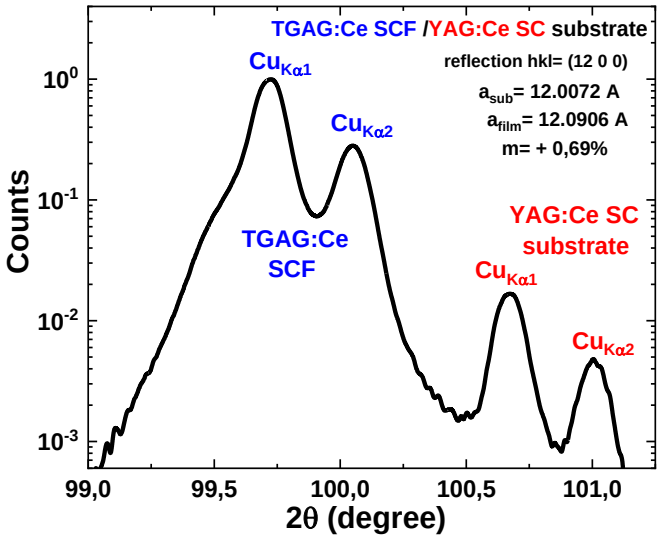

Fig.7.4. XRD pattern of (12 0 0) pane of 12 μm thick $Tb_{1.5}Gd_{1.5}AG$:Ce SCF grown on (1 0 0) oriented YAG:Ce substrate. The diffractions for $Cu_{k\alpha1}$ and $Cu_{k\alpha2}$ from the film and substrate are shown.

7.2.2 Optical and luminescence properties of TbGdAG:Ce SCF/YAG:Ce SC substrate composite color converters

The RT absorption spectra in 180-600 nm range of the YAG:Ce SC substrate (a) and $Tb_{1.5}Gd_{1.5}AG$:Ce SCF/YAG:Ce SC composite converter (b) are shown in Fig. 7.5. The absorption spectra of YAG:Ce substrate (Fig. 7.5a) shows two main intense absorption bands centered at ~460 nm (E_1) and ~340 nm (E_2) attributed to the allowed electric dipole transitions of Ce^{3+} ions from 4f (^4F_J) ground state to $5d_{1,2}(^2E)$ excited states, respectively. Absorption bands located around 230 nm related to the Ce^{3+} $4f\rightarrow5d_{3\text{-}5}(T_{2g})$ transitions. The peak position at 370 nm is close to the absorption band of the F^+-type center discussed in the work [167]. The intensities of Ce^{3+} absorption bands are enhanced with increasing of Ce^{3+} concentration in substrates from 0.1 to 0.5 at.% (S2 and S1 samples) in agreement with numerous previous studies [69].

The absorption spectra of the $Tb_{1.5}Gd_{1.5}AG$:Ce SCF/YAG:Ce SC epitaxial structures show the superposition of Ce^{3+} absorption bands in $Tb_{1.5}Gd_{1.5}AG$:Ce film and YAG crystal. Significant broadening of the main E_1 absorption band in the composite converter is a superior advantage for fitting with commercially available blue LEDs for WLED creation. Besides this, the absorption spectra contain sets of bands belonging to transitions of Tb^{3+} and Gd^{3+} ions. Namely, the bands centered around ~240 nm and ~290 nm belong to the low spin-allowed (LS) $4f\rightarrow5d_2$ and $4f\rightarrow5d_1$ absorption transitions of Tb^{3+} ions, respectively [149]. Weak absorption bands related to $4f\rightarrow4f$ Gd^{3+} transitions, peaked in the 313-317 nm range, strongly overleaped with bands related to the $4f\rightarrow5d_1$ (HS) transitions of Tb^{3+} ions. The peak at 373 nm is ascribed to the $^7F_6\rightarrow{}^5G_6$ absorption transitions of Tb^{3+}cations [149].

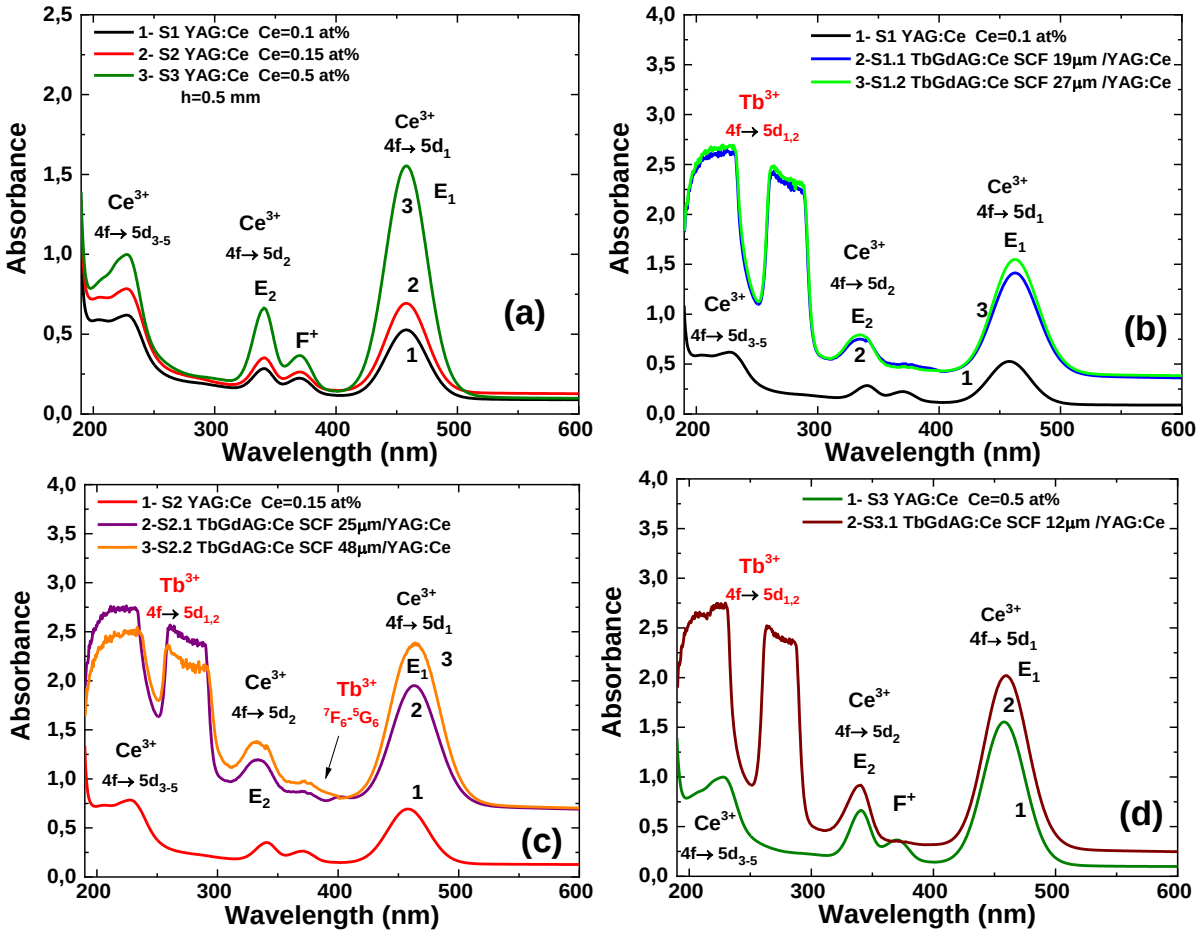

Fig.7.5. RT absorption spectra of YAG:Ce substrates (a) and $Tb_{1.5}Gd_{1.5}AG$:Ce SCF/YAG:Ce SC composite converters (b, c, d) compared with corresponding substrates.

Ce^{3+} PL emission and excitation spectra of $Tb_{1.5}Gd_{1.5}AG$:Ce SCF/YAG:Ce SC (S1.2) composite color converters are compared in Fig. 7.6 with its YAG:Ce constituent substrate (S1). The excitation bands of S1 substrate and S1.2 composite color converter recorded at RT for the maximum of Ce^{3+} emission band at 560 nm are mostly identical with their absorption spectra belonging to Ce^{3+} and Tb^{3+} ions absorption transitions. Therefore, the PL excitation spectrum presented in Fig. 7.6, shows that Tb^{3+} and Gd^{3+} cations act as sensitizers of Ce^{3+} luminescence.

Efficient energy transfer from the matrix containing Gd^{3+} and Tb^{3+}cations to the Ce^{3+} activator occurs in several directions (from Gd^{3+} to Tb^{3+} and then from Tb^{3+} to Ce^{3+} vice versa), which can also efficiently produce the yellow light caused by the Ce^{3+} emission both in $Tb_{1.5}Gd_{1.5}AG$:Ce SCF and YAG:Ce substrate of the composite color converter under UV or blue LED excitation. The most efficient energy migration over Gd and Tb sublattices to Ce^{3+} occurs at 50% concentration of Gd^{3+} and Tb^{3+} cations ions in $Tb_{1.5}Gd_{1.5}AG$:Ce garnet [20]. This fact determined the choice of film content of composite color converters developed in this work. In comparison with S1 substrate, the main Ce^{3+} excitation band related to $4f \rightarrow 5d_1$ transitions in (S1.2) composite converter is broadened from 86 nm to 90 nm, which, together with the red shift of the band by 9 nm, determines its maximum centered

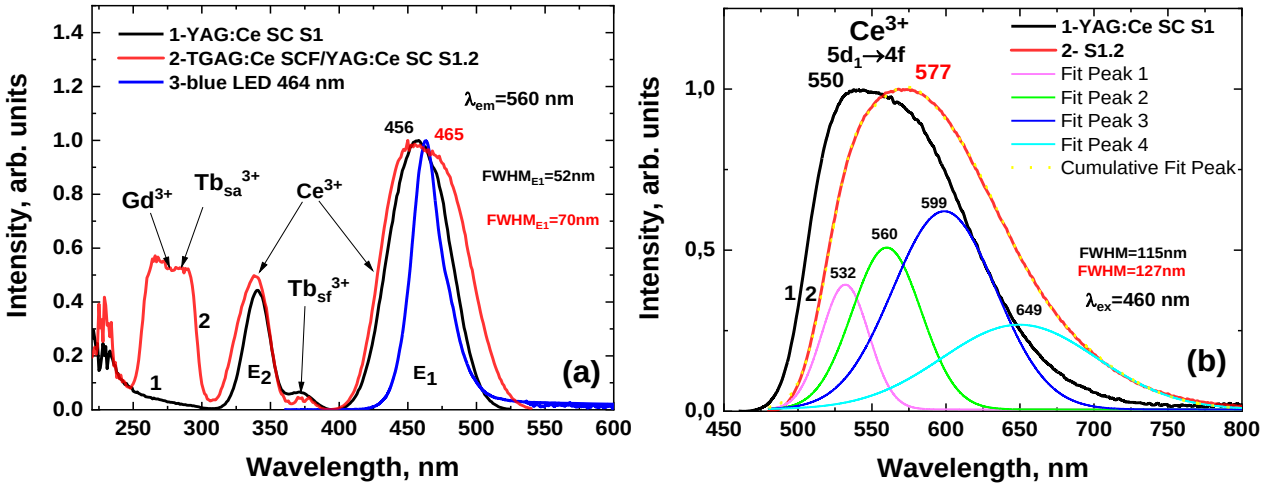

Fig. 7.6. (a) - RT PL excitation spectrum of the Ce^{3+} luminescence at 585 nm, and (b) - PL spectrum excited at 460 nm of YAG:Ce substrate (1, 3) and S3.1 sample of $Tb_{1.5}Gd_{1.5}AG$:Ce SCF/ YAG:Ce SC epitaxial structure (2, 4).

at 465 nm (S1.2). The full width at half maximum (FWHM) for the composite converter and YAG:Ce substrate is 52 and 70 nm respectively.

PL emission spectra of $Tb_{1.5}Gd_{1.5}AG$:Ce SCF/YAG:Ce SC epitaxial structures and YAG:Ce substrate excited at 460 nm are shown in Fig. 7.6b. In comparison to the typical 550 nm emission of YAG:Ce SC substrate, related to the $5d_1(E_{2g})\rightarrow 4f(^2F_{5/2})$ and $5d_1(E_{2g})\rightarrow 4f(^2F_{7/2})$ transitions of Ce^{3+} ions (Fig. 7.6b, curve 1), the emission spectra of composite converter represents the overlapped broad yellow-orange emission of Ce^{3+} ions both in YAG:Ce substrate and $Tb_{1.5}Gd_{1.5}AG$:Ce SCF. Using the decomposition into four Gaussian components the emission $5d_1\rightarrow{}^2F_{5/2}$ and $5d_1\rightarrow{}^2F_{7/2}$ subpeaks in the $Tb_{1.5}Gd_{1.5}AG$:Ce SCF/ YAG:Ce SC are located at 532 and 560 nm related to YAG:Ce SC emission; 599 and 649 nm from $Tb_{1.5}Gd_{1.5}AG$:Ce SCF, respectively. This makes it possible to achieve a broadened red-shifted emission band peaked at 577 nm with FWHM 127 nm in comparison with substrate emission maxima at 550 nm and FWHM equal to 115 nm. Such behavior is mainly explained by overlapping and increased crystal-field splitting of the Ce^{3+} 5d energy level in the film constituent part of the composite converter due to the larger sizes of ionic radius of Gd^{3+} and Tb^{3+} in comparison with Y^{3+} in dodecahedral positions of the garnet host. The position of the half-width and the intensity of the Ce^{3+} emission bands in film and substrate are also affected by its concentration in the matrix, which allows precious control of the photo-conversion properties of pc-WLEDs

7.2.3 Photoconversion properties of $Tb_{1.5}Gd_{1.5}AG$:Ce SCF/YAG:Ce SC substrate structures

Fig. 7.7 displays the emission spectra of pc-WLEDs prototypes composed of the band around 455 nm attributed to the emission of blue LED transmitted through the sample and the broad yellow emission band of Ce^{3+} ions in composite converters. For the YAG:Ce SC substrate with increasing

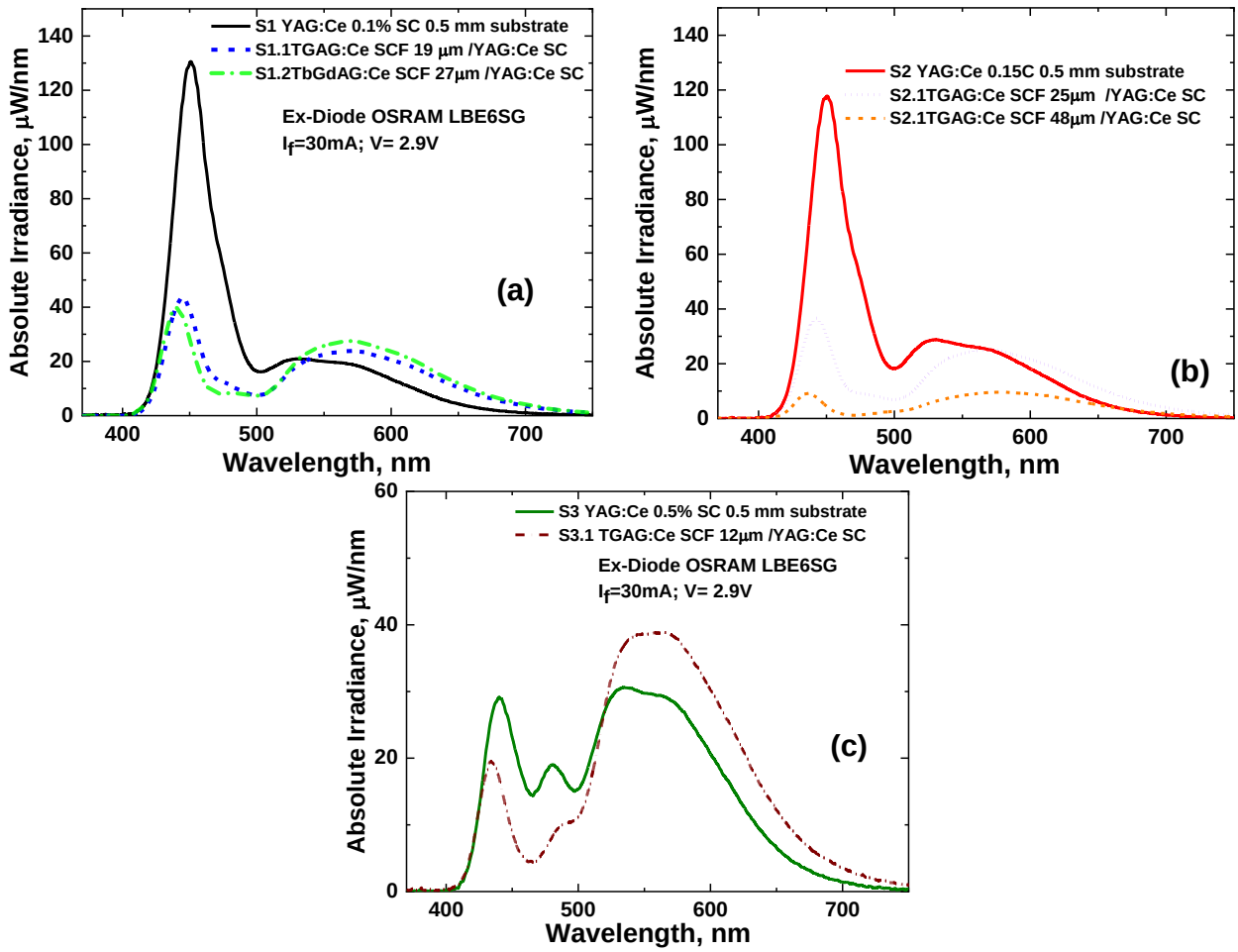

Fig. 7.7. The spectral performance of three groups (Table 1) of YAG:Ce SC substrates and TbGdAG:Ce SCF/YAG:Ce SC composite converters under 455 nm blue LED excitation.

Ce concentration the intensity of blue component is decreasing with the simultaneous increase of the yellow component in the emission spectra (solid line in Fig.7.7). It is related to higher absorption of blue light by SC substrates, according to absorption spectra Fig.7.5a. The chromaticity coordinates calculated from the photoconversion spectra of S1, S2 and S3 YAG:Ce SC substrates with different Ce content located on a straight trend line which connects the blue radiation area of the diode and yellow-green area of CIE diagram (Fig.6, blue trend line).

In the case of a composite converter, it is clearly seen that the imposition of a thin film on a substrate significantly changes the spectrum of the composite. A simultaneous change in the intensity and position of the blue band is observed, due to the additional absorption of the film, as well as the broadening and red-shifting of yellow emission components emanating from the basic substrate and film. It allows for decreasing the correlated color temperature (CCT) of radiation and optimizing its color rendering index (CRI), see Table 7.2.

As can be seen from the CIE-1931 chromaticity diagram Fig. 7.8, the color coordinates of composite converters from the three investigated groups form new trend lines (Fig. 7.8, black, red and

Table 7.2. Photoconversion properties of YAG:Ce substrates and $Tb_{1.5}Gd_{1.5}AG$:Ce SCF/YAG:Ce SC composite color converters. The thickness of the films is given for one side of the composite converter for convenience, on the backside of the substrate the film has the same thickness.

Sample	Substrate thickness [mm]	Film thickness [μm]	x	y	CCT [K]	CRI	LE [lm/W]
S1 YAG:Ce 0.1 at.% Ce SC	0.5		0.210	0.167	N/A	N/A	68
S1.1 $Tb_{1.5}Gd_{1.5}AG$:Ce SCF/YAG:Ce SC	0.5	19	0.324	0.306	5948	79	107
S1.2 $Tb_{1.5}Gd_{1.5}AG$:Ce SCF/YAG:Ce SC	0.5	27	0.349	0.338	4768	72	115
S2 YAG:Ce 0.15 at.% Ce SC	0.5		0.230	0.206	N/A	N/A	81
S2.1 $Tb_{1.5}Gd_{1.5}AG$:Ce SCF/YAG:Ce SC	0.5	25	0.345	0.333	4937	74	112.6
S2.2 $Tb_{1.5}Gd_{1.5}AG$:Ce SCF/YAG:Ce SC	0.5	45	0.397	0.386	3651	70	120
S3 YAG:Ce 0.5 at.% Ce SC	0.5		0.318	0.380	6019	65	130
S3.1 $Tb_{1.5}Gd_{1.5}AG$:Ce SCF/YAG:Ce SC	0.5	12	0.389	0.456	4255	62	145

green lines) together with their substrates, depending on the film thickness. In this case, the trend line is directed from the coordinates of the basic substrate towards the orange area of the diagram, which is lying in the region of 570 nm (according to the border wavelength scale of the diagram).

Thus, it is shown that the proposed approach for creating of composite color converters, makes it possible to achieve practically any color coordinates in the white area we are interested in, by selecting two tuning parameters: i) Ce^{3+} concentration in YAG:Ce substrate; ii) thickness of $Tb_{1.5}Gd_{1.5}AG$:Ce film. The color coordinates of S2.1 sample of the composite converter were dramatically shifted to near white coordinates (0.345, 0333), from its basic substrate located in a bluish

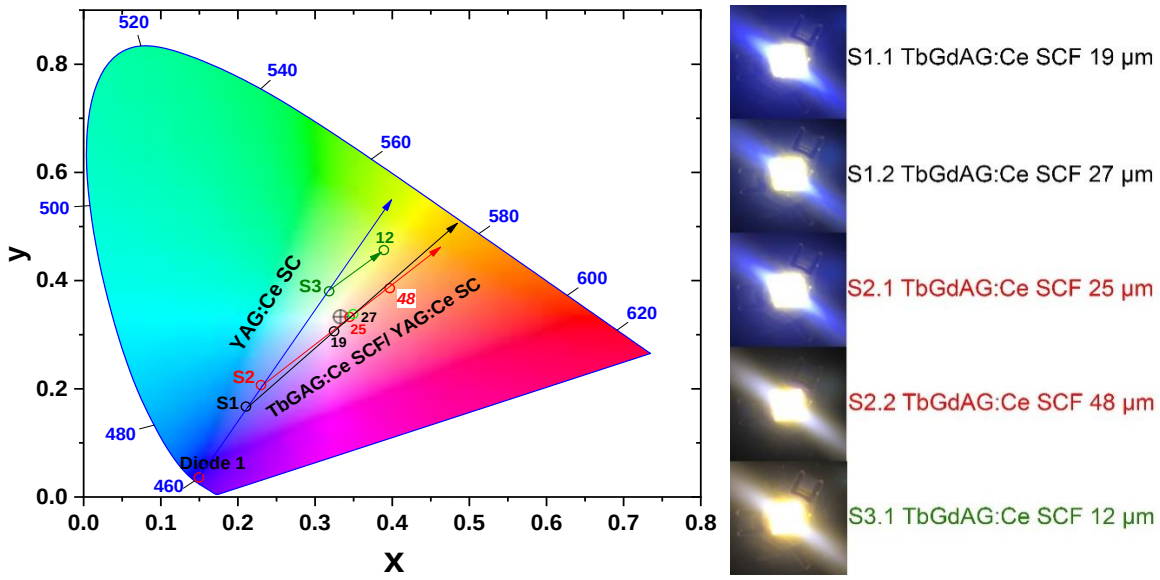

Fig. 7.8. Color coordinates of $Tb_{1.5}Gd_{1.5}AG$:Ce SCF/YAG:Ce SC composite color converter based WLEDs in CIE-1931 color space chromaticity diagram.

area with coordinates (0.230, 0.206). At the same time, there is an increase in the CRI in each studied group of converters, the values of which slightly decrease with an increase in the film thickness. In turn, an increase in luminous efficacy is observed with an increase of Ce^{3+} concentration in YAG:Ce SC substrate and the thickness of the film. The maximum obtained LE value is 145 lm/W for S3.1 sample.

In summary, the main photoconversion parameters of the WLEDs based on TbGdAG:Ce SCF/ YAG:Ce SC composite converter with various film thicknesses and YAG:Ce SC substrate and doping concentration are listed in Table 7.2.

Conclusions to Chapter 7

TbAG:Ce SCF/ YAG:Ce SC. Firstly, using LPE growth method we have developed a new type of TbAG:Ce SCF/YAG:Ce SC composite color converters for WLED application. The XRD and rocking curves analysis of the obtained converters confirmed the crystallization of one-phase TbAG:Ce SCF onto YAG:Ce SC substrates with excellent quality, despite the relatively large SCF-substrate lattice misfit being equal to 0.55%. The Ce^{3+} emission in TbAG:Ce SCF/YAG:Ce SC composite structures is significantly broadened and red-shifted yields the yellow/orange light compared to the green/yellow light from YAG:Ce SC substrate.

In this study, the photoconversion properties of novel composite converter, including CCC, CRI and LE were studied by varying Ce^{3+} concentration in the 0.1-0.25 % range in substrates and thicknesses of substrates (0.5-1 mm) and films (30-108 μm). The combination of different YAG:Ce substrates with various TbAG:Ce SCFs enables tuning the white light tons from cold white/daylight white (CCT > 6000 K) to neutral white (6000 K > CCT > 3300 K). The ideal white color was almost achieved for TbAG:Ce SCF/YAG:Ce (0.5 mm) SC converters with a SCF thickness of 30-104 μm under 455 nm LED excitation. A high LE, CRI and acceptable CCT is achieved also in these composite converter samples. The highest luminous efficiency of 157 lm/ W was obtained for the TbAG:Ce (124 μm) SCF/YAG:Ce (1mm) SC converter, which coordinates located in the yellow edge of the diagram, due to the relatively large film and crystal thicknesses.

Thus, we have shown a wide possibility of WLEDs color tuning depending on the thickness and Ce^{3+} concentration in the substrate and film of the proposed composite color converters. The obtained results indicate also that TbAG:Ce SCF /YAG:Ce SC composite converters possess great application potential in the different fields of WLEDs application.

TbGdAG:Ce SCF/ YAG:Ce SC. Another novel type of composite color photoconverters based on LPE grown $Tb_{1.5}Gd_{1.5}$AG:Ce SCFs onto YAG:Ce SC substrates, was developed. The XRD analysis of the obtained converters confirmed the crystallization of high structural quality $Tb_{1.5}Gd_{1.5}$AG:Ce SCF onto YAG:Ce substrates despite the large film/ substrate misfit of 0.69 %.

Three sets of $Tb_{1.5}Gd_{1.5}AG$:Ce SCF /YAG:Ce SC composite color converters with different Ce^{3+} concentrations (0.1; 0.15; 0.5 at.%) in the substrate and variable film thickness in the range were studied in detail using absorption, PL emission and PL excitation spectra measurements. Finally, the photoconversion properties of these epitaxial structures were investigated in combination with 455 nm emitting blue LED.

The PLE spectra revealed efficient $Gd^{3+} \rightarrow Tb^{3+}$ and Tb^{3+} Ce^{3+} cascade energy transfer in $Tb_{1.5}Gd_{1.5}AG$:Ce garnet host. Such cascade energy transfer occurs in several directions (from Gd^{3+} to Tb^{3+} and from Tb^{3+} to Ce^{3+} and vice versa), and can also efficiently produce the yellow light emission of Ce^{3+} ions both in $Tb_{1.5}Gd_{1.5}AG$:Ce SCF and YAG:Ce SC substrates under UV or blue LED excitation. The Ce^{3+} emission in $Tb_{1.5}Gd_{1.5}AG$:Ce SCF/YAG:Ce SC converter is significantly red shifted in comparison to that in reference YAG:Ce SC substrate. Furthermore, the redshift and broadening of Ce^{3+} emission band both in film and substrate of composite converter leads to the improvement of CRI of pc-WLEDs system due to the compensation of the red component in the spectrum of basic YAG:Ce garnet phosphor.

For this reason, developed $Tb_{1.5}Gd_{1.5}AG$:Ce SCF/YAG:Ce SC composite converters are responsible for producing white light when directly combined with commercially available LEDs and allow for resolving the problem of a high color temperature or low color rendering index of conventional WLEDs based on the conventional YAG:Ce phosphor.

General conclusions

Based on the analyses of obtained results in this work, some important conclusions were formulated regarding the structural and mechanical properties of crystals and SCFs of YAG, LuAG and TbAG garnets as well as the development of new types of photoconverters for WLEDs based on the epitaxial structures of Ce^{3+} doped LuAG:Ce, TbAG:Ce and $Tb_{1.5}Gd_{1.5}$AG:Ce SCFs, grown using LPE growth method onto YAG and YAG:Ce substrates. Namely, the most important achievements of this doctoral thesis can be formulated as follows.

1. The sets of photoconverters for WLED based on the SCFs of LuAG:Ce, TbAG:Ce and $Tb_{1.5}Gd_{1.5}$AG:Ce garnets with different thicknesses in the 19-160 μm range were successfully grown using the LPE method from PbO-B_2O_3 based flux onto undoped YAG substrates in the condition of the large SCF/substrate misfit *m* been equal to – 0.82% for LuAG:Ce SCF/YAG SC structure up to m= + 0.53% for TbAG:Ce SCF/YAG SC and m= + 0.65% for $Tb_{1.5}Gd_{1.5}$AG:Ce SCF/YAG SC structures, respectively.

2. High-resolution TEM and compositional analysis were performed for the first time for the cross-section of LuAG:Ce SCF/YAG SC and TbAG:Ce SCF/YAG SC epitaxial structures, revealing a film-substrate interface with high structural quality including the formation of a transition layer with a 5-8 nm thickness between LuAG:Ce and TbAG:Ce SCFs and YAG substrate, where the content of these layer changes gradually from YAG substrate towards LuAG:Ce and TbAG:Ce SCFs.

3. The very large misfit between LuAG:Ce and TbAG:Ce SCFs and YAG substrate in the – 0.82% ⇆ + 0.65% range results in the strong stretching of the LuAG:Ce lattice and strong compression of TbAG:Ce host starting from SCF/substrate interface. Furthermore, the relaxation of such mechanical stress towards the main volume of LuAG:Ce and TbAG:Ce SCFs can result in the gradual changing of their optical properties.

4. The acoustic microscopy was conducted for the first time for YAG:Ce substrate and the model LuAG:Ce SCF/YAG:Ce SC epitaxial structure. It was found that the phase velocities for the YAG:Ce substrate are very close (~4600 m/s) and weakly depend on the frequency of the exciting wave. On the opposite, the phase velocity for the LuAG:Ce SCF/YAG:Ce SC epitaxial structure depends on their frequency as a consequence of the complex interaction of the surface acoustic waves with the layered structure of the material.

5. The basic elastic properties of LuAG garnet (Young modulus of 290 GPa and Poisson ratio of 0.23) were correctly obtained for the first time based on the results of the investigation of LuAG:Ce SCF.

6. The investigation of structural, luminescence, and photoconversion properties (CCC, CRI, and LE) of LuAG:Ce, TbAG:Ce and $Tb_{1.5}Gd_{1.5}$AG:Ce SCF phosphors was performed for the first time. The trend line on the color coordinates diagram was obtained for the mentioned SCF converters

under excitation by 455 nm blue LED by the variation of film thickness in the 19-160 μm; 36-108 μm and 45-83 μm ranges, respectively.

7. It was shown that the LuAG:Ce SCFs are promising candidates for the creation of the temperature stable green emitting crystal converter under excitation with 455 nm blue LED. The optimal optical performance values in terms of LE of 129 lm/W, a CCT of 7570 K, and a CRI of 57 are achieved for the 92 μm thick LuAG:Ce SCF converter under excitation by 460 nm blue LED.

8. The efficient $Tb^{3+} \rightarrow Ce^{3+}$ and $Gd^{3+} \rightarrow Tb^{3+} \rightarrow Ce^{3+}$ cascade energy transfer processes were confirmed in SCFs of TbAG:Ce and $Tb_{1.5}Gd_{1.5}$AG:Ce garnets, respectively. Such cascade energy transfers occur in several directions (from Tb^{3+} cations to Ce^{3+} ions and vice versa and from Gd^{3+} to Tb^{3+} cations and then to Ce^{3+} ions) and results in efficient producing the yellow-orange light emission in TbAG:Ce and $Tb_{1.5}Gd_{1.5}$AG:Ce SCF phosphors under UV or blue LED excitation.

9. The Ce^{3+} emission in TbAG:Ce and $Tb_{1.5}Gd_{1.5}$AG:Ce SCF converters is significantly red shifted and broadened in comparison to YAG:Ce counterpart, which can result in the improvement of CRI of pc-WLEDs system due to the compensation of the red component in the spectrum of YAG:Ce garnet phosphor. For this reason, TbAG:Ce and $Tb_{1.5}Gd_{1.5}$AG:Ce SCF converters are responsible for resolving the problem of a high color temperature or low color rendering index of conventional WLEDs based on the YAG:Ce crystal phosphor.

10. It was shown that the developed TbAG:Ce and $Tb_{1.5}Gd_{1.5}$AG:Ce SCF phosphors are responsible for producing white light when combined with blue LEDs, emitting in the 450-464 range. The several advantages of TbAG:Ce and $Tb_{1.5}Gd_{1.5}$AG:Ce SCF converters over their YAG:Ce single crystal converter were evidenced as well:

- The CRI values were higher for TbAG:Ce SCF converters compared with reference YAG:Ce single crystal converters.
- The ideal white color was almost achieved for the TbAG:Ce SCF converter with a thickness of 55 μm under 455 nm blue LED excitation.
- The highest LE value of 132.6 lm/W was obtained for the 108 μm-thick $Tb_{1.5}Gd_{1.5}$AG:Ce SCF converter under 455 nm blue LED excitation.

11. It was shown that the LuAG:Ce, TbAG:Ce and $Tb_{1.5}Gd_{1.5}$AG:Ce SCF converters can be suitable also for the development of multilayered composite color converters based on YAG:Ce or other Ce^{3+} doped garnet crystal substrates using the LPE growth method.

12. The two sets of composite photoconverters for WLED based on the SCFs of TbAG:Ce and $Tb_{1.5}Gd_{1.5}$AG:Ce garnets with different thicknesses were successfully crystalized using the LPE method from $PbO\text{-}B_2O_3$ based flux onto Ce^{3+} doped YAG:Ce SC substrates with 0.5-1 nm thickness and Ce content in the 0.1-0.25 at.% range.

13. The investigation of structural, luminescence, and photoconversion properties (CCC, CRI and LE) of the TbAG:Ce SCF/YAG:Ce SC and $Tb_{1.5}Gd_{1.5}$AG:Ce SCF/YAG:Ce SC composite phosphors was performed for the first time. It was shown that these composite phosphors are responsible for producing white light when combined with 455 nm emitting blue LED.

14. The trend line on the color coordinates diagram was obtained for the first time for the TbAG:Ce SCF/YAG:Ce SC and $Tb_{1.5}Gd_{1.5}$AG:Ce SCF/YAG:Ce SC composite converters by varying Ce^{3+} concentration in the 0.1-0.5 at. % range in substrates and thicknesses of substrates in 0.5-1 mm range and films in 30-124 μm and 12-45 μm ranges, respectively.

15. Important advantages of TbAG:Ce and $Tb_{1.5}Gd_{1.5}$AG:Ce SCF composite converters over their YAG:Ce single crystal counterparts were evidenced:

- The combination of different YAG:Ce SC substrates with TbAG:Ce SCF converters with 19-124 μm thickness enables tuning the white light tons from cold white/daylight white (CCT > 6000 K) to neutral white (6000 K > CCT > 3300 K).
- Almost ideal white color (theoretical white point) was almost achieved for TbAG:Ce SCF/YAG:Ce (0.5 mm) SC converters with a SCF thickness of 30-104 μm under 455 nm LED excitation. A high LE, CRI and acceptable CCT are achieved also in these composite converter samples.
- The highest luminous efficiency of 157 lm/W was obtained for the TbAG:Ce (124 μm) SCF/YAG:Ce (1mm) SC converter, which coordinates located in the yellow edge of the diagram, due to the relatively large film and crystal thicknesses.
- An increase in luminous efficacy is observed with an increase of Ce^{3+} content in YAG:Ce substrate and the thickness of the $Tb_{1.5}Gd_{1.5}$AG:Ce film. The maximum LE value is obtained for 145 lm/W for 12 thick $Tb_{1.5}Gd_{1.5}$AG:Ce SCF/YAG:Ce SC (0.5 mm) composite converter.

16. Finally, it is shown that the proposed approach for creating composite SCF-crystal color converters, makes it possible to achieve practically any color “on demand” in the white area, by selecting two tuning parameters: i) Ce^{3+} concentration in YAG:Ce substrate; ii) thickness of TbAG:Ce or $Tb_{1.5}Gd_{1.5}$AG:Ce films and YAG:Ce substrates.

References

[1] T. Gao, J. Tian, Y. Liu, R. Liu, W. Zhuang, Garnet phosphors for white-light-emitting diodes: modification and calculation, Dalton Trans. 50 (2021) 3769–3781. https://doi.org/10.1039/d0dt04368k.

[2] Q. Meng, G. Zhao, Q. Zhu, X. Li, X. Sun, J.-G. Li, Site-selective and cooperative doping of $Gd_3Al_5O_{12}$:Ce garnets for structural stabilization and warm WLED lighting of low CCT and high CRI, Dalton Trans. 51 (2022) 645–654. https://doi.org/10.1039/d1dt03599a .

[3] A.A. Setlur, W.J. Heward, M.E. Hannah, U. Happek, Incorporation of Si^{4+}–N^{3-} into Ce^{3+} -doped garnets for warm white LED phosphors, Chem. Mater. 20 (2008) 6277–6283. https://doi.org/10.1021/cm801732d .

[4] M.S. Jang, Y.H. Choi, S. Wu, T.G. Lim, J.S. Yoo, Material properties of the Ce^{3+}-doped garnet phosphor for a white LED application, J. Inf. Disp. 17 (2016) 117–123. https://doi.org/10.1080/15980316.2016.1205527 .

[5] J. Wang, T. Han, T. Lang, M. Tu, L. Peng, Synthesis and photoluminescence properties of cerium-doped terbium–yttrium aluminum garnet phosphor for white light-emitting diodes applications, Opt. Eng. 54 (2015) 117106. https://doi.org/10.1117/1.oe.54.11.117106.

[6] Z. Xia, A. Meijerink, Ce^{3+}-Doped garnet phosphors: composition modification, luminescence properties and applications, Chem. Soc. Rev. 46 (2017) 275–299. https://doi.org/10.1039/c6cs00551a

[7] A. Bindhu, J.I. Naseemabeevi, S. Ganesanpotti, Distortion and energy transfer assisted tunability in garnet phosphors, Crit. Rev. Solid State Mater. Sci. 47 (2022) 621–664. https://doi.org/10.1080/10408436.2021.1935211 .

[8] V. Monteseguro, P. Rodríguez-Hernández, H.M. Ortiz, V. Venkatramu, F.J. Manjón, C.K. Jayasankar, V. Lavín, A. Muñoz, Structural, elastic and vibrational properties of nanocrystalline lutetium gallium garnet under high pressure, Phys. Chem. Chem. Phys. 17 (2015) 9454–9464. https://doi.org/10.1039/c4cp05903d .

[9] D. Kundaliya, M. Raukas, A.M. Scotch, D. Hamby, K. Mishra, M. Stough, Wavelength converter for an LED and LED containing same, Patent US8937332, 2012, https://patents.google.com/patent/US8937332B2/en

[10] V. Gorbenko, T. Zorenko, P. Pawlowski, A. Iskaliyeva, K. Paprocki, A. Suchocki, Y. Zhydachevskii, A. Fedorov, N. Khaidukov, R. Van Deun, F. Schröppel, A. Osvet, M. Batentschuk, Y. Zorenko, Luminescent and scintillation properties of Ce^{3+} doped $Ca_2RMgScSi_3O_{12}$ (R = Y, Lu) single crystalline films, J. Lumin. 195 (2018) 362–370. https://doi.org/10.1016/j.jlumin.2017.11.052

[11] K. Bartosiewicz, V. Babin, A. Beitlerova, P. Bohacek, K. Jurek, M. Nikl, The temperature dependence studies of rare-earth (Dy^{3+}, Sm^{3+}, Eu^{3+} and Tb^{3+}) activated $Gd_3Ga_3Al_2O_{12}$ garnet single crystals, J. Lumin. 189 (2017) 126–139. https://doi.org/10.1016/j.jlumin.2016.09.053 .

[12] K. Bartosiewicz, V. Babin, J.A. Mares, A. Beitlerova, Y. Zorenko, A. Iskaliyeva, V. Gorbenko, Z. Bryknar, M. Nikl, Luminescence and energy transfer processes in Ce^{3+} activated $(Gd,Tb)_3Al_5O_{12}$ single crystalline films, J. Lumin. 188 (2017) 60–66. https://doi.org/10.1016/j.jlumin.2017.04.010 .

[13] Y. Liu, J. Zou, M. Shi, B. Yang, Y. Han, W. Li, Z. Wang, H. Zhou, M. Li, N. Jiang, Effect of gallium ion content on thermal stability and reliability of YAG: Ce phosphor films for white LEDs, Ceram. Int. 44 (2018) 1091–1098. https://doi.org/10.1016/j.ceramint.2017.10.056 .

[14] G.-Y. Li, Y. Zheng, Y.-X. Jiang, Z. Zhang, Y. Cao, Guided wave elastography of layered soft tissues, Acta Biomater. 84 (2019) 293–304. https://doi.org/10.1016/j.actbio.2018.12.002 .

[15] G. Menzer, XX. Die kristallstruktur der granate, Z. Kristallogr. Cryst. Mater. 69 (1929) 300–396. https://doi.org/10.1524/zkri.1929.69.1.300 .

[16] Structure and Properties of Inorganic Solids, Elsevier.com. (n.d.). https://shop.elsevier.com/ books/ structure-and-properties-of-inorganic-solids/galasso/978-0-08-006873-2 (accessed October 4, 2023) .

[17] K. Bartosiewicz, V. Babin, K. Kamada, A. Yoshikawa, A. Beitlerova, M. Nikl, Effects of Gd/Lu ratio on the luminescence properties and garnet phase stability of Ce^{3+} activated $Gd_xLu_{3-x}Al_5O_{12}$ single crystals, Opt. Mater. (Amst.). 80 (2018) 98–105. https://doi.org/10.1016/j.optmat.2018.04.023.

[18] Y. Kanke, A. Navrotsky, A calorimetric study of the lanthanide aluminum oxides and the lanthanide gallium oxides: Stability of the perovskites and the garnets, J. Solid State Chem. 141 (1998) 424–436. https://doi.org/10.1006/jssc.1998.7969 .

[19] K. Bartosiewicz, V. Babin, K. Kamada, A. Yoshikawa, S. Kurosawa, A. Beitlerova, R. Kucerkova, M. Nikl, Y. Zorenko, Ga for Al substitution effects on the garnet phase stability and luminescence properties of $Gd_3Ga_xAl_{5-x}O_{12}$:Ce single crystals, J. Lumin. 216 (2019) 116724. https://doi.org/10.1016/j.jlumin.2019.116724 .

[20] R.D. Shannon, Revised effective ionic radii and systematic studies of interatomic distances in halides and chalcogenides, Acta Crystallogr. A. 32 (1976) 751–767. https://doi.org/10.1107/s0567739476001551 .

[21] M. Nikl, A. Yoshikawa, Recent R&D trends in inorganic single-crystal scintillator materials for radiation detection, Adv. Opt. Mater. 3 (2015) 463–481. https://doi.org/10.1002/adom.201400571 .

[22] Z. Xia, Q. Liu, Progress in discovery and structural design of color conversion phosphors for LEDs, Prog. Mater. Sci. 84 (2016) 59–117. https://doi.org/10.1016/j.pmatsci.2016.09.007 .

[23] H. Przybylińska, A. Wittlin, C.-G. Ma, M.G. Brik, A. Kamińska, P. Sybilski, Y. Zorenko, M. Nikl, V. Gorbenko, A. Fedorov, M. Kučera, A. Suchocki, Rare-earth antisites in lutetium aluminum

garnets: Influence on lattice parameter and Ce^{3+} multicenter structure, Opt. Mater. (Amst.). 36 (2014) 1515–1519. https://doi.org/10.1016/j.optmat.2014.04.015 .

[24] C. Dujardin, E. Auffray, E. Bourret-Courchesne, P. Dorenbos, P. Lecoq, M. Nikl, A.N. Vasil'ev, A. Yoshikawa, R.-Y. Zhu, Needs, trends, and advances in inorganic scintillators, IEEE Trans. Nucl. Sci. 65 (2018) 1977–1997. https://doi.org/10.1109/tns.2018.2840160 .

[25] F.D. Patel, E.C. Honea, J. Speth, S.A. Payne, R. Hutcheson, R. Equall, Laser demonstration of $Yb3Al_5O_{12}$ (YbAG) and materials properties of highly doped Yb:YAG, IEEE J. Quantum Electron. 37 (2001) 135–144. https://doi.org/10.1109/3.892735 .

[26] Z. Huang, J. Feng, W. Pan, Elastic properties of YAG: First-principles calculation and experimental investigation, Solid State Sci. 14 (2012) 1327–1332. https://doi.org/10.1016/j.solidstatesciences.2012.07.008 .

[27] A. Koch, C. Raven, P. Spanne, A. Snigirev, X-ray imaging with submicrometer resolution employing transparent luminescent screens, J. Opt. Soc. Am. A Opt. Image Sci. Vis. 15 (1998) 1940. https://doi.org/10.1364/josaa.15.001940 .

[28] M. Nikl, Nanocomposite, ceramic, and thin film scintillators, CRC Press, Boca Raton, FL, 2016.

[29] T. Martin, A. Koch, Recent developments in X-ray imaging with micrometer spatial resolution, J. Synchrotron Radiat. 13 (2006) 180–194. https://doi.org/10.1107/s0909049506000550 .

[30] N. Wei, T. Lu, F. Li, W. Zhang, B. Ma, Z. Lu, J. Qi, Transparent $Ce:Y_3Al_5O_{12}$ ceramic phosphors for white light-emitting diodes, Appl. Phys. Lett. 101 (2012) 061902. https://doi.org/10.1063/1.4742896 .

[31] M. Odziomek, F. Chaput, C. Dujardin, F. Lerouge, P. Cassette, M. Sitarz, S. Parola, Design and application of high optical quality YAG:Ce nanocrystal-loaded silica aerogels, ACS Appl. Mater. Interfaces. 10 (2018) 32304–32312. https://doi.org/10.1021/acsami.8b09229 .

[32] V.F. Kitaeva, E.V. Zharikov, I.L. Chistyi, The properties of crystals with garnet structure, Physica Status Solidi A Appl. Res. 92 (1985) 475–488. https://doi.org/10.1002/pssa.2210920217 .

[33] R.M. Martin, R.M. Martin, Electronic structure: Basic theory and practical methods, Cambridge University Press, Cambridge, England, 2004.

[34] P. Dorenbos, Electronic structure and optical properties of the lanthanide activated $RE_3(Al_{1-x}Ga_x)_5O_{12}$ (RE=Gd, Y, Lu) garnet compounds, J. Lumin. 134 (2013) 310–318. https://doi.org/10.1016/j.jlumin.2012.08.028 .

[35] P. Dorenbos, Charge transfer bands in optical materials and related defect level location, Opt. Mater. (Amst.). 69 (2017) 8–22. https://doi.org/10.1016/j.optmat.2017.03.061 .

[36] Modern luminescence spectroscopy of minerals and materials, Springer-Verlag, Berlin/Heidelberg, 2005.

[37] D.-S. Yang, High-resolution electron spectroscopy of gas-phase Metal−Aromatic complexes, J. Phys. Chem. Lett. 2 (2011) 25–33. https://doi.org/10.1021/jz101550d .

[38] P. Dorenbos, The 4f ↔4f−5d1 transitions of the trivalent lanthanides in halogenides and chalcogenides, J. Lumin. 91 (2000) 91–106. https://doi.org/10.1016/s0022-2313(00)00197-6 .

[39] Y.-C. Lin, M. Bettinelli, M. Karlsson, Unraveling the mechanisms of thermal quenching of luminescence in Ce^{3+}-doped garnet phosphors, Chem. Mater. 31 (2019) 3851–3862. https://doi.org/10.1021/acs.chemmater.8b05300 .

[40] P.D. Rack, P.H. Holloway, The structure, device physics, and material properties of thin film electroluminescent displays, Mater. Sci. Eng. R Rep. 21 (1998) 171–219. https://doi.org/10.1016/s0927-796x(97)00010-7 .

[41] P. Dorenbos, Relating the energy of the $[Xe]5d^1$ configuration of Ce^{3+} in inorganic compounds with anion polarizability and cation electronegativity, Phys. Rev. B Condens. Matter. 65 (2002). https://doi.org/10.1103/physrevb.65.235110 .

[42] P. Dorenbos, 5d-level energies of Ce^{3+} and the crystalline environment. IV. Aluminates and "simple" oxides, J. Lumin. 99 (2002) 283–299. https://doi.org/10.1016/s0022-2313(02)00347-2 .

[43] E. Gibney, Nobel for blue LED that revolutionized lighting, Nature. 514 (2014) 152–153. https://doi.org/10.1038/514152a .

[44] C.-C. Sun, Y.-Y. Chang, T.-H. Yang, T.-Y. Chung, C.-C. Chen, T.-X. Lee, D.-R. Li, C.-Y. Lu, Z.-Y. Ting, B. Glorieux, Y.-C. Chen, K.-Y. Lai, C.-Y. Liu, Packaging efficiency in phosphor-converted white LEDs and its impact to the limit of luminous efficacy, J. Solid State Light. 1 (2014). https://doi.org/10.1186/s40539-014-0019-0 .

[45] Y. Huang, Y. Nakai, T. Tsuboi, H.J. Seo, The new red-emitting phosphor of oxyfluoride $Ca_2RF_4PO_4:Eu^{3+}$ (R=Gd, Y) for solid state lighting applications, Opt. Express. 19 (2011) 6303. https://doi.org/10.1364/oe.19.006303 .

[46] B.V. Ratnam, M. Jayasimhadri, G. Bhaskar Kumar, K. Jang, S.S. Kim, Y.I. Lee, J.M. Lim, D.S. Shin, T.K. Song, Synthesis and luminescent features of $NaCaPO_4:Tb^{3+}$ green phosphor for near UV-based LEDs, J. Alloys Compd. 564 (2013) 100–104. https://doi.org/10.1016/j.jallcom.2013.01.203 .

[47] Y.-C. Chiu, W.-R. Liu, C.-K. Chang, C.-C. Liao, Y.-T. Yeh, S.-M. Jang, T.-M. Chen, $Ca_2PO_4Cl:Eu^{2+}$: an intense near-ultraviolet converting blue phosphor for white light-emitting diodes, J. Mater. Chem. 20 (2010) 1755. https://doi.org/10.1039/b920610h .

[48] G. Li, Y. Tian, Y. Zhao, J. Lin, Recent progress in luminescence tuning of $Ce^{3+}$and Eu^{2+}-activated phosphors for pc-WLEDs, Chem. Soc. Rev. 44 (2015) 8688–8713. https://doi.org/10.1039/c4cs00446a .

[49] K. Kamada, T. Endo, K. Tsutumi, T. Yanagida, Y. Fujimoto, A. Fukabori, A. Yoshikawa, J. Pejchal, M. Nikl, Composition engineering in cerium-doped $(Lu,Gd)_3(Ga,Al)_5O_{12}$ single-crystal scintillators, Cryst. Growth Des. 11 (2011) 4484–4490. https://doi.org/10.1021/cg200694a .

[50] M. Fasoli, A. Vedda, M. Nikl, C. Jiang, B.P. Uberuaga, D.A. Andersson, K.J. McClellan, C.R. Stanek, Band-gap engineering for removing shallow traps in rare-earth $Lu_3Al_5O_{12}$ garnet scintillators using Ga^{3+} doping, Phys. Rev. B Condens. Matter Mater. Phys. 84 (2011). https://doi.org/10.1103/physrevb.84.081102 .

[51] J. Chen, Y. Tang, X. Yi, Y. Tian, G. Ao, D. Hao, Y. Lin, S. Zhou, Fabrication of $(Tb,Gd)_3Al_5O_{12}:Ce^{3+}$ phosphor ceramics for warm white light-emitting diodes application, Opt. Mater. Express. 9 (2019) 3333. https://doi.org/10.1364/ome.9.003333 .

[52] S. Arjoca, D. Inomata, Y. Matsushita, K. Shimamura, Growth and optical properties of $(Y_{1-x}Gd_x)_3Al_5O_{12}$:Ce single crystal phosphors for high-brightness neutral white LEDs and LDs, CrystEngComm. 18 (2016) 4799–4806. https://doi.org/10.1039/c6ce00500d .

[53] K. Bando, K. Sakano, Y. Noguchi, Y. Shimizu, Development of high-bright and pure-white LED lamps, J. Light Vis. Environ. 22 (1998) 2–5. https://doi.org/10.2150/jlve.22.1_2 .

[54] H.-M. Lee, C.-C. Cheng, C.-Y. Huang, The synthesis and optical property of solid-state-prepared YAG:Ce phosphor by a spray-drying method, Mater. Res. Bull. 44 (2009) 1081–1085. https://doi.org/10.1016/j.materresbull.2008.10.006 .

[55] B. Huang, Y. Ma, S. Qian, D. Zou, G. Zheng, Z. Dai, Luminescent properties of low-temperature-hydrothermally-synthesized and post-treated YAG:Ce (5%) phosphors, Opt. Mater. (Amst.). 36 (2014) 1561–1565. https://doi.org/10.1016/j.optmat.2014.04.025 .

[56] S. Zhang, W. Zhuang, T. He, Y. Liu, R. Liu, W. Gao, Y. Hu, Z. Long, Study on co-precipitation synthesized $Y_3Al_5O_{12}$:Ce yellow phosphor for white LED, J. Rare Earths. 28 (2010) 713–716. https://doi.org/10.1016/s1002-0721(09)60186-1 .

[57] Y.C. Kang, I.W. Lenggoro, S.B. Park, K. Okuyama, YAG:Ce phosphor particles prepared by ultrasonic spray pyrolysis, Mater. Res. Bull. 35 (2000) 789–798. https://doi.org/10.1016/s0025-5408(00)00257-9 .

[58] L. Zhang, Z. Lu, J. Zhu, H. Yang, P. Han, Y. Chen, Q. Zhang, Citrate sol-gel combustion preparation and photoluminescence properties of YAG:Ce phosphors, J. Rare Earths. 30 (2012) 289–296. https://doi.org/10.1016/s1002-0721(12)60040-4.

[59] K.V.K. Gupta, A. Muley, P. Yadav, C.P. Joshi, S.V. Moharil, Combustion synthesis of YAG:Ce and related phosphors, Appl. Phys. B. 105 (2011) 479–484. https://doi.org/10.1007/s00340-011-4685-y

[60] S. Pimputkar, J.S. Speck, S.P. DenBaars, S. Nakamura, Prospects for LED lighting, Nat. Photonics. 3 (2009) 180–182. https://doi.org/10.1038/nphoton.2009.32 .

[61] S. Bierhuizen, M. Krames, G. Harbers, G. Weijers, Performance and trends of high power light emitting diodes, in: I.T. Ferguson, N. Narendran, T. Taguchi, I.E. Ashdown (Eds.), SPIE Proceedings, SPIE, 2007.

[62] S.C. Allen, A.J. Steckl, A nearly ideal phosphor-converted white light-emitting diode, Appl. Phys. Lett. 92 (2008). https://doi.org/10.1063/1.2901378 .

[63] Y.H. Kim, N.S.M. Viswanath, S. Unithrattil, H.J. Kim, W.B. Im, Review—phosphor plates for high-power LED applications: Challenges and opportunities toward perfect lighting, ECS J. Solid State Sci. Technol. 7 (2018) R3134–R3147. https://doi.org/10.1149/2.0181801jss .

[64] E.G. Víllora, S. Arjoca, D. Inomata, K. Shimamura, Single-crystal phosphors for high-brightness white LEDs/LDs, in: H. Jeon, L.-W. Tu, M.R. Krames, M. Strassburg (Eds.), SPIE Proceedings, SPIE, 2016.

[65] S. Fujita, A. Sakamoto, S. Tanabe, Luminescence characteristics of YAG glass–ceramic phosphor for white LED, IEEE J. Sel. Top. Quantum Electron. 14 (2008) 1387–1391. https://doi.org/10.1109/jstqe.2008.920285 .

[66] S. Arjoca, E.G. Víllora, D. Inomata, K. Aoki, Y. Sugahara, K. Shimamura, Temperature dependence of Ce:YAG single-crystal phosphors for high-brightness white LEDs/LDs, Mater. Res. Express. 2 (2015) 055503. https://doi.org/10.1088/2053-1591/2/5/055503 .

[67] S.V. Nizhankovskyi, A.V. Tan'ko, Y.N. Savvin, S.I. Krivonogov, A.T. Budnikov, A.V. Voloshin, Single crystalline YAG:Ce phosphor for powerful solid-state sources of white light. The influence of production conditions on luminescence properties and lighting characteristics, Opt. Spectrosc. 120 (2016) 915–921. https://doi.org/10.1134/s0030400x16050210 .

[68] W.-H. Chao, R.-J. Wu, T.-B. Wu, Structural and luminescent properties of YAG:Ce thin film phosphor, J. Alloys Compd. 506 (2010) 98–102. https://doi.org/10.1016/j.jallcom.2010.04.136 .

[69] C.T. Hsu, S.K. Yen, Electrochemical synthesis of thin film YAG on inconel substrate, Electrochem. Solid State Letters. 9 (2006) D9. https://doi.org/10.1149/1.2170482 .

[70] Y.K. Lee, J.R. Oh, Y.R. Do, Enhanced extraction efficiency of Y_2O_3:Eu^{3+} thin-film phosphors coated with hexagonally close-packed polystyrene nanosphere monolayers, Appl. Phys. Lett. 91 (2007). https://doi.org/10.1063/1.2763974 .

[71] G.R. Bai, H.L.M. Chang, C.M. Foster, Erratum: '"Preparation of single-crystal $Y_3Al_5O_{12}$ thin film by metalorganic chemical vapor deposition. Appl. Phys. Lett. 65 (1994) 790–790. https://doi.org/10.1063/1.113088 .

[72] L.A. Díaz-Torres, E. De la Rosa, P. Salas, C. Angeles-Chavez, L.B. Arenas, J. Nieto, Nanoparticle thin films of nanocrystalline YAG by pulsed laser deposition, Opt. Mater. (Amst.). 27 (2005) 1217–1220. https://doi.org/10.1016/j.optmat.2004.10.017 .

[73] Y. Zorenko, V. Gorbenko, V. Savchyn, T. Voznyak, O. Sidletskiy, B. Grinyov, M. Nikl, J. Mares, T. Martin, P.-A. Douissard, Single crystalline film scintillators based on the orthosilicate, perovskite and garnet compounds, IEEE Trans. Nucl. Sci. 59 (2012) 2260–2268. https://doi.org/10.1109/tns.2012.2188907 .

[74] M.G. Mauk, Liquid-Phase Epitaxy, Digital Encyclopedia of Applied Physics. (2023) 1–31. https://doi.org/10.1002/3527600434.eap812 .

[75] P. Capper, M. Mauk, Liquid Phase Epitaxy of electronic, optical and optoelectronic materials, John Wiley & Sons, 2007.

[76] A. Markovskyi, V. Gorbenko, T. Zorenko, T. Yokosawa, J. Will, E. Spiecker, M. Batentschuk, J. Elia, A. Fedorov, Y. Zorenko, LPE growth of $Tb_3Al_5O_{12}$:Ce single crystalline film converters for WLED application, CrystEngComm. 23 (2021) 3212–3219. https://doi.org/10.1039/d1ce00268f .

[77] V.I. Chani, A. Yoshikawa, H. Machida, T. Fukuda, $(Tb,Yb)_3Al_5O_{12}$ garnet: crystal-chemistry and fiber growth by micro-pulling-down technique, Mater. Sci. Eng. B Solid State Mater. Adv. Technol. 75 (2000) 53–60. https://doi.org/10.1016/s0921-5107(00)00382-2 .

[78] Y. Zorenko, V. Gorbenko, T. Voznyak, T. Zorenko, B. Kuklinski, R. Turos-Matysyak, M. Grinberg, Luminescence properties of phosphors based on $Tb_3Al_5O_{12}$ (TbAG) terbium-aluminum garnet, Opt. Spectrosc. 106 (2009) 365–374. https://doi.org/10.1134/s0030400x09030102 .

[79] A. Markovskyi, V. Gorbenko, T. Zorenko, S. Nizhankovskiy, A. Fedorov, Y. Zorenko, Composite color converters based on $Tb_3Al_5O_{12}$:Ce single-crystalline films and $Y_3Al_5O_{12}$:Ce crystal substrates, Phys. Status Solidi Rapid Res. Lett. 15 (2021). https://doi.org/10.1002/pssr.202100173 .

[80] Y. Zorenko, V. Gorbenko, J. Vasylkiv, A. Zelenyj, A. Fedorov, R. Kucerkova, J.A. Mares, M. Nikl, P. Bilski, A. Twardak, Growth and luminescent properties of scintillators based on the single crystalline films of $Lu_{3-x}Gd_xAl_5O_{12}$:Ce garnet, Mater. Res. Bull. 64 (2015) 355–363. https://doi.org/10.1016/j.materresbull.2015.01.020 .

[81] K. Bartosiewicz, V. Babin, M. Nikl, J.A. Mares, Y. Zorenko, V. Gorbenko, Luminescence and energy transfer processes in $(Lu,Tb)_3Al_5O_{12}$ single crystalline films doped with Ce^{3+}, J. Lumin. 173 (2016) 141–148. https://doi.org/10.1016/j.jlumin.2016.01.022.

[82] J.Y. Cho, K.-Y. Ko, Y.R. Do, Optical properties of sol–gel derived Y_2O_3:Eu^{3+} thin-film phosphors for display applications, Thin Solid Films. 515 (2007) 3373–3379. https://doi.org/10.1016/j.tsf.2006.09.029.

[83] G.R. Bai, H.L.M. Chang, C.M. Foster, Preparation of single-crystal $Y_3Al_5O_{12}$ thin film by metalorganic chemical vapor deposition, Appl. Phys. Lett. 64 (1994) 1777–1779. https://doi.org/10.1063/1.111805.

[84] Y. Zorenko, V. Gorbenko, E. Mihokova, M. Nikl, K. Nejezchleb, A. Vedda, V. Kolobanov, D. Spassky. Single crystalline film scintillators based on Ce- and Pr-doped aluminium garnets, Radiat. Meas. 42 (2007) 521–527. https://doi.org/10.1016/j.radmeas.2007.01.045.

[85] Y. Zorenko, V. Gorbenko, Growth peculiarities of the $R_3Al_5O_{12}$ (R=Lu, Yb, Tb, Eu–Y) single crystalline film phosphors by liquid phase epitaxy, Radiat. Meas. 42 (2007) 907–910. https://doi.org/10.1016/j.radmeas.2007.02.049.

[86] Y. Zorenko, P.-A. Douissard, T. Martin, F. Riva, V. Gorbenko, T. Zorenko, K. Paprocki, A. Iskalieva, S. Witkiewicz, A. Fedorov, P. Bilski, A. Twardak, Scintillating screens based on the LPE grown $Tb_3Al_5O_{12}$:Ce single crystalline films, Opt. Mater. (Amst.). 65 (2017) 73–81. https://doi.org/10.1016/j.optmat.2016.09.066.

[87] H.J. Levinstein, S. Licht, R.W. Landorf, S.L. Blank, Growth of high-quality garnet thin films from supercooled melts, Appl. Phys. Lett. 19 (1971) 486–488. https://doi.org/10.1063/1.1653784.

[88] J.H. Park, J.K. Cho, K. Nishimura, H. Uchida, M. Inoue, Growth of epitaxial garnet film by LPE for application to integrated magneto-optic light switch arrays, Physica Status Solidi A Appl. Res. 201 (2004) 1976–1979. https://doi.org/10.1002/pssa.200304545 .

[89] J.W. Nielsen, S.L. Blank, D.H. Smith, G.P. Vella-Coleiro, F.B. Hagedorn, R.L. Barns, W.A. Biolsi, Three garnet compositions for bubble domain memories, J. Electron. Mater. 3 (1974) 693–707. https://doi.org/10.1007/bf02655293 .

[90] G.B. Stringfellow, Epitaxy, Rep. Prog. Phys. 45 (1982) 469–525. https://doi.org/10.1088/0034-4885/45/5/001 .

[91] Балбашов А.М. Магнитные материалы для микроэлектроники / А.М. Балбашов, А.Я. Червоненкис // М.:Энергия, 1979. -216 с.

[92] Y. Zorenko, V. Gorbenko, T. Voznyak, V. Vistovsky, S. Nedilko, M. Nikl, Luminescence of ions in single crystalline films, Radiat. Meas. 42 (2007) 882–886. https://doi.org/10.1016/j.radmeas.2007.02.030 .

[93] S. Witkiewicz-Lukaszek, V. Gorbenko, T. Zorenko, Y. Syrotych, J.A. Mares, M. Nikl, O. Sidletskiy, P. Bilski, A. Yoshikawa, Y. Zorenko, Composite detectors based on single-crystalline films and single crystals of garnet compounds, Materials (Basel). 15 (2022) 1249. https://doi.org/10.3390/ma15031249 .

[94] Scintillators with high Z_{eff} on the base of $Lu_3Al_5O_{12}$:Ce single crystalline films: growth, properties and applications / Yu. Zorenko, V. Gorbenko, I. Konstankevych, M. Batenchuk // in: Proc. SCINT 1999. – M.: Moscow State University. – 2000. - P.532–537.

[95] M.E. Fitzpatrick, A.T. Fry, P. Holdway, F.A. Kandil, J. Shackleton, L. Suominen, Determination of residual stresses by X-ray diffraction, (2005). https://oro.open.ac.uk/11283 (accessed October 5, 2023).

[96] G.F. Harrington, J. Santiso, Back-to-Basics tutorial: X-ray diffraction of thin films, J. Electroceram. 47 (2021) 141–163. https://doi.org/10.1007/s10832-021-00263-6 .

[97] M. Elbaum, Quantitative cryo-scanning transmission electron microscopy of biological materials, Adv. Mater. 30 (2018). https://doi.org/10.1002/adma.201706681 .

[98] E. Popova, M. Deb, L. Bocher, A. Gloter, O. Stéphan, B. Warot-Fonrose, B. Berini, Y. Dumont, N. Keller, Interplay between epitaxial strain and low dimensionality effects in a ferrimagnetic oxide, J. Appl. Phys. 121 (2017). https://doi.org/10.1063/1.4978508 .

[99] H. Yu, Scanning acoustic microscopy for material evaluation, Appl. Microsc. 50 (2020). https://doi.org/10.1186/s42649-020-00045-4 .

[100] J. Hoffmann, S. Sathish, E.B. Shell, S. Fassbender, N. Meyendorf, Acoustic imaging techniques for characterization of corrosion, corrosion protective coatings, and surface cracks, in: Nondestructive Materials Characterization, Springer Berlin Heidelberg, Berlin, Heidelberg, 2004: pp. 294–322.

[101] K. Dynowski, J. Litniewski, A. Nowicki, Three-dimentional imaging in ultrasonic microscopy, Arch. Acoust. 32 (2014) 71–75. https://acoustics.ippt.pan.pl/index.php/aa/article/view/1391 (accessed October 01, 2023).

[102] J.G. Solé, L.E. Bausá, D. Jaque, An introduction to the optical spectroscopy of inorganic solids, Wiley, 2005.

[103] V-760 UV-Visible spectrophotometer - JASCO, JASCO Inc. (2017). https://jascoinc.com/products/spectroscopy/uv-visible-nir-spectrophotometers/models/v-760-uv-vis-spectrophotometer (accessed October 5, 2023).

[104] C.S. Creaser, J.R. Sodeau, Luminescence Spectroscopy, in: Perspectives in Modern Chemical Spectroscopy, Springer Berlin Heidelberg, Berlin, Heidelberg, 1990: pp. 103–136.

[105] Spectrofluorometer, Edinburgh Instruments. (2015). https://www.edinst.com/us/products/fs5-spectrofluorometer (accessed October 5, 2023).

[106] J. Schanda, ed., Colorimetry: Understanding the CIE System, (2007). https://doi.org/10.1002/9780470175637.

[107] Colorimetry of light sources gigahertz-optik, Gigahertz-optik.com. (n.d.). https://www.gigahertz-optik.com/en-us/service-and-support/knowledge-base/basics-light-measurement/light-color/colorimetry (accessed October 5, 2023)

[108] D. Durmus, Correlated color temperature: Use and limitations, Light. Res. Technol. 54 (2022) 363–375. https://doi.org/10.1177/14771535211034330.

[109] Integrating spheres, Avantes. (2020). https://www.avantes.com/products/accessories/integrating-spheres (accessed October 5, 2023).
[110] T.S. Duffy, Single-crystal elastic properties of minerals and related materials with cubic symmetry, Am. Mineral. 103 (2018) 977–988. https://doi.org/10.2138/am-2018-6285.
[111] W.J. Alton, A.J. Barlow, Temperature dependence of the elastic constants of yttrium aluminum garnet, J. Appl. Phys. 38 (1967) 3023–3024. https://doi.org/10.1063/1.1710044.
[113] Fluid Mechanics, Elsevier, 1987.
[114] G. Saatsakis, D. Linardatos, G. Karpetas, N. Kalyvas, K. Ninos, A. Bakas, E. Lavdas, G. Fountos, I. Kandarakis, I. Valais, C. Michail, On the thermal response of LuAG:Ce single crystals, Procedia Struct. Integr. 33 (2021) 287–294. https://doi.org/10.1016/j.prostr.2021.10.035 .
[115] Genetic algorithm, Mathworks.com. (n.d.). https://www.mathworks.com/help/gads/genetic-algorithm.html (accessed October 5, 2023).
[116] M.J. Weber, CRC Handbook of Laser Science and Technology supplement 2: Optical Materials, 1st ed., CRC Press, Boca Raton, FL, 1994.
[117] P.D. Dragic, M.G. Pamato, V. Iordache, J.D. Bass, C.J. Kucera, M. Jones, T.W. Hawkins, J. Ballato, Athermal distributed Brillouin sensors utilizing all-glass optical fibers fabricated from rare earth garnets: LuAG, New J. Phys. 18 (2015) 015004. https://doi.org/10.1088/1367-2630/18/1/015004.
[118] A. Kastengren, Thermal behavior of single-crystal scintillators for high-speed X-ray imaging, J. Synchrotron Radiat. 26 (2019) 205–214. https://doi.org/10.1107/s1600577518015230 .
[119] M. Nikl, Scintillation detectors for x-rays, Meas. Sci. Technol. 17 (2006) R37–R54. https://doi.org/10.1088/0957-0233/17/4/r01 .
[120] X. Yin, H. Lin, D. Zhang, R. Hong, C. Tao, Z. Han, A facile way to obtain LuAG:Ce^{3+} transparent ceramic phosphor and a LuAG:Ce^{3+}/Al ceramic metal integration structure, Mater. Res. Express. 6 (2019) 116214. https://doi.org/10.1088/2053-1591/ab4dd1 .
[121] T. Yanagida, Y. Fujimoto, Y. Yokota, A. Yoshikawa, T. Ishikawa, H. Fujimura, H. Shimizu, H. Yagi, T. Yanagitani, Scintillation properties of LuAG(Ce) ceramic and single crystalline scintillator, in: IEEE Nuclear Science Symposuim & Medical Imaging Conference, IEEE, 2010: pp. 1612–1614.
[122] P.-A. Douissard, T. Martin, F. Riva, Y. Zorenko, T. Zorenko, K. Paprocki, A. Fedorov, P. Bilski, A. Twardak, Epitaxial growth of LuAG:Ce and LuAG:Ce,Pr films and their scintillation properties, IEEE Trans. Nucl. Sci. 63 (2016) 1726–1732. https://doi.org/10.1109/tns.2016.2565731 .
[123] T. Zorenko, V. Gorbenko, T. Vozniak, S. Heinrich, G. Huber, Y. Zorenko, Comparison of the luminescent properties of LuAG:Ce films grown by pulse laser deposition and liquid phase epitaxy methods using synchrotron radiation excitation, Opt. Mater. 105 (2020) 109751. https://doi.org/10.1016/j.optmat.2020.109751 .

[124] K.V. Ivanovskikh, J.M. Ogiegło, A. Zych, C.R. Ronda, A. Meijerink, Luminescence temperature quenching for $Ce^{3+}$and pr^{3+}*d-f*emission in YAG and LuAG, ECS J. Solid State Sci. Technol. 2 (2013) R3148–R3152. https://doi.org/10.1149/2.011302jss .

[125] V. Khanin, A. Meijerink, A.J. Houtepen, H.J.B. Jagt, D.K.G. de Boer, Photosaturation in luminescent LuAG:Ce garnet concentrator rods, Adv. Photonics Res. 2 (2021). https://doi.org/10.1002/adpr.202100055 .

[126] L. Wang, H. Yang, Y. Zhang, Y. Liang, J. Zhang, E. Mei, F. Xu, J. Long, P. Yu, W. Xiang, All-inorganic high efficiency LuAG:Ce^{3+} converter based on phosphor-in-glass for laser diode lighting, J. Alloys Compd. 892 (2022) 161882. https://doi.org/10.1016/j.jallcom.2021.161882 .

[127] Y. Cao, R. Xie, Q. Liu, X. Chen, Pursuing phosphor materials for laser-driven lighting, Appl. Phys. Lett. 121 (2022). https://doi.org/10.1063/5.0127364 .

[128] Y. Zorenko, V. Gorbenko, I. Konstankevych, A. Voloshinovskii, G. Stryganyuk, V. Mikhailin, V. Kolobanov, D. Spassky, Single-crystalline films of Ce-doped YAG and LuAG phosphors: advantages over bulk crystals analogues, Journal of Luminescence. 114 (2005) 85–94. https://www.sciencedirect.com/science/article/pii/S0022231304005265 .

[129] Y. Zorenko, A. Voloshinovskii, V. Savchyn, T. Voznyak, M. Nikl, K. Nejezchleb, V. Mikhailin, V. Kolobanov, D. Spassky, Exciton and antisite defect-related luminescence in $Lu_3Al_5O_{12}$ and $Y_3Al_5O_{12}$ garnets, Phys. Status Solidi B Basic Res. 244 (2007) 2180–2189. https://doi.org/10.1002/pssb.200642431 .

[130] Z. Wang, J. Zou, C. Zhang, M. Shi, B. Yang, Y. Li, H. Zhou, Y. Liu, M. Li, X. Qian, High color rendering index of warm WLED based on LuAG:Ce^{3+} PiG coated $CaAlSiN_3$:Eu^{2+} phosphor film for residential lighting applications, J. Mater. Sci.: Mater. Electron. 29 (2018) 8767–8773. https://doi.org/10.1007/s10854-018-8893-7 .

[131] M.J. Hÿtch, E. Snoeck, R. Kilaas, Quantitative measurement of displacement and strain fields from HREM micrographs, Ultramicroscopy. 74 (1998) 131–146. https://doi.org/10.1016/s0304-3991(98)00035-7 .

[132] A. Moridi, H. Ruan, L.C. Zhang, M. Liu, Residual stresses in thin film systems: Effects of lattice mismatch, thermal mismatch and interface dislocations, Int. J. Solids Struct. 50 (2013) 3562–3569. https://doi.org/10.1016/j.ijsolstr.2013.06.022 .

[133] E. Talik, J. Kusz, A. Guzik, M. Szubka, K. Balin, J. Kisielewski, W. Wierzchowski, A. Malinowska, A. Strojny-Nedza, A. Pajaczkowska, W. Drozdowski, Properties of $Lu_3Al_5O_{12}$, $Lu_3Al_5O_{12}$:Pr, $Lu_3Al_5O_{12}$:Pr,Mo, and $(Lu_{1-x}Y_x)_3Al_5O_{12}$:Pr scintillator crystals, Mater. Res. Express. 4 (2017) 056201. https://doi.org/10.1088/2053-1591/aa6be5 .

[134] Y. Zorenko, V. Gorbenko, T. Voznyak, T. Zorenko, Luminescence of Pb^{2+}ions in YAG:Pb single-crystalline films, Phys. Status Solidi B Basic Res. 245 (2008) 1618–1622. https://doi.org/10.1002/pssb.200844093 .

[135] Shannon Radii, Ic.ac.uk. (n.d.). http://abulafia.mt.ic.ac.uk/shannon/ptable.php (accessed October 5, 2023).

[136] Y. Yuan, D. Wang, B. Zhou, S. Feng, M. Sun, S. Zhang, W. Gao, Y. Bi, H. Qin, High luminous fluorescence generation using Ce:YAG transparent ceramic excited by blue laser diode, Opt. Mater. Express. 8 (2018) 2760. https://doi.org/10.1364/ome.8.002760 .

[137] Y. Chen, M. Gong, G. Wang, Q. Su, High efficient and low color-temperature white light-emitting diodes with $Tb_3Al_5O_{12}:Ce^{3+}$ phosphor, Appl. Phys. Lett. 91 (2007). https://doi.org/10.1063/1.2771538 .

[138] P. Bolek, J. Zeler, V. Gorbenko, T. Zorenko, P. Popielarski, K. Bartosiewicz, A. Osvet, M. Batentschuk, E. Zych, Y. Zorenko, Luminescent properties of nanopowder and single-crystalline films of TbAG:Ce garnet, Phys. Status Solidi B Basic Res. 257 (2020). https://doi.org/10.1002/pssb.201900495 .

[139] M. Batentschuk, A. Osvet, G. Schierning, A. Klier, J. Schneider, A. Winnacker, Simultaneous excitation of Ce^{3+} and Eu^{3+} ions in $Tb_3Al_5O_{12}$, Radiat. Meas. 38 (2004) 539–543. https://doi.org/10.1016/j.radmeas.2003.12.009 .

[140] R. Turos-Matysiak, W. Gryk, M. Grinberg, Y.S. Lin, R.S. Liu, Energy transfer in $Y_{3-x-y}Tb_x Gd_yAl_5O_{12}$ doped with Ce^{3+}, Radiat. Meas. 42 (2007) 755–758. https://doi.org/10.1016/ j.radmeas. 2007.02.003 .

[141] A.A. Setlur, J.J. Shiang, C.J. Vess, Transition from long-range to short-range energy transfer through donor migration in garnet hosts, J. Phys. Chem. C Nanomater. Interfaces. 115 (2011) 3475–3480. https://doi.org/10.1021/jp110520j .

[142] Y. Zorenko, T. Voznyak, V. Vistovsky, T. Zorenko, S. Nedilko, M. Batentschuk, A. Osvet, A. Winnacker, G. Zimmerer, V. Kolobanov, D. Spassky, Energy transfer to ions in single crystalline films, Radiat. Meas. 42 (2007) 648–651. https://doi.org/10.1016/j.radmeas.2007.01.059.

[143] S. Ganschow, D. Klimm, P. Reiche, R. Uecker, On the Crystallization of Terbium Aluminium, (2008). https://www.semanticscholar.org/paper/b6557976c293a309b09e2f72e94dcca8b45cbf07 (accessed October 5, 2023).

[144] V.I. Chani, A. Yoshikawa, H. Machida, T. Fukuda, Melt growth of $(Tb,Lu)_3Al_5O_{12}$ mixed garnet fiber crystals, J. Cryst. Growth. 212 (2000) 469–475. https://doi.org/10.1016/s0022-0248(00)00021-x .

[145] S. Witkiewicz-Lukaszek, V. Gorbenko, T. Zorenko, O. Sidletskiy, P. Arhipov, A. Fedorov, J.A. Mares, R. Kucerkova, M. Nikl, Y. Zorenko, Liquid phase epitaxy growth of high-performance composite scintillators based on single crystalline films and crystals of LuAG, CrystEngComm. 22 (2020) 3713–3724. https://doi.org/10.1039/d0ce00266f .

[146] Y. Zorenko, V. Gorbenko, T. Voznyak, M. Batentschuk, A. Osvet, A. Winnacker, Luminescence of Mn^{2+} ions in $Tb_3Al_5O_{12}$ garnet, J. Lumin. 130 (2010) 380–386. https://doi.org/10.1016/j.jlumin.2009.09.024 .

[147] One-dimensional dislocations. I. Static theory, Proc. R. Soc. Lond. 198 (1949) 205–216. https://doi.org/10.1098/rspa.1949.0095 .

[148] J.M. Ogiegło, A. Zych, K.V. Ivanovskikh, T. Jüstel, C.R. Ronda, A. Meijerink, Luminescence and energy transfer in $Lu_3Al_5O_{12}$ scintillators co-doped with Ce^{3+} and Tb^{3+}, J. Phys. Chem. A. 116 (2012) 8464–8474. https://doi.org/10.1021/jp301337f .

[149] K. Bartosiewicz, A. Markovskyi, T. Zorenko, A. Yoshikawa, S. Kurosawa, A. Yamaji, Y. Zorenko, New efficient scintillating and photoconversion materials based on the self-flux grown $Tb_3Al_5O_{12}$:Ce single crystal, Phys. Status Solidi Rapid Res. Lett. 14 (2020). https://doi.org/10.1002/pssr.202000327 .

[150] V. Bachmann, C. Ronda, A. Meijerink, Temperature quenching of yellow Ce^{3+} luminescence in YAG:Ce, Chem. Mater. 21 (2009) 2077–2084. https://doi.org/10.1021/cm8030768 .

[151] M. Nikl, Energy transfer phenomena in the luminescence of wide band-gap scintillators, Physica Status Solidi A Appl. Res. 202 (2005) 201–206. https://doi.org/10.1002/pssa.200460107 .

[152] Y. Yang, X. Wang, B. Liu, Y. Zhang, X. Lv, J. Li, S. Li, L. Wei, H. Zhang, C. Zhang, Dependence of emitting light for LEDs fabricated by YAG:Ce crystal wafer on wafer thickness, J. Lumin. 204 (2018) 157–161. https://doi.org/10.1016/j.jlumin.2018.08.024.

[153] P.A. Tanner, L. Fu, L. Ning, B.-M. Cheng, M.G. Brik, Soft synthesis and vacuum ultraviolet spectra of YAG:Ce^{3+}nanocrystals: reassignment of Ce^{3+}energy levels, J. Phys. Condens. Matter. 19 (2007) 216213. https://doi.org/10.1088/0953-8984/19/21/216213 .

[154] Y. Zorenko, V. Gorbenko, T. Zorenko, K. Paprocki, P. Bilski, A. Twardak, T. Voznyak, O. Sidletskiy, Y. Gerasimov, B. Gryniov, A. Fedorov, Composition engineering of single crystalline films based on the multicomponent garnet compounds, Opt. Mater. (Amst.). 61 (2016) 3–10. https://doi.org/10.1016/j.optmat.2016.03.031 .

[155] V. Gorbenko, T. Zorenko, S. Witkiewicz, K. Paprocki, O. Sidletskiy, A. Fedorov, P. Bilski, A. Twardak, Y. Zorenko, LPE growth of single crystalline film scintillators based on Ce^{3+} doped $Tb_{3-x}Gd_xAl_{5-y}Ga_yO_{12}$ mixed garnets, Crystals, 7 (2017) 262. https://doi.org/10.3390/cryst7090262 .

[156] D. Feezell, S. Nakamura, Invention, development, and status of the blue light-emitting diode, the enabler of solid-state lighting, Comptes Rendus Physique, 19 (2018) 113–133. https://doi.org/10.1016/j.crhy.2017.12.001 .

[157] T. Förster, Zwischenmolekulare energiewanderung und Fluoreszenz, Ann. Phys. 437 (1948) 55–75. https://doi.org/10.1002/andp.19484370105 .

[158] A.G. Petrosyan, K.L. Ovanesyan, R.V. Sargsyan, G.O. Shirinyan, D. Abler, E. Auffray, P. Lecoq, C. Dujardin, C. Pedrini, Bridgman growth and site occupation in LuAG:Ce scintillator crystals, J. Cryst. Growth. 312 (2010) 3136–3142. https://doi.org/10.1016/j.jcrysgro.2010.07.042 .

[159] R.R. Jacobs, W.F. Krupke, M.J. Weber, Measurement of excited-state-absorption loss for Ce^{3+} in $Y_3Al_5O_{12}$ and implications for tunable $5d \rightarrow 4f$ rare-earth lasers, Appl. Phys. Lett. 33 (1978) 410–412. https://doi.org/10.1063/1.90395 .

[160] Y. Zhuang, C. Li, C. Liu, Y. Fu, Q. Shi, Y. Liang, L. Xia, High-efficiency YAG:Ce^{3+} glass-ceramic phosphor by an organic-free screen-printing technique for high-power WLEDs, Opt. Mater. (Amst.). 107 (2020) 110118. https://doi.org/10.1016/j.optmat.2020.110118 .

[161] X. Liu, X. Wang, L. Ma, W. Shen, Z. Wang, $Tb^{3+} \rightarrow Ce^{3+}$ energy transfer in $Y_3Ga_5O_{12}$:Ce^{3+},Tb^{3+} garnet, J. Lumin. 40–41 (1988) 653–654. https://doi.org/10.1016/0022-2313(88)90374-2 .

[162] Y. Zorenko, V. Gorbenko, V. Savchyn, T. Zorenko, T. Martin, P.-A. Douissard, M. Nikl, J.A. Mares, Luminescent properties and energy transfer processes in Ce–Tb doped single crystalline film screens of Lu-based silicate, perovskite and garnet compounds, Radiat. Meas. 56 (2013) 415–419. https://doi.org/10.1016/j.radmeas.2013.01.042 .

[163] Y. Peng, Q. Sun, J. Liu, H. Cheng, Y. Mou, Fabrication of stacked color converter for high-power WLEDs with ultra-high color rendering, J. Alloys Compd. 850 (2021) 156811. https://doi.org/10.1016/j.jallcom.2020.156811 .

[164] S. Hu, C. Lu, G. Zhou, X. Liu, X. Qin, G. Liu, S. Wang, Z. Xu, Transparent YAG:Ce ceramics for WLEDs with high CRI: Ce^{3+} concentration and sample thickness effects, Ceram. Int. 42 (2016) 6935–6941. https://doi.org/10.1016/j.ceramint.2016.01.079 .

[165] S. Nishiura, S. Tanabe, K. Fujioka, Y. Fujimoto, Properties of transparent Ce:YAG ceramic phosphors for white LED, Opt. Mater. (Amst.). 33 (2011) 688–691. https://doi.org/10.1016/j.optmat.2010.06.005 .

[166] X. Shen, D.-F. Zhang, X.-W. Fan, G.-S. Hu, X.-B. Bian, L. Yang, Fabrication and characterization of YAG:Ce phosphor films for white LED applications, J. Mater. Sci.: Mater. Electron. 27 (2016) 976–981. https://doi.org/10.1007/s10854-015-3841-2 .